Electron Transport in Quantum Dots Defined in Low-Dimensional Semiconductor Structures

Larsson, Marcus

2011

Electron Transport in Quantum Dots Defined in Low-Dimensional Semiconductor Structures

Marcus Larsson

LUND
UNIVERSITY

Department of Physics
Lund, Sweden 2011

Akademisk avhandling för avläggande av teknologie doktorsexamen vid tekniska fakulteten vid Lunds universitet.
Lund, september 2011

Division of Solid State Physics
Department of Physics
Lund University
P.O. Box 118
SE-221 00 Lund
Sweden

ISBN 978-91-7473-172-9
Printed in Sweden by Media-Tryck, Lund
September 2011

Abstract

This thesis focuses on electron transport in single and double quantum dots defined in low-dimensional, narrow-band-gap III-V semiconductor materials. Fabrication schemes are presented for defining single and double quantum dots in lateral InGaAs/InP heterostructures, either by a combination of etching and local gating or solely by local top gating. The quantum dots are here electrostatically confined in at least one dimension. This allows for *insitu* control of the tunnel coupling of the quantum dots using gate voltages. Nanowire-defined quantum dots have also been studied. Here, the quantum dots are formed in an InSb nanowire segment through a metal electrode Schottky barrier.

Electron transport properties have been investigated in these systems at low temperatures and single-electron charging behavior consistent with both many- and few-electron single quantum dots was observed. Magneto-transport measurements of InGaAs defined many- and few-electron single quantum dots show level-dependent effective electron g-factors of $\sim 2-4$. For the InSb nanowire quantum dot, giant and level-depended g-factors of up to ~ 70 were observed. The level-to-level fluctuation in the g-factor is attributed to the presence of strong spin-orbit interaction in these systems. The magnitude of the spin-orbit interaction was investigated in an InSb nanowire quantum dot by finite bias magneto-spectroscopy. Spin-orbit mixing of a ground state and a first excited state with opposite spins induced an avoided level crossing in the quantum dot dominated by Zeeman energy. The avoided level crossing allowed a spin-orbit energy of ~ 280 μeV to be directly extracted. The spin filling sequence of a few-electron InGaAs single quantum dot was also investigated using ground state magneto-spectroscopy and parallel spin filling configurations were identified. From these configurations the lower bound of the exchange energy in the dot was estimated to be ~ 210 μeV.

Single quantum dots were also studied in the strong coupling regime where correlated electron transport processes become important. Here, co-tunneling, the spin-1/2 Kondo effect as well as an gate-induced splitting of

the Kondo effect of a few-electron InGaAs quantum dot were investigated and the characteristic energy scales of the system were extracted. In addition, the degeneracy point of two quantum levels of *equal* spin was studied in the strong coupling regime of an InSb nanowire quantum dot. Strong suppression of the co-tunneling background current was observed at the level degeneracy. This current suppression is attributed to the destructive interference of two spin-correlated conduction paths.

Pauli spin blockade at the $(3, 5) \rightarrow (2, 6)$ charge state transition in an InGaAs defined double quantum dot was identified, where (N_1, N_2) refers to the number of electrons in dot 1 and dot 2, respectively. An integrated quantum point contact charge state read-out sensor was used to determine the exact charge state of the double quantum dot. Leakage current was observed through the spin blockade, caused by triplet-to-singlet relaxation. The main contribution to the mixing of the singlet and triplet states is attributed to the hyperfine interaction between the electron spin and nuclear spin in the material. An effective nuclear magnetic field of ~ 2.7 mT was determined from the magnetic field dependence of the leakage current for detuned energy levels.

List of papers

I. Electron transport study of a lateral InGaAs quantum dot
Marcus Larsson, Daniel Wallin, and Hongqi Xu
Physica E **40**, 1950 (2008).
I fabricated the sample, and performed the measurements and data analysis. I wrote the paper.

II. A highly tunable lateral quantum dot realized in InGaAs/InP by an etching technique
Marcus Larsson, Daniel Wallin, and Hongqi Xu
Journal of Applied Physics **103**, 086101 (2008).
I fabricated the sample, and performed the measurements and data analysis. I wrote the paper.

III. Gate-defined quantum-dot devices realized in InGaAs/InP by incorporating a HfO_2 layer as a gate dielectric
Jie Sun, Marcus Larsson, Ivan Maximov, Hilde Hardtdegen, and Hongqi Xu
Applied Physics Letters **94**, 042114 (2009).
I participated in the measurements and data analysis.

IV. g-factor and exchange energy in a few-electron lateral InGaAs quantum dot
Marcus Larsson, Henrik A. Nilsson, Hilde Hardtdegen, and Hongqi Xu
Applied Physics Letters **95**, 192112 (2009).
I fabricated the sample, and performed the measurements and data analysis. I wrote the paper.

V. Giant, Level-Dependent g Factors in InSb Nanowire Quantum Dots
Henrik A. Nilsson, Philippe Caroff, Claes Thelander, Marcus Larsson, Jacob B. Wagner, Lars-Erik Wernersson, Lars Samuelson, and Hongqi Xu
Nano Letters **9**, 3151 (2009).
I participated in the measurements and data analysis.

VI. Correlation-Induced Conductance Suppression at Level Degeneracy in a Quantum Dot
Henrik A. Nilsson, Olov Karlström, Marcus Larsson, Philippe Caroff, Jesper N. Pedersen, Lars Samuelson, Andreas Wacker, Lars-Erik Wernersson, and Hongqi Xu
Physical Review Letters **104**, 186804 (2010).
I participated in the measurements and data analysis.

VII. Tunable zero-field Kondo splitting in a lateral InGaAs quantum dot
Marcus Larsson, and Hongqi Xu
Manuscript, to be submitted
I fabricated the sample, and performed the measurements and data analysis. I wrote the paper.

VIII. Gate-defined double quantum dot with integrated charge sensors realized in InGaAs/InP by incorporating a high κ dielectric
Jie Sun, Marcus Larsson, Ivan Maximov, and Hongqi Xu
Applied Physics Letters **96**, 162107 (2010).
I participated in the measurements and data analysis.

IX. Charge state readout and hyperfine interaction in a few-electron InGaAs double quantum dot
Marcus Larsson, and Hongqi Xu
Physical Review B **83**, 235302 (2011).
I fabricated the sample, and performed the measurements and data analysis. I wrote the paper.

Other papers that I have contributed to but that are not included because they deal with subjects beyond the scope of this thesis.

X. Thermally driven ballistic rectifer
Jason Matthews, David Sanches, Marcus Larsson, and Heiner Linke
arXiv:1107.3179v1, submitted to *Physical Review Letters*

XI. Supercurrent through InAs Nanowires with highly transparent superconducting contacts

Takahiro Nishio, Tatsuya Kozakai, Shinichi Amaha, Marcus Larsson, Henrik A. Nilsson, Hongqi Xu, Guoqiang Zhang, Kouta Tateno, Hideaki Takayanagi, and Koji Ishibashi

Accepted for publication in *Nanotechnology*

Preface and Acknowledgments

First of all I would like to thank my supervisor, Prof. Hongqi Xu, for giving me the opportunity to do my PhD in his research group. His enthusiasm and knowledge in the field of electron transport and physics in general have greatly inspired me. I am grateful for his support and encouragement over the past five years.

During my PhD I have had the fortune of attending several international conferences. I have also been involved in the EU research program SUBTLE. Thus, I have had the great pleasure of visiting many places all around the world and meeting scientists with different backgrounds. These trips have been fantastic experiences, both on a scientific and personal level.

I would like to express my deepest thanks to Dr. Daniel Wallin and Dr. Jie Sun for teaching me everything about nano-fabrication, measurement techniques and cryogenics. Their help and guidance when I started my PhD were invaluable. I would like to thank Dr. Stefano Roddaro for his help, especially for teaching me how the dilution refrigerator work.

I would like to thank all members of the Quantum Device Group, as well as my other collaborators, Nicklas Anttu, Erin Boyd, Dr. Patrik Brusheim, Dr. Philippe Caroff, Mingtang Deng, Jason Matthews, Dr. Henrik Nilsson, Dr. Takahiro Nishio, Jifa Tian, and Halvar Trodahl. Thanks to Dr. Hilde Hardtdegen for growing 2DEG samples for us. Thanks also to Dr. Andreas Fuhrer. Although he left the Division soon after I started my PhD, I profited greatly from his legacy. Anil Dey and Ricardo Andrade I would like to thank for their efforts during their Master's projects. Thanks to Anil Dey, Carl Ellström, Bahram Ganjipour, Sepideh Gorji, Sofia Johansson, Dr. Henrik Nilsson, Dr. Niklas Sköld and Dr. Daniel Wallin for creating a pleasant working environment in the office.

I am grateful to Prof. Lars Samuelson and Prof. Heiner Linke for creating an excellent research environment at the Division of Solid State Physics. I would also like to thank Ivan Maximov, Mariusz Graczyk, Lena Timby and all the other Nano Lab staff for keeping the cleanroom up and running. Special thanks to Leif Magnusson at Kryolab for providing me with liquid

helium whenever I asked. I would also like to thank Mona Hammar and Anders Gustafsson for their administrative support, and Bengt Bengtsson for computer support.

Last, but not least, I would like to thank my family and friends. Especially my parents Ingvar and Åsa for their unwavering support and encouragement.

Lund, September 2011

Marcus Larsson

Contents

Chapter 1

Introduction

Solids are typically classified into three categories depending on their electrical properties: conductors, insulators and semiconductors. Conductors such as metals conduct current well, whereas insulators do not conduct current. Semiconductors lie somewhere in between metals and insulators in terms of how well they conduct current. The current in solids is carried by the *electrons*, elementary particles that behave as both particles and waves. The differences in the electrical properties of solids arise from the interaction between the crystal structure of the material and the electrons. In solids, this interaction will give rise to an energy gap in the allowed states of the electrons in the material. In semiconductors and insulators, the energy gap divides electrons into *bound* electrons, the so-called valance band electrons, and *free* electrons, the so-called conduction band electrons. How well a semiconductor or insulator conducts current, i.e. its conductivity, is related to the number of electrons in the conduction band. In semiconductors the energy gap is small and in insulators the gap is large. This means that semiconductors can conduct fairly well at room temperature since bound electrons can become free mobile charge carriers through thermal excitation.

The conductivity of semiconductors can be fine-tuned, from metal-like to insulating, by introducing so-called *doping atoms* that control the number of free carriers in the conduction band, or by using an electric field to shape the band structure. The fact that the conductivity of semiconductors can be controlled is of the utmost importance to the semiconductor industry since this tunability is used to design electronic devices. It is thanks to this flexibility of semiconductor materials that the semiconductor industry has grown enormously over recent decades. The invention of the solid state semiconductor transistor in 1947, by J. Bardeen, W. Brattain, and W. Shockley at AT&T's Bell Labs was the starting point of this rapid growth. This discovery later earned the inventors the Nobel Prize in Physics [1]. The transistor can be

used as a fundamental building block to perform logic functions and is therefore integral to all electronic devices. Since the invention of the transistor, the semiconductor electronic devices functionality, size, power consumption, and integration have improved tremendously making everyday electronic devices, such as computers, mobile phones and digital cameras possible. These improvements have been made possible thanks to the on-going miniaturization and optimization of the transistor. For example, Intel's first processor, introduced in 1971, consisted of 2300 transistors with a minimum feature size of 10 μm. One of Intel's latest processors, the Intel Xeon introduced in 2007, has 820 million transistors with a minimum feature size of 45 nm [2]. Intel has since launched a series of processors based on 32 nm manufacturing technology [3].

Miniaturization of the transistor is becoming increasingly difficult partly due to quantum mechanical effects. These effects appear when the size of the transistor is of the same scale as the electron wavelength. Here, quantum mechanical effects such as tunneling, confinement and interference can dominate the electron transport properties of the transistor which will degrade the device performance. Current transistor designs will therefore become obsolete if the size continues to shrink. This challenge has led researchers to try to develop new devices based on novel physics that utilize quantum effects, instead of being hampered by them [4, 5, 6, 7, 8, 9]. By combining novel narrow-band-gap semiconductor compounds such as indium gallium arsenide (InGaAs) and indium antimonide (InSb) which exhibit large quantum confinement effects [10] with new nano-fabrication techniques, it is possible to investigate some of these new quantum effects.

As the size of the device becomes closer to the wavelength of the electrons in the material, confinement effects will lead to electrons exhibiting low-dimensional properties that differ from bulk properties. Low-dimensional properties of electrons are clearly seen in two-dimensional electron gases (2DEGs) based on semiconductor heterostructures [11, 12], and one-dimensional semiconductor nanowires [13, 14, 15]. In these nano-structures, electron motion is restricted in one or two dimensions, confining electrons to a plane (2DEGs) or along an axis (nanowires). The discovery of quantized states in a 2DEG system in a strong magnetic field in 1980 [16] resulted in the Nobel prize in physics in 1985 for the discoverer K. v. Klitzing [17]. 2DEGs are today commonly used for research purposes, as well as in high-electron-mobility transistors (HEMTs) for high-frequency applications, in for example, telecommunication. Their cylindrical geometry make nanowires excellent candidates as high-performance field effect transistors due to the excellent gate control of the conducting channel using wrap gates [18, 19].

By confining electrons to a nanometer-sized box in all directions it is pos-

sible to create so-called quantum dots, which exhibit zero-dimensional properties. These quantum dots show similar discrete energy spectra to atoms and are therefore sometimes referred to as *artificial atoms*. Additionally, quantum dots show strong Coulomb repulsion effects. When electrons are added to the dot the electrostatic energy of the dot jumps in steps due to the discrete nature of the electron charge. At low enough temperatures the discrete energies that electrons may populate are well defined. By connecting the quantum dot to contacted electron reservoirs and gate electrodes, the number of filled discrete levels may be tuned and the transport properties can be measured. Here, the quantum dot operates as an energy filter, only allowing electrons to pass through the system at specific energies. This controllable *single-electron transistor* behavior makes the quantum dot a potential candidate as a building block for devices based on novel physics [20].

One of the main benefits of the quantum dot system is the flexibility it allows in terms of device design, using nano-fabrication techniques, as well as the high degree of tunability of the system using external probes, such as gate voltages and magnetic fields. The flexibility and tunability of quantum dots have led to the proposal of their use as the elementary bits in a scalable quantum computer [6]. Here, the spin on the quantum dot forms a so-called quantum bit, or qubit, which can couple to other qubits. Quantum computers have been shown to solve certain types of computational problems much faster than classical computers [21]. One important requirement for functioning quantum computation based on spin qubits in quantum dots is a long spin coherence time, such that the spin states are coherently coupled during logic operations and state read-out. Thus, spin effects in quantum dots have been intensively studied in recent years [5]. Two main mechanisms couple the electron spin to the environment which can lead to spin decoherence in III-V semiconductor compounds, namely the spin-orbit interaction and the hyperfine interaction. The spin-orbit interaction couples the spin degree of freedom to the orbital momentum of the electron, which can lead to decoherence as the electron orbital couples to electric field fluctuations in the environment. The hyperfine interaction couples the electron spin to the randomly fluctuating nuclear spins of surrounding atoms and can lead to decoherence in materials with a non-zero nuclear spin. Despite these obstacles, researchers have made great progress in coherent manipulation of spins in quantum dots formed in GaAs-based 2DEGs [22, 23] and in InAs nanowires [24]. Although the spin-orbit interaction can lead to decoherence of electron spins in quantum dots, recent theoretical proposals [25, 26, 27] and experimental results [24] have shown that the strong spin-orbit interaction in narrow-band-gap semiconductors like InAs can be used for coherent manipulation of spins. It has also been proposed that nuclear spins could

potentially be used to store quantum information [28, 29].

To this end, it is important to improve our understanding of fundamental spin physics effects such as the Zeeman effect, the exchange interaction, the hyperfine interaction and the spin-orbit interaction in quantum dots. These effects are typically investigated by studying the evolution of ground state and excited state quantum dot levels in a magnetic field by standard transport spectroscopy at cryogenic temperatures.

Coherent transport in quantum dots can be studied in the regime of strong coupling between localized electrons residing on the dot and de-localized electrons in the contacts. When the quantum dot is in a magnetic configuration, i.e. it has a non-zero total spin, an increase in conductance related to the formation of a coherent state between localized and de-localized electrons can be observed. This effect is the so-called Kondo effect [30]. Other Kondo-like effects also appear for various other quantum dot configurations where spin and orbital degeneracies can result in correlated electron transport [31, 32, 33, 34].

This thesis is organized as follows:

Chapter 2 gives a brief description of the materials used. It also provides detailed information on device fabrication.

Chapter 3 begins with an introduction to transport in single quantum dots based on a simple theoretical model. Experimental low-temperature transport measurements of many-electron single quantum dots based on Papers I, II, and III and few-electron quantum dots are then presented. g-factors, exchange energy and spin-orbit energy of few-electron quantum dots obtained from magneto-transport data are reported. These measurements are based on Papers III, IV and V.

Chapter 4 focuses on correlated electron transport through single quantum dots in the strong coupling regime. The physical principles of elastic co-tunneling, inelastic co-tunneling and the Kondo effect are discussed and experimental data are presented. Measurements on gate-induced splitting of the Kondo effect and correlation-induced current suppression are also described. The measurements discussed in this chapter are based on Papers VI and VII.

Chapter 5 describes transport through double quantum dots. Here, a simple theoretical model for double quantum dot transport is presented together with transport data from a few-electron double quantum dot and a many-electron double quantum dot. A charge sensing scheme using a capacitively coupled quantum point contact is also presented. Further, spin blockade measurements used study triplet-to-singlet relaxation are described. The measurements presented in this chapter are based on Papers VIII and IX.

Chapter 2

Materials and device fabrication

The experimental work described in this thesis is based on devices fabricated from InGaAs/InP heterostructures (Papers I, II, III, IV, VII, VIII and IX), and in InAs/InSb heterostructure nanowires (Papers V and VI). This chapter describes the device fabrication, from material growth to the various processing techniques required to achieve the desired device.

In Section 2.1 the principles of epitaxial growth and the material properties of InGaAs/InP lateral heterostructures and InAs/InSb heterostructure nanowires are briefly discussed. Section 2.2 describes the fabrication of both lateral and nanowire-based quantum dot devices in detail.

2.1 Semiconductor growth

The materials used in this work were grown using metal organic vapor phase epitaxy (MOVPE), which is one of many different growth techniques used to produced highly ordered and almost perfect crystalline semiconductor materials. In MOVPE, the semiconductor species, usually from group III and column V in the periodic table, are introduced into a reactive chamber using a laminar flow of metal organic precursors at near atmospheric pressure. The sample substrate is placed inside the reactive chamber on a heated holder. When the metal organic precursors meet the heated sample substrate they will react and the desired semiconductor compound will be deposited on the substrate surface. By switching precursors it is possible to grow layered structures of different materials, so-called heterostructures. Optimization of the growth conditions can yield very sharp interfaces between different materials. Furthermore, dopants can be introduced into the chamber in order to locally control the doping level of the semiconductor.

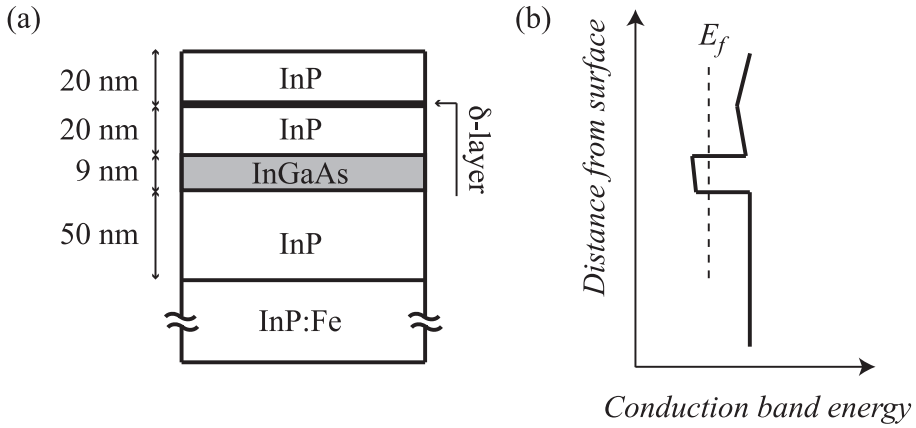

Figure 2.1: (a) Layer sequence for the InGaAs/InP heterostructure used in this work. (b) Sketch of the conduction band energy for an InGaAs/InP heterostructure.

2.1.1 Two-dimensional electron gas structures

The energy band structure of the resulting semiconductor heterostructure can be engineered by growing planar layers of different semiconductor materials on top of each other. Band engineering is a powerful tool in the manipulation of the electronic properties of semiconductors, and has led to development of faster electronic devices and the discovery of novel physics.

In the case of the InGaAs/InP heterostructure used in this work, the narrow band gap of a thin $In_{0.75}Ga_{0.25}As$ layer is sandwiched between layers of the larger-band-gap InP using MOVPE [35]. (The indices in $In_xGa_{1-x}As$ refer to the compound fraction.) In the following discussion InGaAs will be used to denote $In_{0.75}Ga_{0.25}As$ for simplicity. The small band gap in the thin InGaAs layer yields potential traps in the form of square quantum wells for electrons in the conduction band and for holes in the valance band in the growth direction. The quantum well restricts the motion of electrons in the growth direction, however in the plane of the interface there are no restrictions on the electron motion. Hence, this type of heterostructure is commonly referred to as a two-dimensional electron gas (2DEG). The electron concentration in the quantum well is controlled by introducing a very thin, highly Si-doped layer in the InP capping layer, a method called modulation doping or δ-doping. By spatially separating the 2DEG and the donor atoms it is possible to avoid increased scattering in the conducting layer from donor impurities in the lattice while still achieving a high electron concentration. Figure 2.1 shows the full layer sequence for the heterostructure grown on

top of a semi-insulating InP substrate (a) and a schematic of the conduction band energy (b).

Compared to the more commonly used AlGaAs/GaAs heterostructure, where the 2DEG is defined in the GaAs layer close to the AlGaAs interface, the InGaAs 2DEG has a low effective mass producing a large confinement effect on the electrons. Due to the large indium content in the InGaAs layer the effective g-factor is large, making it an interesting material for spin physics studies. Another interesting possibility is to utilize the spin-orbit interaction caused by structural inversion asymmetry in quantum wells with a tilting potential. In devices made using such quantum wells the strength of the spin-orbit interaction can be controlled by applying an electric field perpendicular to the 2DEG plane using a top gate electrode [36]. Controlling the spin-orbit interaction could potentially be used in so-called spintronic devices [4].

At a temperature of 300 mK the InGaAs 2DEG used in this work has a mobility of 1.0×10^5 cm^{2}V^{-1}s^{-1}, a sheet electron concentration of 7.5×10^{11} cm^{-2} and mean free path of 1.4 μm. The 2DEG structures were grown in collaboration with the Institute of Bio- and Nanosystems, Jülich in Germany.

2.1.2 Nanowires

Nanowires are grown epitaxially by depositing gold nano-particles on the surface of a semiconductor substrate and introducing the appropriate semiconductor precursors into the reactive chamber. Under correct conditions of temperature and pressure, one-dimensional semiconductor nanowires will form below the gold particles. Here, the gold particles act as catalysts for growth in a process called vapor liquid solid epitaxy, [37] in which, the semiconductor material in the chamber is incorporated into the gold particle and deposited on the substrate below. The diameter of the nanowire is determined by the size of the gold particle used to facilitate growth. It is possible to grow nanowire heterostructures by changing the precursors. Due to the small diameter of nanowires it is possible to grow heterostructures using materials with very different lattice constants since the strain produced at the interfaces of the different layers can relax to the sides.

The nanowires studied in this work were grown by MOVPE using aerosol gold particles with a diameter of 40 nm deposited on an InAs substrate. First, InAs nanowire segments were grown followed by a second stage of growth where the precursors were changed such that InSb segments were formed. Figure 2.2(a) shows a scanning electron microscope image of the as-grown InAs/InSb heterostructure nanowires. A transmission electron microscope image of the InSb segment of one nanowire is shown in Figure 2.2(b). All

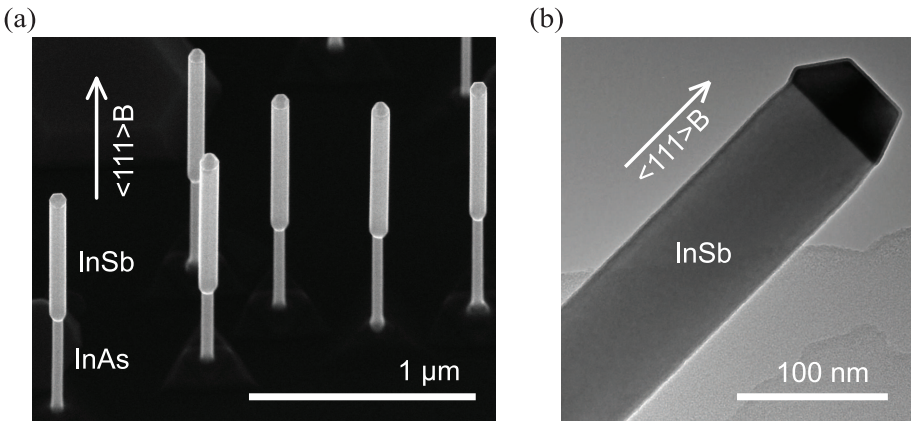

Figure 2.2: (a) Scanning electron microscope image of as-grown InAs/InSb heterostructure nanowires. (b) Transmission electron microscope image of an InSb segment of an InAs/InSb heterostructure nanowire.

nanowires were grown by Dr. Philippe Caroff at the Division of Solid State Physics, Lund.

2.2 Device fabrication

In order to achieve the desired device design, the semiconductor material grown needs to be further processed using a combination of lithography, etching, thermal evaporation and lift-off techniques. Lithography is a process for transferring a pattern onto a surface and comes from the Greek words *lithos*, which means 'stone', and *graphein*, which means 'writing', literally meaning 'stone writing'. In the context of this thesis lithography refers to the transfer of a pattern, nanometer-sized or larger, onto a sample surface. Lithography is performed on a clean sample surface which is first spin-coated with a resist, i.e. an organic polymer such as PMMA. The sample is then exposed to ultra-violet light (optical lithography or UVL) or an electron beam (electron beam lithography or EBL). The exposed parts of the polymer will have different chemical properties making them more or less solvable (depending on the type of resist used) in a developer. After developing the resist pattern, other processing steps, such as etching or metal evaporation and lift-off are typically performed. UVL is commonly used to expose large patterns since large areas can be irradiated simultaneous, whereas EBL is used to expose nanoscale structures since only small areas of the sample surface are irradiated at a time, but with high resolution.

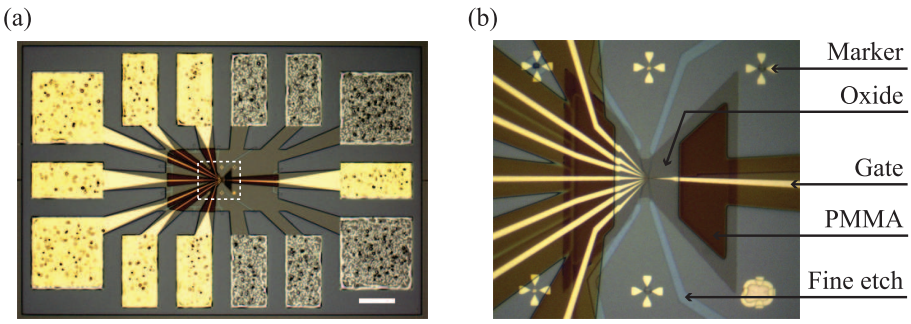

Figure 2.3: (a) Optical image of a lateral quantum dot device formed in an InGaAs/InP heterostructure. A combination of cross-linked PMMA and HfO_2 is used as a gate dielectric. The square and rectangular areas form contact pads for gate electrodes (yellow) and 2DEG regions (gray). The scale bar is 100 μm. (b) Enlargement of the dashed area in (a).

2.2.1 Fabrication of lateral quantum dot devices

Two sightly different fabrication schemes were used to fabricate lateral quantum dot devices: a combination of etching and metal electrode gating (papers I, II, IV, VII and IX) and metal electrode gating (papers III and XIII). The former fabrication scheme will be described here, as the latter scheme follows the same process steps except for the alignment marker and fine etch processes, which are not included. It should be noted that the latter scheme uses HfO_2 as a gate dielectric. The fabrication of lateral quantum dots is discussed mainly in Papers II, III and VIII. The top-gate-defined quantum dot devices (Papers III and VIII) were fabricated by Dr. Jie Sun at the Division of Solid State Physics, Lund.

The lateral quantum dot devices are fabricated in several steps. First the epitaxially grown InGaAs/InP wafer is cleaved into 3.5 mm x 4.5 mm large chips. Each chip is then carefully cleaned in remover 1165, acetone, and IPA to remove any particles on the surface. In the second step a mesa is defined on the sample surface in order to isolate gate contacts and ohmic contacts. Ohmic contacts to the 2DEG are formed by thermally annealing Au/Ge/Au metal layers deposited onto the surface. Next, a pattern of metal markers is fabricated on the surface of the chip in order to align the next patterns with each other. The nano-structure where the quantum dots will be defined is formed by wet chemical etching, followed by deposition of a layer of oxide and/or cross-linked PMMA resist used as gate dielectrics. In the final processing step, top gates made from Ti/Au are deposited over the device region. Optical images of such a device are shown in figure 2.3.

Mesa etching and ohmic contacts

The patterns formed in resist by lithography can be transferred to a semiconductor surface by etching. Various methods are available for etching semiconductor materials, however, in this work wet chemical etching was the only method used. The device mesa region is defined by either UVL or EBL followed by the etching of trenches. A clean sample is spin-coated with S1813 resist and baked on a hot plate at 115 °C for 90 s (UVL) or spin-coated with a double layer of ZEP 520A7 resist and baked on a hotplate at 160 °C for 15 min (EBL). The mesa pattern is then exposed in the resist using either UVL or EBL. The sample is then developed in MF319 for 2 min and rinsed in water for 60 s (UVL), or developed in oxylene for 5 min and rinsed in IPA for 20 s (EBL). The sample is baked in an oven at 120 °C for 30 min (UVL) or 120 °C for 5 min (EBL). Finally, the sample is etched in a room temperature solution of 40 ml water, 5 ml HBr, 5 ml HNO_3 and 300 μl saturated bromic water for 2 min. This yields an etch depth of several hundred nm, and the 2DEG below the exposed parts is thus removed. The resist is stripped by placing the sample in remover 1165 and heating to 80 °C for 10 min.

Ohmic contacts connecting the 2DEG electrically to metal contact pads on the sample surface are fabricated using either UVL or EBL. First, the sample is spin-coated with LOR 3A resist and baked on a hotplate at 170 °C for 20 min (UVL), or spin-coated with PMMA 950 A6 and baked at 160 °C for 10 min (EBL). For the UVL process a second S1813 resist layer is spin-coated on the sample and baked at 115 °C for 90s. The contact pad regions are then exposed using UVL or EBL. The sample is then developed in MF319 for 60 s and rinsed in water for 60 s (UVL) or in MIBK/IPA 1:3 for 90 s and rinsed in IPA for 30 s (EBL). The metal contact pad consists of Au/Ge/Au (400 Å/200 Å/1600 Å) layers. The whole sample surface is covered by metal using thermal evaporation followed by a lift-off procedure in which resist and metal is removed from the unexposed areas of the surface. Lift-off is achieved by placing the sample in warm (50 °C) acetone for 5 min and varm (50 °C) remover 1165 for 10 min (UVL) or in warm (50 °C) acetone for 20 min (EBL). Low-power ultrasonic treatment for 1 min is often needed to complete lift-off and remove all the unwanted metal traces. Lift-off is followed by rapid thermal annealing during which the sample is heated to 200 °C for 1 min and then to 390 °C for 2 min. During this rapid thermal annealing the metal melts and the Ge atoms diffuse down into the semiconductor, forming a highly n-doped region between the contact metal and the 2DEG. This procedure reduces the contact resistance. Typical resistances of these contacts are $\sim$10 kΩ at room temperature and $\sim$2 kΩ at 4.2 K.

Alignment markers

Metal markers are used to define a sample coordinate system for fine alignment of the different layers during EBL processing. The markers and alignment technique used in this work enabled a precision of better than 20 nm for different layers.

First, the sample is spin coated with PMMA 950 A5 resist and baked at 160 °C for 15 min. The marker patterns are then exposed using EBL. The sample is developed in MIBK/IPA 1:3 for 90 s and rinsed in IPA for 30 s. The markers are fabricated by thermal evaportation of Ti and Au layers with thicknesses of 50 Å and 450 Å, respectively. The Ti layer is used to improve the adhesion of the Au to the substrate. In the last step, the resist and unwanted metal is removed by lift-off in acetone for 1 to 2 hours followed by 1 min low-power ultrasonic treatment. All subsequent EBL patterns are aligned to these markers.

Fine etch

In order to create a quantum dot structure, electrons in the device have to be confined in all dimensions. This is achieved by a combination of etching trenches and gating, which together form the zero-dimensional quantum dot structure. Fine etch processing is similar to EBL mesa etching.

The sample is spin-coated with a single layer ZEP 520A7 resist and baked on a hotplate at 160 °C for 15 min. The fine etch patterns are then exposed using EBL. The sample is developed in oxylene for 5 min and rinsed in IPA for 10 s. The sample is then baked on a hotplate at 120 °C for 5 min, and etched in a room temperature solution of 60 ml water, 1 ml HBr, 1 ml HNO_3 and 125 μl saturated bromic water for 20 s. This yields an etch depth of $\sim$70 nm. Finally, the resist is stripped off by placing the sample in remover 1165 heated to 80 °C for 10 min.

Gate dielectric

Because of the small Schottky barrier of InP, an insulating layer is necessary between the metal gate electrodes and the InP capping layer in order to reduce leakage currents from gates to ohmic contacts and between gates. In the early quantum dot devices fabricated in this work cross-linked PMMA was used as the gate dielectric, whereas a thin film of HfO_2 locally deposited over the central device region was used in the later quantum dot devices in order to improve gating efficiency. Cross-linked PMMA was used for the other gate regions.

Hafnium oxide (HfO_2) is a dielectric material with a large dielectric constant, making it an excellent choice as a gate dielectric. HfO_2 is grown by atomic layer deposition at a temperature of 100 °C. The low temperature during growth makes it possible to do lift-off after deposition since the resist will not melt during growth.

First, PMMA 950 A5 resist is spin-coated on the sample and baked on a hotplate heated to 160 °C for 15 min. The oxide pattern is exposed using EBL. The sample is developed in MIBK/IPA 1:3 for 90 s and rinsed in IPA for 30 s. A thin film of HfO_2 with a thickness of ∼20 nm is then grown by atomic layer deposition, followed by lift-off. Lift-off is achieved by leaving the sample in acetone for 1 to 2 hours followed by 1 min low-power ultrasonic treatment.

Cross-linking PMMA is achieved by exposing the PMMA resist to high energy electrons such that the polymer chains of the resist form new chemical bonds [38]. The resulting polymer is difficult to remove with organic solvents, such as acetone, thus making it possible to perform further lithography and processing on top of the resist layer.

PMMA 950 A5 or A6 resist is spin-coated on the sample and baked on a hotplate at 160 °C for 15 min. The gate dielectric pattern is then exposed in the EBL using a very high dose, typically 1000 times higher than the normal dose. The unexposed areas of the resist are simply removed by placing the sample in acetone for 10 min. Finally, the sample with the remaining cross-linked resist is hard baked at 180 °C for 15 min.

Gate electrodes

Gate electrodes are used to fine-tune the electron concentration in the active regions of the device and to confine electrons to the quantum dots by modifying the potential landscape of the device.

PMMA 950 A4 resist is spin-coated on the sample and baked on a hot plate at 160 °C for 15 min. The gate pattern is then exposed using EBL. The sample is developed in MIBK/IPA 1:3 for 60 s and rinsed in IPA for 30 s. Layers of Ti and Au (50 Å and 450 Å) are deposited on the sample by thermal evaporation. Lift-off is carried out by leaving the sample in acetone for 2 hours followed by 1 min low-power ultrasonic treatment. In the thin finger gates used for later quantum dot devices a gate periodicity of 80 nm with a gate width of 40 nm was possible using this method.

2.2.2 Fabrication of nanowire quantum dot devices

In order to electrically characterize nanowires it is necessary to contact them with electrodes. In this work, this is done by breaking off the nanowires and placing them on a Si/SiO_2 substrate. Once on the substrate, traditional lateral lithographic techniques is used to electrically contact single InSb segments of InSb/InAs heterostructure nanowires.

The substrate is a degenerately doped Si wafer with a 100 nm thick surface layer of SiO_2. First, a metal gate electrode completely covering the back of the wafer is fabricated. The native oxide on the back side of the wafer is removed by spin-coating the front of the wafer with S1813 and baking the wafer at 120°C for 10 min, and then dipping the wafer in a small amount of hydrofluoric acid and rinsing it in water. Layers of Ti and Au (50 Å and 1000 Å) are then thermally evaporated onto the back of the wafer. The resist is then stripped in acetone. The front of the wafer, i.e. the side covered by SiO_2, is provided with alignment markers forming a coordinate system. The wafer is spin-coated with ZEP 520A7 and baked on a hotplate at 180 °C for 15 min. The coordinate markers are exposed by EBL. The wafer is developed in oxylene for 5 min and rinsed in IPA. The wafer is then briefly etched in O_2 plasma. Layers of Ti and Au (30 Å and 300 Å) are thermally evaporated onto the wafer, followed by lift-off in remover 1165. In the next step, the wafer is provided with large metal bonding pads. The wafer is spin-coated with LOR 7B resist, and baked in an oven at 180°C for 20 min. It is then spin-coated with S1813 resist and baked on a hotplate at 115°C for 90 s. The bonding pad pattern is exposed using UVL, developed in MF319 and rinsed in water. The wafer is then briefly etched in O_2 plasma. Layers of Ti and Au (50 Å and 1000 Å) are thermally evaporated onto the wafer followed by lift-off in remover 1165. The wafer is finally cleaved into 3.5 mm x 5.5 mm pieces.

Nanowires are transfered from the growth substrate to the processed Si/SiO_2 substrate using a cleanroom tissue. The method of transfer is completely stochastic, meaning that the wires will be randomly scattered over the sample surface. The wires are located by imaging with an optical microscope. The coordinate system makes it is possible to align metal electrodes with individual nanowires.

The sample is spin-coated with PMMA 950 A5 and baked in an oven at 180 °C for 1 hour. The electrode pattern is then exposed using EBL and developed in MIBK/IPA 1:3 for 1 min followed by rinsing in IPA for 30 s. The sample is etched briefly using O_2 plasma. To obtain good ohmic contacts with nanowires it is necessary to remove the native oxide on the wires and to passivate the surface. This is done by etching the sample in ammonium

sulfide, $(NH_4)_2S_x$ in water 1:9 for 2-3 min at a temperature of 40 °C. After passivation it is critical to quickly transfer the sample to the evaporator chamber to avoid re-oxidation of the semiconductor surface. Layers of Ti or Ni (200 or 250 Å) and Au (750 Å) are thermally evaporated onto the sample followed by lift-off in acetone. For further details on the fabrication of contacts to nanowires see [39]. All nanowire devices were fabricated by Dr. Henrik Nilsson at the Division of Solid State Physics, Lund.

Chapter 3

Single quantum dots

Studies on single quantum dots are presented in Papers I, II, III, VI, V, VI and VII. This chapter gives an introduction to electron transport in single quantum dot devices. Transport and magneto-transport properties in the weakly coupled regime where the lowest order tunneling events dominate, i.e. sequential tunneling, are discussed here. A theoretical description based on a capacitance model is used to interpret experimental data obtained from measurements on single quantum dots formed in an InGaAs/InP heterostructure and InSb nanowire quantum dots.

In Section 3.1 the so-called constant interaction theoretical model is presented. The physical concepts are based on references [40, 41, 42]. In Section 3.2 measurements on many-electron quantum dots are presented, while Section 3.3 presents measurements on a few-electron quantum dot where clear confinement effects were observed. Spin-related effects such as the Zeeman effect, exchange interaction and spin-orbit interaction are discussed in Sections 3.4, 3.5 and 3.6.

3.1 The constant interaction model

A quantum dot is a very small conducting island connected electrically to source and drain contacts via tunnel barriers. In such a system, interaction effects between electrons become important and when the size of the dot is comparable to the electron wavelength, confinement effects will greatly influence the energy spectrum of the dot. These effects lead to a discrete energy spectrum of the quantum dot resembling the energy spectrum of an atom. As a result, quantum dots are sometimes called *artificial atoms*. The so-called constant interaction model describes the quantum dot system in terms of capacitances and resistances. While there are many different types of quantum

dot systems, only lateral semiconductor heterostructure quantum dots and vertical semiconductor nanowire quantum dots, where the constant interaction model is adequate to describe the basic features of the experimental results, will be dealt with in this thesis. The constant interaction model assumes that the Coulomb interaction between electrons on the dot and the electrons in the surroundings is parameterized by a single constant capacitance, the self-capacitance C_Σ. The constant interaction model also assumes that the discrete energy levels that can be calculated from non-interacting electrons are not affected by electron-electron interactions, i.e. the number of electrons on the dot.

Figure 3.1 (a) shows a schematic equivalent electric circuit representing a quantum dot coupled to the source and drain leads with tunnel barriers and capacitively coupled to a gate. The charge on conductor i is given by

$$Q_i = \sum_{j=0}^{m} C_{ij} V_j, \tag{3.1}$$

where C_{ij} is the mutual capacitance of conductors i and j, V_j is the electrostatic potential on conductor j and m is the number of conductors. If the quantum dot is defined as conductor 0, then its electrostatic potential can be written as:

$$V_0 = \frac{1}{C_\Sigma}\left[Q_0 - \sum_{j=1}^{m} C_{0j} V_j\right], \tag{3.2}$$

where $C_{00} = C_\Sigma$ is the self-capacitance of the dot. C_{00} can be rewritten as the sum of all surrounding capacitances $C_{00} = -\sum_{j\neq 0} C_{0j}$.

The electrostatic energy, U, of a quantum dot containing N electrons is given by

$$U(N) = \int_0^{-Ne} V_0(Q_0) dQ_0 = \frac{N^2 e^2}{2C_\Sigma} + eN \sum_{j=1}^{m} \frac{C_{oj}}{C_\Sigma} V_j. \tag{3.3}$$

Based on the second assumption in the constant interaction model we simply add the single particle energies ϵ_i to the electrostatic energy to obtain the total quantum dot energy

$$E(N) = \sum_{i=1}^{N} \epsilon_i + U(N) = \sum_{i=1}^{N} \epsilon_i + \frac{N^2 e^2}{2C_\Sigma} + eN \sum_{j=1}^{m} \frac{C_{oj}}{C_\Sigma} V_j. \tag{3.4}$$

We can now write the electrochemical potential for the Nth electron, i.e. the energy required to add electron N to the dot, μ_N, as:

$$\mu_N = E(N) - E(N-1) = \epsilon_N + \frac{e^2}{C_\Sigma}\left(N - \frac{1}{2}\right) - e\sum_{j=1}^{m} \alpha_j V_j, \tag{3.5}$$

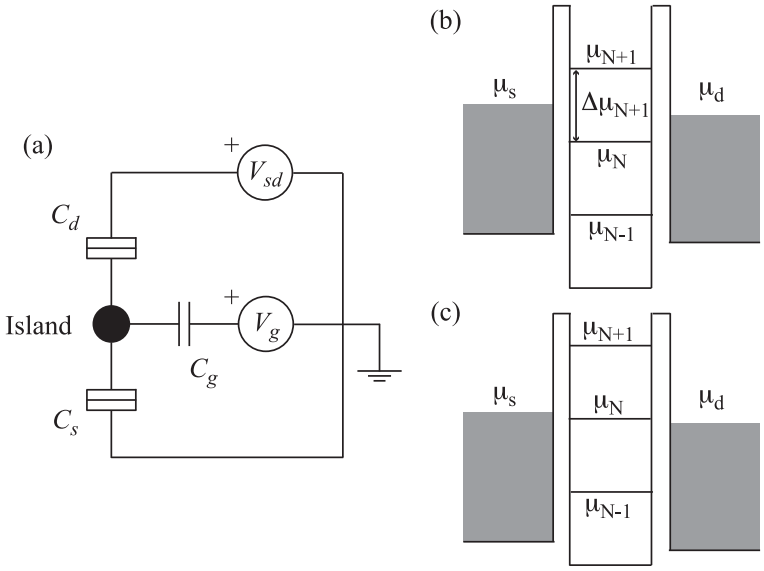

Figure 3.1: (a) Schematic of the electric circuit equivalent to a single quantum dot in the constant interaction model. Tunnel barriers connect the quantum dot to source and drain contacts. The gate is capacitively coupled to the quantum dot. (b) Schematic energy diagram of a quantum dot connected to source and drain electrochemical potentials. When the electrochemical potentials of the source and drain lie between two quantum dot levels the number of electrons on the dot is constant and electron transport is blocked. (c) The energy levels on the dot can be changed relative to the electrochemical potentials of the source and drain by changing the applied gate voltage, V_g. When an energy level is within the bias window electrons can flow from source to drain.

where the quantity $\alpha_j = -C_{0j}/C_\Sigma$ is the so-called lever arm of conductor j. α_j is always positive and is used in experiments to relate the gate voltage to the potential on the quantum dot. We can now determine the addition energy for adding electron N to the dot

$$\Delta\mu_N = \mu_N - \mu_{N-1} = \epsilon_N - \epsilon_{N-1} + \frac{e^2}{C_\Sigma} = \Delta\epsilon_N + \frac{e^2}{C_\Sigma}. \tag{3.6}$$

The first term, $\Delta\epsilon_N$, in Equation 3.6 is the single-particle energy difference between the states occupied by electrons N and $N-1$. The second term, e^2/C_Σ, is the so-called charging energy. The charging energy gives an indication of the size of the quantum dot since the capacitance of a conductor is related to its size.

3.1.1 Coulomb oscillations

Figure 3.1(a) shows a typical quantum dot circuit where only three conductors are connected to the quantum dot: the tunnel-coupled source and drain electrodes and the capacitively coupled gate electrode. Transport of electrons through such a system is depicted in an energy level diagram in Figure 3.1(b) where source and drain electrochemical potentials, μ_s and μ_d, are connected to the quantum dot filled with N electrons via two tunnel barriers. The positions of the energy levels, μ_N, in the quantum dot are given by Equation 3.5 and the addition energy by Equation 3.6. In the following discussion the applied source drain bias V_{sd} is assumed to be small compared to the temperature, i.e. $V_{sd} < k_BT$. It is also assumed that the temperature is low compared to the single-particle spacing, $k_BT << \Delta\mu_N$. Furthermore, the tunnel barriers must be high enough to ensure that the electrons are sufficiently localized to the dot. The resistance of the tunnel barriers should therefore be higher than the quantum resistance, $h/e^2 = 26$ kΩ. Under these assumptions electron transport in the configuration shown in Figure 3.1(b) is blocked since the electrons occupying the dot prohibits other electrons from tunneling into the dot. This configuration is usually called Coulomb blockade.

The electrochemical potential on the quantum dot can be changed by changing the voltage applied to the gate electrode, V_g. In Figure 3.1(c) a negative voltage has been applied to the gate, thus raising the electrochemical potential on the dot to a configuration where μ_N is aligned with μ_s and μ_d. Electrons can now tunnel from the source contact to the allowed state on the dot and finally leave the dot through the drain contact. In this way, the number of electrons on the dot will fluctuate between N and $N-1$. Transport

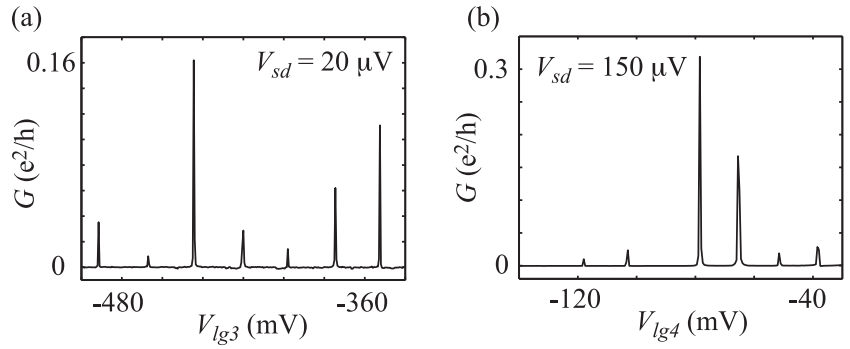

Figure 3.2: (a) Coulomb blockade oscillations in the current through a lateral InGaAs quantum dot as a function of gate voltage. The current oscillations are regularly spaced indicating that the single-particle level spacing is small compared to the charging energy. (b) Coulomb blockade oscillations in the few-electron limit for a lateral InGaAs quantum dot. The current oscillations appear in alternating large and small spacings indicating that the single-particle level spacing is comparable in size to the charging energy, and that there is two-fold degeneracy in the energy levels.

through the dot in this configuration is usually called resonant tunneling or sequential tunneling.

The positions of the current peaks can be determined by solving Equation 3.5 for the gate voltage

$$V_g^{(N)} = \frac{1}{e\alpha_g}\left[\epsilon_N + \frac{e^2}{C_\Sigma}\left(N - \frac{1}{2}\right) - e\sum_{j=4}^{m}\alpha_j V_j - \mu_s\right] \tag{3.7}$$

where $j = 1$ corresponds to the source, $j = 2$ to the drain and $j = 3$ to the gate, and α_g is the gate lever arm. The spacings of the peaks are then given by

$$\Delta V_g^{(N)} = \frac{1}{e\alpha_g}(\mu_N - \mu_{N-1}) = \frac{1}{e\alpha_g}(\epsilon_N - \epsilon_{N-1} + \frac{e^2}{C_\Sigma}). \tag{3.8}$$

From this equation it can be seen that it is possible to determine the single-particle level spacing from a measurement of Coulomb blockade peak spacings if the gate lever arm and charging energy is known.

Figure 3.2(a) shows a typical quantum dot transport measurement where the conductance through the quantum dot is plotted as a function of the applied gate voltage for a small source drain bias $V_{sd} = 20$ μV, measured at a temperature of 100 mK. The conductance peaks indicate the positions of

the energy levels in gate voltage in the dot according to Equation 3.7. Note that the spacing of the peaks is regular. This regular spacing is typical of metal dots and large semiconductor dots filled with many electrons, where the single-particle level spacing is much smaller than the charging energy. The periodicity of the peaks is therefore given by the charging energy and gate lever arm

$$\Delta V_g = \frac{1}{e\alpha_g}\frac{e^2}{C_\Sigma}. \tag{3.9}$$

Figure 3.2(b) shows a similar Coulomb oscillation measurement but for a smaller quantum dot which contains only a few electrons. The peaks now appear in pairs. The pairing of peaks is related to the single-particle level spacing (see Equation 3.8), which in this few-electron dot is comparable in size to the charging energy due to strong confinement effects. In addition to large single-particle level spacing two-fold spin degeneracy causes two electrons, one spin-up and one spin-down, to occupy each single-particle level. This gives current oscillations with alternating small and large spacings, where:

$$\Delta V_g^{odd} = \frac{1}{e\alpha_g}\frac{e^2}{C_\Sigma} \tag{3.10}$$

is the spacing for an odd number occupation on the dot and

$$\Delta V_g^{even} = \frac{1}{e\alpha_g}(\Delta\epsilon_N + \frac{e^2}{C_\Sigma}) \tag{3.11}$$

is the spacing for an even number occupation on the dot.

So far the quantum dot has been considered to be a non-interacting system. However, in order to understand the line shape of the Coulomb blockade peaks it is necessary to take into account the tunnel coupling strengths of the quantum dot to the source and drain contacts. The transmission rates Γ_s^N and Γ_d^N of peak N to the source and drain are given by the wave function overlap of the state on the dot and states on the source and drain contacts. Here we distinguish between two different regimes, the weak coupling regime when $\hbar\Gamma << k_BT$ and the strong coupling regime when $\hbar\Gamma \geq k_BT$, where $\Gamma = \Gamma_s + \Gamma_d$ and the index N has been dropped. The discussion here is based on the theory developed in reference [43].

In the weak coupling regime the thermal energy exceeds the width of the transmission resonance, meaning that the Coulomb peaks are thermally broadened. The discussion here is limited to the case when the single-particle level spacing is larger than the thermal energy, $\hbar\Gamma << k_BT << \Delta E_n$ where

n is a spin-degenerate level. Only one level on the dot contributes to electron transport and the conductance becomes:

$$G^i = \frac{e^2}{4k_BT}\left(\frac{1}{\Gamma_s^i}+\frac{1}{\Gamma_d^i}\right)^{-1}\cosh^{-2}\left(\frac{e\alpha_g(V_g-V_g^i)}{2k_BT}\right) \tag{3.12}$$

where i is a number associated with a Coulomb blockade peak centered around V_g^i. Note that the peak amplitude is inversely proportional to the temperature. By fitting this equation to experimental data it is possible to determine the transmission rate and electron temperature associated with each Coulomb blockade peak. Peak fitting of the Coulomb blockade peaks in Figure 3.2(a) using Equation 3.12 gives electron temperatures in the range of 100 ± 10 mK and transmission rates on the order of GHz.

In the strong coupling regime, transport through the quantum dot is considered for noninteracting electrons including inelastic scattering. The conductance then takes the Breit-Wigner form [44]:

$$G^i = \frac{2e^2}{h}\frac{\Gamma_s^i\Gamma_d^i}{\Gamma^i}\frac{h^2\Gamma^i}{[e\alpha_g(V_g^i-V_g)]^2+(h\Gamma^i/2)^2} \tag{3.13}$$

where $\Gamma^i = \Gamma_s^i + \Gamma_d^i$.

In a real sample, the transmission rates typically vary considerably between Coulomb blockade peaks, see Figure 3.2(a) and (b), since individual states in the leads tend to couple to the dot state with different strengths. For lateral quantum dots the leads are semiconducting and are, as such, affected by the gate voltage. Therefore, the number of lead states that couple to the dot state and the transmission rates are expected to change with gate voltage.

3.1.2 Charge stability diagram

So far we have only considered transport through quantum dots for small source-drain bias voltages, the so-called linear response regime. In order to fully characterize a quantum dot, measurements at finite bias are necessary. In the following discussion it is assume that the bias is applied symmetrically between the source and drain contacts, since this resembles the experimental measurement setup. Figure 3.3(a) shows the current through a quantum dot as a function of applied bias for a fixed gate voltage. For small biases transport is Coulomb blockaded as depicted in Figure 3.3(b). However, when the bias approaches the addition energy, assuming that the electrochemical potentials μ_s and μ_d at zero bias lie right between μ_N and μ_{N+1}, the Coulomb blockade is lifted and electrons can flow from source to drain, see

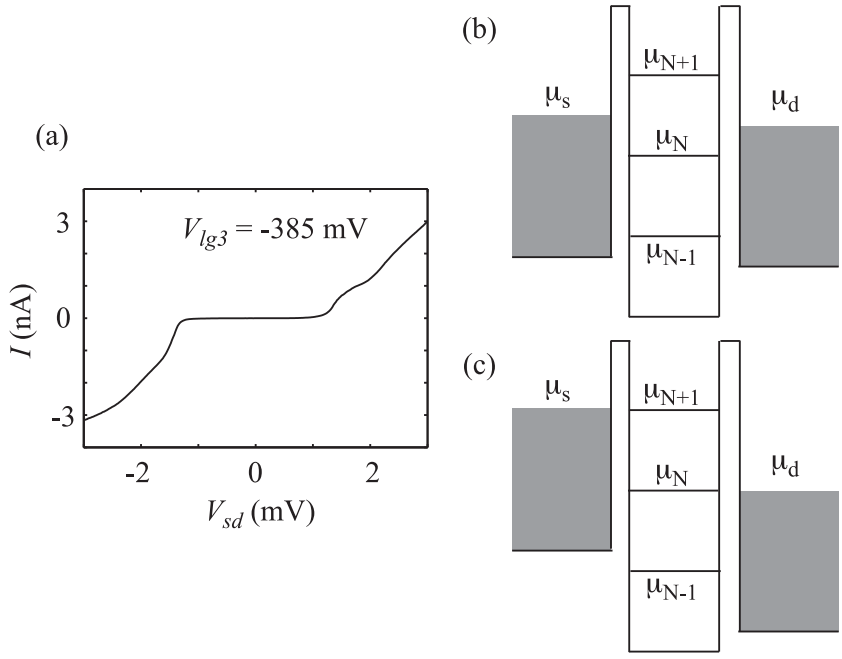

Figure 3.3: (a) Current (I) as a function of source-drain voltage (V_{sd}) for a quantum dot. For small voltages transport is Coulomb blockaded. For large voltages the Coulomb blockade is lifted and transport is possible. (b) Schematic energy diagram of a Coulomb blockaded quantum dot for small biases. (c) Transport through the quantum dot is possible when at least one level on the dot is within the source-drain electrochemical potential window.

Figure 3.3(c). The lifting of the Coulomb blockade is seen in Figure 3.3(a) as a decrease in resistance for $|V_{sd}| > 1.6$ mV. Measurements like the one in Figure 3.3(a) are made for many different gate voltages to form a so-called charge stability diagram.

To model the transport behavior for large biases, the chemical potential for source and drain contacts are written as $\mu_s = \mu_0 + eV_{sd}/2$ and $\mu_d = \mu_0 - eV_{sd}/2$ where μ_0 the chemical potential for source and drain contacts with no applied bias. The number of electrons on the dot (N) is then stable if:

$$\mu_N < \mu_0 - eV_{sd}/2 \tag{3.14}$$
$$\mu_{N+1} > \mu_0 + eV_{sd}/2 \tag{3.15}$$

for $V_{sd} > 0$, and

$$\mu_N < \mu_0 + eV_{sd}/2 \tag{3.16}$$
$$\mu_{N+1} > \mu_0 - eV_{sd}/2 \tag{3.17}$$

for $V_{sd} < 0$. These inequalities combined with Equation 3.7 give two equations that describe the positions where Coulomb blockade for a system is lifted in terms of gate and bias voltage. For $V_{sd} > 0$ and $\mu_{N+1} = \mu_0 + eV_{sd}$ we obtain:

$$V_g = \frac{1}{e\alpha_g}\left[\epsilon_{N+1} + \frac{e^2}{C_\Sigma}\left(N + \frac{1}{2}\right) - \mu_0 - (1 + \alpha_s - \alpha_d)\frac{eV_{sd}}{2} - e\sum_{j=4}^{m}\alpha_j V_j\right] \tag{3.18}$$

which describes the alignment of μ_{N+1} and μ_s. For $V_{sd} > 0$ and $\mu_N = \mu_0 + eV_{sd}$ we obtain

$$V_g = \frac{1}{e\alpha_g}\left[\epsilon_N + \frac{e^2}{C_\Sigma}\left(N - \frac{1}{2}\right) - \mu_0 + (1 - \alpha_s + \alpha_d)\frac{eV_{sd}}{2} - e\sum_{j=4}^{m}\alpha_j V_j\right] \tag{3.19}$$

which describes the alignment of μ_N and μ_d. α_s and α_d are the lever arms of the source and drain contacts. If the couplings to the source and drain are equal, i.e. $\alpha_s = \alpha_d$, then the charge transition borderlines describing the alignments will have the same slope but opposite signs, $\pm 1/2\alpha_g$. The two borderlines with slopes of opposite signs corresponding to the same charge state will cross at $eV_{sd} = \Delta\epsilon_N + e^2/C_\Sigma$.

Figure 3.4 shows the borderline regions based on Equations 3.18 and 3.19 in a schematic charge stability diagram, also know as a Coulomb blockade

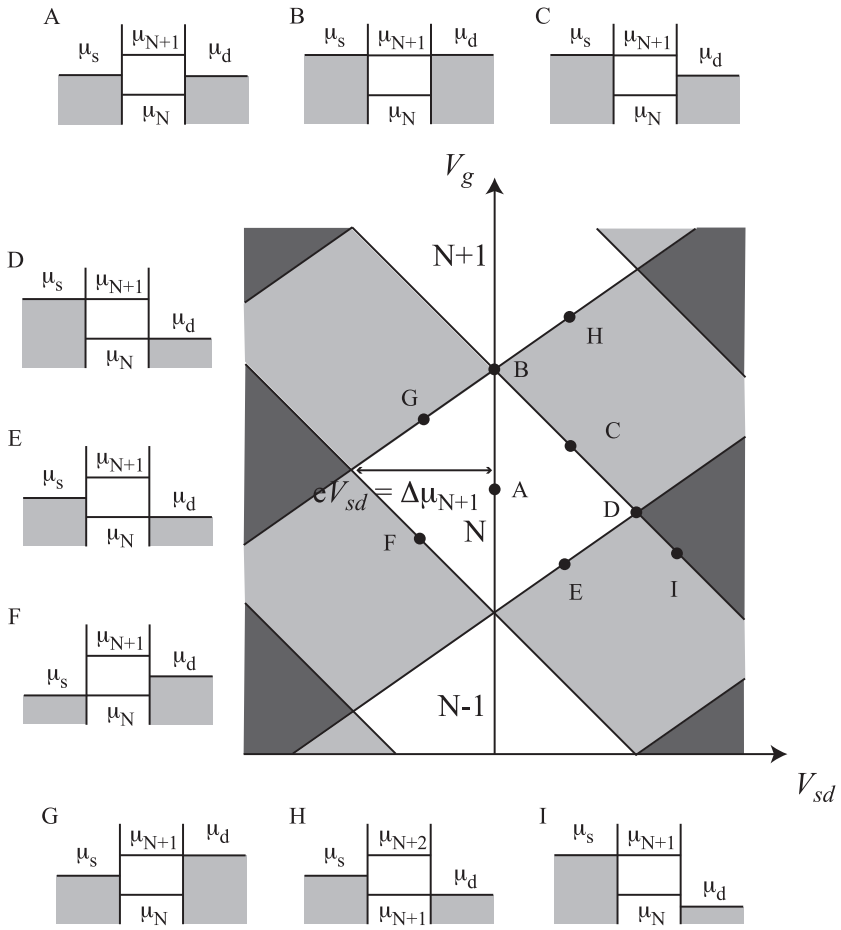

Figure 3.4: Schematic charge stability diagram showing the charge transition borders of a quantum dot as a function of gate voltage, V_g, and source-drain voltage, V_{sd}. Point A corresponds to a Coulomb blockade configuration where the number of electrons on the dot is N. Point B corresponds to a low bias situation where the electrochemical potential of the source and drain contacts are aligned with μ_{N+1} and the number of electrons on can fluctuate between N and $N + 1$. Point D corresponds to the case where μ_s is aligned with μ_{N+1} and μ_d is aligned with μ_N. Points C, G, H, and I correspond to cases where μ_s or μ_d is aligned with μ_{N+1}. Points E and F correspond to configurations where μ_s or μ_d is aligned with μ_N.

diamond diagram. The white regions correspond to a Coulomb blockaded configuration where the number of electrons on the dot is fixed. At the black borders the Coulomb blockade is lifted and transport is possible. The light gray areas correspond to sequential transport through one level on the dot. By applying a large source-drain bias it is possible to open simultaneous transport through two levels on the dot. This situation is indicated by the dark gray areas. Experimentally, it is possible to construct a charge stability diagram by plotting the differential conductance, dI_{sd}/dV_{sd}, as a function of V_g and V_{sd}. The black borderlines in Figure 3.4 would correspond to high differential conductance in the measured charge stability diagram. The addition energy can be directly read from the width of the diamond from the source-drain voltage, see point D in Figure 3.4, and from the slopes of the lines it it possible to determine the gate lever arm α_g. Once α_g is known it is possible to convert the gate voltage to an energy scale.

3.2 Transport in many-electron quantum dots

Since the discovery of single-electron tunneling in GaAs/AlGaAs nanostructures, [45] semiconductor quantum dots have been used to study many-electron dynamics. This section focus on the many-electron quantum dot described in Paper II, which was fabricated following the lateral device processing procedure described in Section 2.2.1, using only a layer of cross-linked PMMA as the gate dielectric. (A similar device was also studied in Paper I.) A circular quantum dot with a diameter of 350 nm was defined in the InGaAs 2DEG by etching trenches. The quantum dot is connected to the source and drain 2DEG contacts and surrounded by six in-plane gates. A top gate metal electrode was locally deposited on top of the quantum dot and is separated from the semiconductor substrate by a 250 nm thick layer of cross-linked PMMA. The device was cooled to cryogenic temperatures in a ^{3}He-based cryostat with a base temperature of 300 mK.

Figure 3.5(a) shows a scanning electron microscope image of a device similar to the one studied, after etching. The top gate is outlined by dashed yellow lines. In order to form tunneling barriers, static negative voltages were applied to the in-plane gates as well as the top gate, $V_l = V_r = -0.8$ V and $V_{tg} = -1.2$ V. This depletes the narrow constrictions connecting the quantum dot to the source and drain electron reservoirs and traps a pool of electrons in the dot.

Figure 3.5(b) shows Coulomb blockade oscillations in the conductance through the quantum dot in the linear response regime as a function of the voltage applied to the upper and lower middle gates, V_m. Note the regular

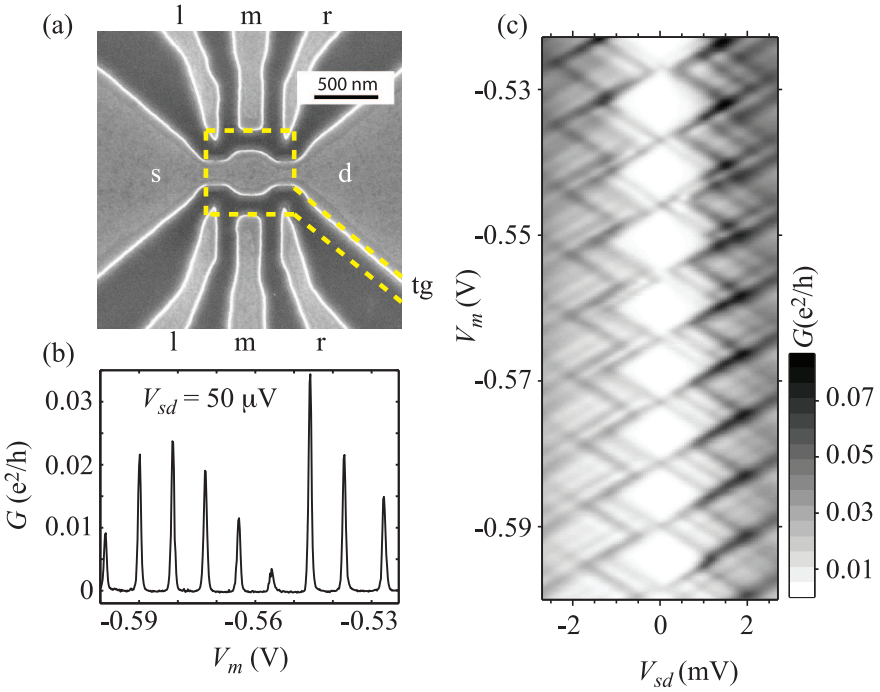

Figure 3.5: (a) Scanning electron microscope image of a lateral quantum dot device defined in an InGaAs/InP heterostructure. The dark regions are etched trenches. A quantum dot with a diameter of 350 nm is connected to source and drain contacts. Six in-plane gates surround the quantum dot. A 250 nm thick dielectric layer of cross-linked PMMA (not seen here) is used to isolate a top gate electrode (dashed yellow line). (b) Coulomb blockade oscillations in the conductance (G) as a function gate voltage (V_m) measured at a temperature of 300 mK. (c) Charge stability diagram showing differential conductance (G) as a function of source-drain voltage V_{sd} and gate voltage V_m.

peak spacing, similar to Figure 3.2(a), where the spacing is primarily determined by the charging energy. Thus, $\Delta V_m = e/\alpha_m C_\Sigma = e/C_m$, where α_m and C_m are the lever arm and gate capacitance of the combined upper and lower middle gates, respectively. From the peak spacings in Figure 3.5(b), the gate capacitance was determined to be $C_m = 18$ aF. From similar measurements of the other gates in the device (not shown here) the other gate capacitances were found to be $C_l = 12$ aF, $C_r = 10$ aF and $C_{tg} = 28$ aF. As described in Section 3.1.2, in order to determine the charging energy and gate lever arms it is necessary to study the charge stability diagram of the quantum dot in the appropriate source-drain voltage range. Figure 3.5(c) shows the charge stability diagram for the same gate range as in (a). The regularity in Coulomb Oscillation peak spacing is seen here as regular sized Coulomb blockade diamonds. A charging energy of 1.2 meV was determined from the width of the diamond, corresponding to a self-capacitance of $C_\Sigma = 130$ aF. The gate lever arms were also determined, $\alpha_m = 0.13$, $\alpha_l = 0.09$, $\alpha_r = 0.07$ and $\alpha_{tg} = 0.21$.

From the self-capacitance it is possible to estimate the electric size of the quantum dot. If we assume that the quantum dot is circular, then the capacitance can be written as $C_\Sigma = 4\epsilon_r\epsilon_0 d$, where ϵ_r is the dielectric constant of InGaAs and d is the electric diameter of the quantum dot. This expression gives an electric size of 260 nm for the quantum dot. The difference between the physical size (350 nm) and electric size (260 nm) of the quantum dot can be explained by the application of the negative voltages to the gates and surface depletion. Surface depletion arises when surface states pin the Fermi level and bend the bands locally so that electrons in the semiconductor are pushed away from the surface. The negative voltages applied to the gates bend the bands further resulting in a smaller electric size than physical size of the quantum dot.

A many-electron quantum dot defined only by top gate electrodes was also fabricated and analyzed in a similar fashion to that described above, see Paper III. A 24 nm thin film of HfO_2 was used as the gate dielectric in this device. The lithographic size of the dot was 250 nm with a square shape defined by four top gate electrodes (see inset in Figure 3.6). Figure 3.6 shows Coulomb oscillations in the current through the quantum dot as a function of the plunger gate voltage V_p. The gate capacitances and the addition energy are of the same order of magnitude as those presented above for the quantum dot defined by etched trenches and gates. The electric diameter of the dot was determined to be 280 nm assuming the dot to be circular, which suggests that the lateral depletion below the gates is minimal. One advantage of using this design compared to the etch defined dot is that the thin top gate electrodes offer more local control of the tunnel coupling to the quantum dot and do not

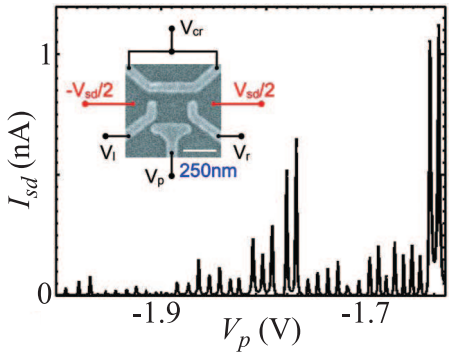

Figure 3.6: Coulomb oscillations in the current through a top-gate-defined quantum dot device as a function of V_p. The inset shows a scanning electron microscope image of the quantum dot device.

require precise alignment to any underlying etched structures. Additionally, the thin layer of HfO_2 greatly improves the coupling of the gate to the 2DEG underneath compared to the thick cross-linked PMMA layer.

3.3 Transport in few-electron quantum dots

Few-electron quantum dots are excellent systems in which to study few-electron interactions, and spin and correlation effects. To tune a quantum dot to the few-electron regime it is necessary to have good control of the potential on the dot and of the tunnel barriers. The circular quantum dot and the top-gated dot presented in the previous section were not successfully tuned to the few-electron regime, since applying increasingly negative voltages to deplete the dot would inevitably lead to pinch-off of the tunnel barriers. To solve this problem the device was redesigned.

Figure 3.7(a) shows a scanning electron microscope image of the central device region of the new few-electron quantum dot device. The circular shape of the dot has been changed to a quantum wire with a width of 150 nm. The in-plane gates used to tune the dot potential and tunnel barriers have been replaced by five very thin local finger Ti/Au gates that wrap around the quantum wire. The metal gates have a width of ∼40 nm and a periodicity of 80 nm, allowing for more efficient local gating [46, 47]. The thick cross-linked PMMA dielectric layer has been replaced by a 20 nm thin film of HfO_2. HfO_2 has a high dielectric constant greatly improving the gating efficiency.

To form a few-electron quantum dot it is critical to find the appropriate

potential profile in the quantum wire such that the quantum dot can be depleted while the tunnel barriers are not pinched off. The optimal operating point is typically found by measuring the conductance through the device in the linear response regime as a function of the two barrier gates, for instance V_{lg3} and V_{lg5}, while keeping the plunger gate, V_{lg4} in this case, fixed and the remaining gates grounded. This conductance map can then be used to determine the pinch-off voltages of the barrier gates and to find a good operating point. A charge stability diagram is then plotted and used to determine whether or not the quantum dot can be depleted. An invaluable aid in determining the number of electrons in the quantum dot is a quantum point contact charge sensor (see Section 5.3 for a detailed description). In the described below measurements a charge sensor was used to verify the absolute charge state of the quantum dot.

Figure 3.7(b) shows the charge stability diagram on a logarithmic color scale for the device in Figure 3.7(a) where a quantum dot is formed between lg3 and lg5, with $V_{lg3} = -280$ mV and $V_{lg5} = -380$ mV, using V_{lg4} as a plunger gate to deplete the quantum dot. The measurements were performed in a dilution refrigerator at a temperature of about 100 mK. The absolute number of electrons in the dot (N) is indicated in the figure for the even Coulomb diamonds. Note the strong odd-even effect related to two-fold spin degeneracy where the odd occupation Coulomb diamonds have a small addition energy and the even occupation Coulomb diamonds have a large addition energy. Consequently, it can be deduced that the charging energy and single-particle level spacing are similar in size. The size of the small diamonds shows that the charging energy in the few-electron regime, ~ 4 to 6 meV, is several times larger that that of the many-electron dot described in Section 3.2. This is related to the smaller size of the few-electron dot. It can also be noted that the constant interaction model breaks down in the few-electron regime since the charging energy, and therefore C_Σ, changes with electron occupation.

Below the $N = 1$ Coulomb diamond the charge transition borders open up and no more diamonds are seen in the transport through the dot or in the charge sensor, confirming that the first few orbital states can be accessed. Figure 3.7(c) shows a schematic reconstruction of the electrochemical potential of the quantum dot levels based on Figure 3.7(b). The two-fold degenerate single-particle level index n and spin states spin-$\uparrow$ and spin-$\downarrow$ are used to denote the quantum dot energy levels.

3.3.1 Excited state spectroscopy

So far only transport through the ground states of the quantum dot has been discussed. For finite biases however, it is possible for excited states to con-

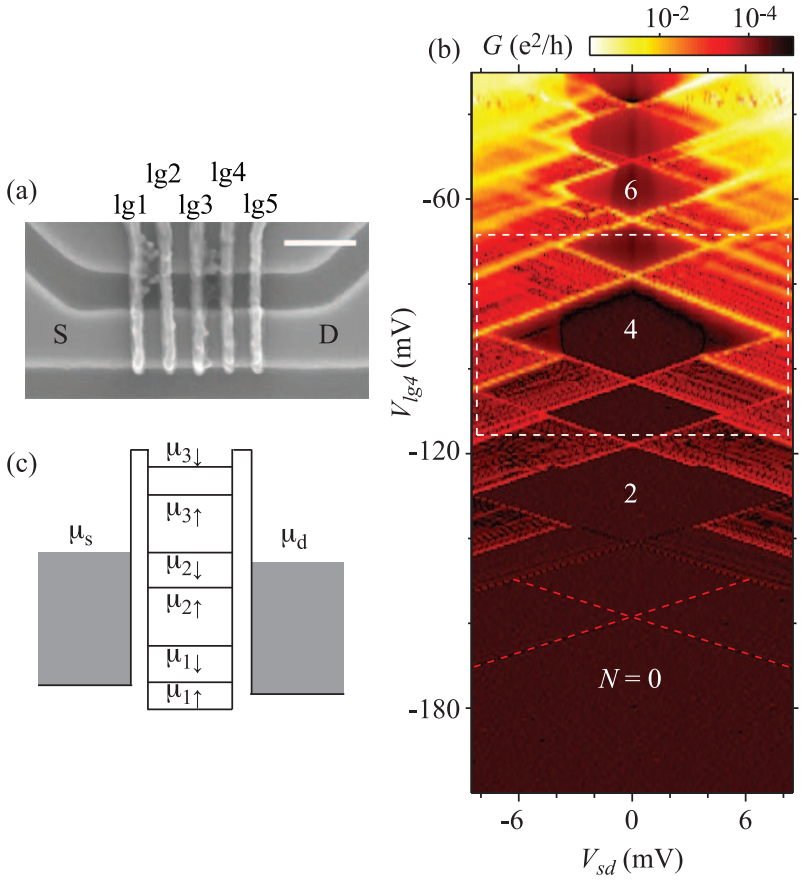

Figure 3.7: (a) Scanning electron microscope image of a few-electron quantum dot device. Negative voltages are applied to two of the gates to induce tunnel barriers in the wire to form a few-electron quantum dot. A third gate is used to tune the dot potential. The scale bar is 200 nm. (b) Charge stability diagram showing differential conductance as a function of gate voltage V_{lg4} and source-drain voltage V_{sd} for a few-electron quantum dot formed between gates lg3 and lg5. (c) Schematic energy level diagram showing the first three spin-degenerate levels of the few-electron quantum dot in (b).

tribute to electron transport. Few-electron quantum dots have pronounced excited state spectra due to the large single-particle level spacing. This can be seen in Figure 3.7(b) as lines of high differential conductance running outside and parallel to the ground state Coulomb diamond borderlines. The excited states are more clearly seen in Figure 3.8(a), which shows a close-up of the white dashed region in Figure 3.7(b) showing the $N = 3$ and $N = 4$ charge states. The differential conductance peaks associated with transport through excited states are indicated by green and blue arrows. It should be pointed out that transport through the quantum dot in this configuration is still sequential, meaning that electrons tunnel in and out of the dot one at a time. However, the presence of additional transport paths through excited states increases the tunneling probability and thus results in a peak in the differential conductance.

Figure 3.8(b) shows a schematic reconstructed charge stability diagram based on Figure 3.8(a), where the green and blue lines in (b) correspond to the excited states indicated by arrows of the same color in (a). The excited state lines have been extended to a larger gate voltage range for clarity. The green and blue dashed lines inside the Coulomb diamond indicate that the excited states are inaccessible due to Coulomb blockade.

Figure 3.8(c) shows schematic energy level diagrams corresponding to points A and B in Figure 3.8(b). The activation of transport through the excited states can identified in detail based on this figure. At point A the electrochemical potential of the drain (μ_d) aligns with the spin-degenerate ground state ($\mu_{2,\uparrow\downarrow} = \mu_{2,\uparrow} = \mu_{2,\downarrow}$) corresponding to single-particle level $n = 2$, whereas the electrochemical potential of the source (μ_s) aligns with the spin-degenerate excited state $\mu_{3,\uparrow\downarrow}$ corresponding to single-particle level $n = 3$. Thus, in this configuration the bias voltage, eV_{sd}, is equal to the single particle spacing, $\Delta\epsilon_3$. From point B two transport paths are available. The electrochemical potential of the drain, μ_d, align with the $\mu_{2,\downarrow}$ state forming one transport path. A spin-$\downarrow$ electron tunneling into this state will form a two-electron singlet state (total spin $S = 0$) with the spin-$\uparrow$ electron permanently occupying the $\mu_{2,\uparrow}$ state. The second transport path involves the excited state $\mu_{3,\uparrow}$. A spin-$\uparrow$ electron tunneling into this state will form a two-electron triplet state (total spin $S = 1$) with the spin-$\uparrow$ electron permanently occupying the $\mu_{2,\uparrow}$ state. Hence, the bias voltage is equal to the so-called singlet-triplet splitting energy ($\Delta\epsilon_{3,st}$) given by the single particle spacing and exchange energy. For a more detailed discussion of singlet states, triplet states and the exchange energy see Section 3.5. A value of $\Delta\epsilon_3 = 4.3$ meV for the single-particle spacing was extracted from the experimental data in figure 3.8(a).

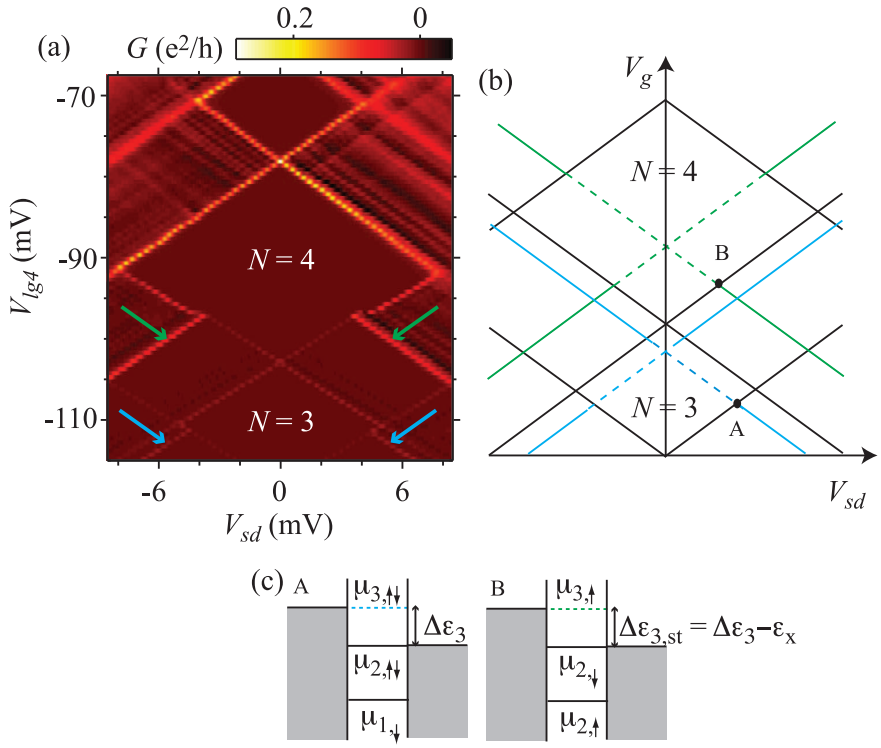

Figure 3.8: (a) Charge stability diagram on a linear color scale showing the region within the white dashed lines in Figure 3.7(b). Green and blue arrows indicate transport through excited states of the few-electron quantum dot. (b) Schematic charge stability diagram showing the Coulomb blockade borderlines (black) and excited state borderlines (green and blue). (c) Schematic energy diagrams depicting configurations A and B in (b). A marks the point where transport through both the $n = 2$ ground state ($\mu_{2,\uparrow\downarrow}$) and $n = 3$ excited state ($\mu_{3,\uparrow\downarrow}$) are possible. B indicates the point where transport through the $n = 2$ singlet ground state ($\mu_{2,\downarrow}$) and the $n = 3$ triplet excited state $\mu_{3,\uparrow}$ is possible.

3.3.2 Lead states

In Figure 3.7(b) and Figure 3.8(a) additional densely spaced peaks and dips of differential conductance outside of the Coulomb diamonds can be seen. Upon comparing the spacing of the peaks and dips to the single-particle level spacing it is clear that these states do not stem from states on the dot itself. The densely spaced states originate in the leads to the source and drain due to reduced dimensionality of the density of states. The leads of the device seen in Figure 3.7(a) are two-dimensional or quasi one-dimensional without any voltage applied to the gates. Applying a negative gate voltage to induce tunnel barriers will lead to the formation of one-dimensional sub-bands in the leads. Fluctuations in the density of states caused by the formation of these sub-bands will give rise to increased or decreased probabilities of electrons tunneling into or out of the dot.

In nanowire quantum dots contacted with metal leads these lead states are not visible due to the non-fluctuating density of states of the metal contact.

3.4 Zeeman effect and spin filling

In order to investigate spin-dependent transport properties in detail it is necessary to perform measurements with finite external magnetic fields. At zero magnetic field states with different spins ($s = \pm 1/2$) belonging to the same orbital are degenerate. In finite fields, however, the spin states will split in energy due to the Zeeman effect [48, 49]. If no other interactions are taken into account the Zeeman splitting is linear and the magnitude of the splitting is given by the effective g-factor , g^*, and the Bohr magneton, μ_B. The free-electron g-factor is close to 2, but can vary in semiconductors due to the periodic potential of the crystal. Additionally, the effective electron g-factor varies greatly for different semiconductors [50].

The device investigated here is similar to the device described in section 3.3 but the gate period is 100 nm and the gate dielectric is a 150-200 nm thick layer of cross-linked PMMA. A quantum dot was formed by applying negative gate voltages to lg2 and lg4 while using lg3 as a plunger gate to change the electron occupation of the dot. Because of the longer gate period and thicker dielectric layer this particular device was not successfully tuned to the final charge state of the dot. The device also lacked a functioning charge sensor. Figure 3.9(a) shows the charge stability diagram for the device measured at a temperature of about 100 mK at zero magnetic field in a dilution refrigerator. The alternating large and small diamonds indicate that the dot is in the few-electron regime. However, the addition energy is slightly

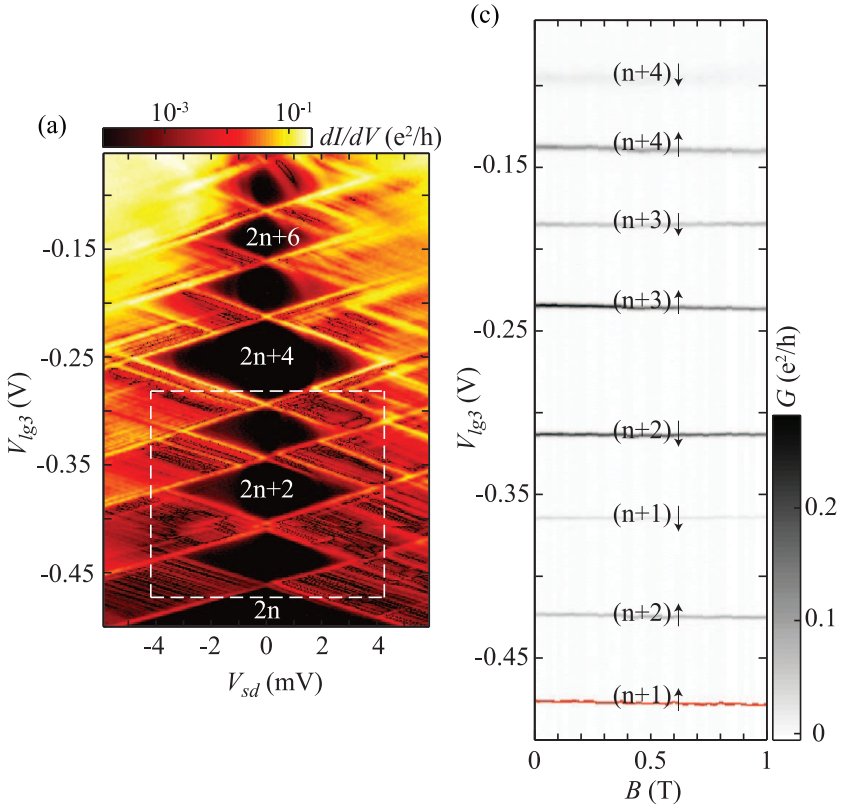

Figure 3.9: (a) Charge stability diagram on a logarithmic color scale. The electron occupation is indicated by the level index n. (b) Magnetic field evolution of the Coulomb blockade peaks in (a) in the linear response regime. The conductance peaks are labeled using level index n and spin state.

smaller than in the device shown in Figure 3.7 indicating that the electric size of the dot is larger in this device. The electron number is indicated in the figure using the orbital index n. The absolute number of electrons in the dot is, however, not known.

Figure 3.9(b) shows the magnetic field evolution of the Coulomb blockade peaks of the corresponding diamonds in Figure 3.9(a) on a gray-scale conductance plot. To avoid magnetic-field-induced orbital interactions the external magnetic field (B) was applied parallel to the 2DEG plane. According the the Zeeman effect, the energy splitting of electrons with different spins occupying states belonging to the same orbital is given by:

$$\Delta E_{Zeeman}(B) = |(s_\uparrow - s_\downarrow) g_n^* \mu_B B| \tag{3.20}$$

where μ_B is the Bohr magneton, g_n^* is the level-dependent effective g-factor and $s_\uparrow = 1/2$, $s_\downarrow = -1/2$ are the spin states of the electrons. In Figure 3.9(b) the levels are labeled by the level index and spin state assuming a negative g-factor for InGaAs [51]. In a typical spin-filling sequence with alternating filling of spin-$\uparrow$ and spin-$\downarrow$ electrons, it would be expected that the two conductance peaks located just above and below an odd-number electron Coulomb diamond would be split with increasing magnetic field according to:

$$\Delta E(B) = \Delta E(0) + \Delta E_{Zeeman}(B) = \Delta E(0) + |g_n^* \mu_B B|. \tag{3.21}$$

For an even-number electron Coulomb diamond, the energy difference of the two corresponding conductance peaks would be given by:

$$\Delta E(B) = \Delta E(0) - |g_n^* \mu_B B|/2 - |g_{n-1}^* \mu_B B|/2 \tag{3.22}$$

leading to the movement of the two associated peaks closer to each other as the magnetic field is increased. However, the peaks in Figure 3.9(b) do not show this dependence on the magnetic field. Here, some neighboring peaks show little or no relative change in position as a function of magnetic field, whereas other neighboring peaks do show a change.

This can be more clearly seen in Figure 3.10(a) where the energy difference between neighboring peaks is plotted. The gate voltage in this figure was converted to energy by extracting the lever arm for lg3 from the charge stability diagram in Figure 3.9(a). Plots showing the energy difference $\mu_{(n+2)\uparrow} - \mu_{(n+1)\uparrow}$ and $\mu_{(n+2)\downarrow} - \mu_{(n+1)\downarrow}$ show very little magnetic field dependence suggesting that the two states involved in these plots have the same spin. From the slopes in Figure 3.10(a) the spin-filling sequence of the few-electron quantum dot in the linear response regime can be deduced to

be $(n+1)\uparrow$,$(n+2)\uparrow$,$(n+1)\downarrow$,$(n+2)\downarrow$,$(n+3)\uparrow$,$(n+3)\downarrow$,$(n+4)\uparrow$,$(n+4)\downarrow$, from the lowest-lying state to the highest-lying one in Figure 3.9(a) and (b). The small energy shifts $\mu_{(n+2)\uparrow} - \mu_{(n+1)\uparrow}$ and $\mu_{(n+2)\downarrow} - \mu_{(n+1)\downarrow}$ as a function of magnetic field originate from orbital-dependent g-factor fluctuations.

The spin-filling sequence observed here can be explained if the two single-particle orbital levels involved are degenerate or nearly degenerate, and the exchange interaction, (see next section,) between electrons favors parallel spin filling, forming a triplet ground state, instead of alternating spin filling with a singlet ground state. The origin of the degeneracy is probably the two-dimensional nature of the quantum dot which enables orbitals with different spacial extensions to have similar energies.

In Figure 3.10(b) the energy differences between conductance peaks belonging to the same orbital state or neighboring orbital state but with opposite spin are plotted. An increase in energy difference can be seen with increasing magnetic field for peaks that belong to the same orbital, while the energy difference of peaks belonging to neighboring orbitals with different spins decreases with increasing magnetic field. The observed behavior is in agreement with Equations 3.21 and 3.22. Linear fits to the data in Figure 3.10(b) yield the level-dependent effective g-factors $|g^*_{n+1}| = 2.7$, $|g^*_{n+2}| = 2.1$, $|g^*_{n+3}| = 2.7$ and $|g^*_{n+4}| = 4.0$.

Similar magnetic field analysis was performed for the top-gated many-electron lateral quantum dot seen in Figure 3.6 (Paper III) and for the few-electron InSb nanowire quantum dot described in Paper V. Contrary to the few-electron InGaAs quantum dot described above, the Coulomb peaks show a relation with increasing magnetic field consistent with antiparallel spin filling (singlet ground states), consistent with Equations 3.21 and 3.22. Fitting peaks belonging to three orbital levels gave $|g^*_{m+1}| = 0.9$, $|g^*_{m+2}| = 1.8$, and $|g^*_{m+3}| = 2.1$, where m is the orbital level index for the top-gated lateral quantum dot. The material composition of the quantum dot is similar to that in the structure described above, i.e. an InGaAs/InP heterostructure, thus giving roughly similar values of the g-factors. The InSb nanowire quantum dot, however, has very large g-factors. From the evolution of the Coulomb blockade peaks belonging to the first five orbital levels of the quantum dot with increasing magnetic field the values $|g^*_1| = 52$, $|g^*_2| = 39$, $|g^*_3| = 31$, $|g^*_4| = 29$ and $|g^*_5| = 63$ were obtained. These values are to the best of the author's knowledge the largest that have been measured in semiconductor quantum dots.

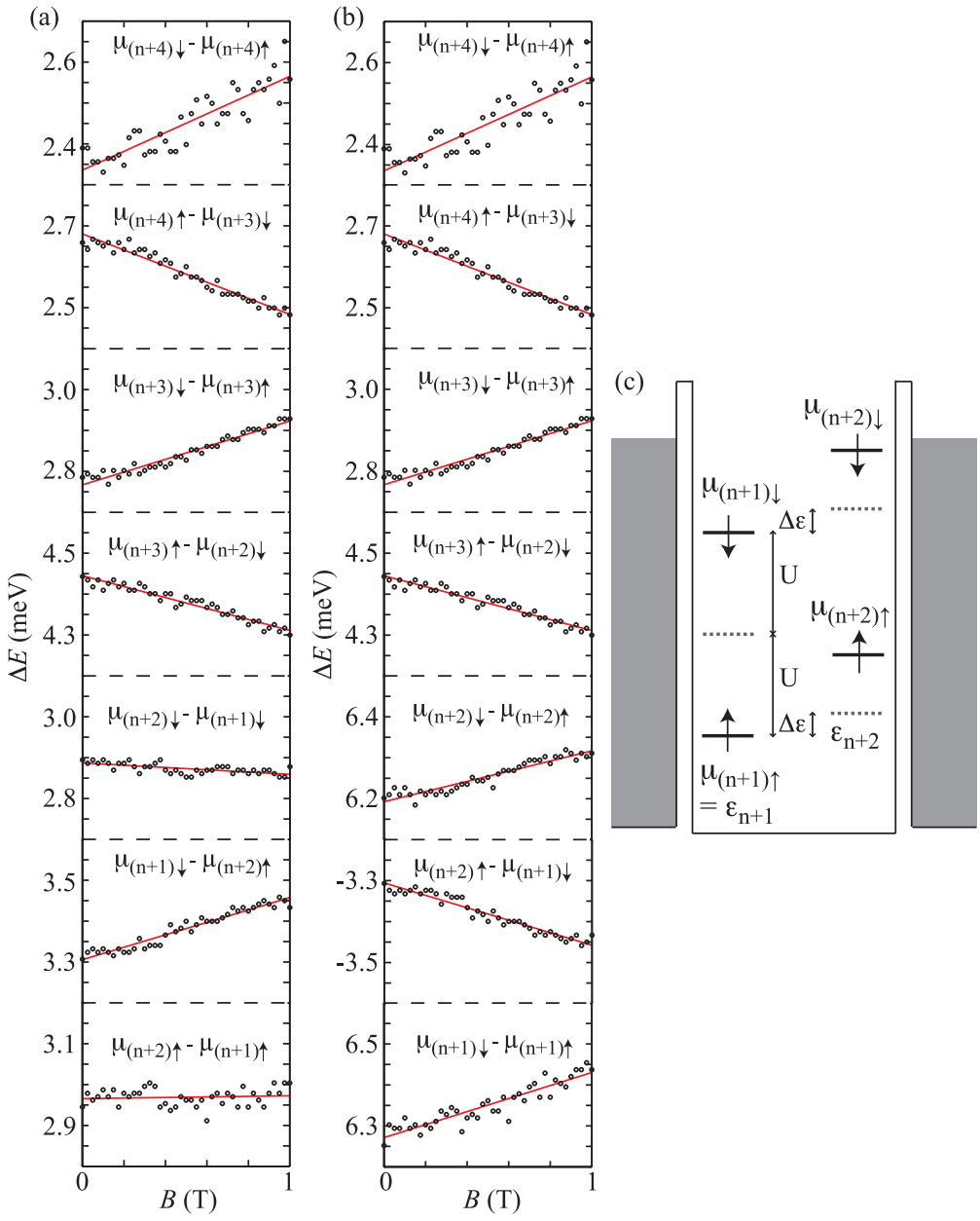

Figure 3.10: (a) and (b) Evolution of the energy difference between the measured conductance peaks shown in Figure 3.9(b) with increasing magnetic field. The orbital level and spin indices of the two associated states are indicated in each plot. (c) A simple model showing the four energy states of the dot responsible for transport in the region indicated by the dashed box in Figure 3.9(a).

3.5 Exchange interaction

The exchange interaction arises from the Scrödinger equation, and is a term that lowers the energy of states with parallel spin configurations. The exchange interaction is responsible for Hund's rule for spin filling in atoms. Spin filling according to Hund's rule has also been observed in few-electron quantum dots [52].

In quantum dots the exchange interaction has a significant influence on electron transport properties since it determines the spin filling sequence [53, 54, 48]. The energy gained by a system from adding electrons with parallel spins rather than antiparallel spin is called the exchange energy, i.e. the energy gained by going from a singlet ground state to a triplet ground state. For parallel spin filling to occur in the ground state of a quantum dot the exchange energy must overcome the single-particle splitting of the orbitals involved. This may happen if the orbital levels are degenerate or nearly degenerate. In this case the exchange interaction can push one electron into a higher orbital state thus lowering the two-electron ground state energy if the spins of the two electrons are parallel.

To estimate the contribution of exchange energy to the quantum dots studied here let us consider the parallel spin filling observed for the four energy states in the dashed region in Figure 3.9(a), which was discussed in the previous section. Figure 3.10(c) shows a schematic energy diagram of the same four states. Assuming a constant charging energy U of the system we can write:

$$\mu_{(n+1)\downarrow} - \mu_{(n+1)\uparrow} = 2U, \tag{3.23}$$

$$\mu_{(n+2)\uparrow} - \mu_{(n+1)\uparrow} = \Delta\epsilon + U - |\epsilon_{x,\uparrow\uparrow}|, \tag{3.24}$$

$$\mu_{(n+2)\downarrow} - \mu_{(n+1)\downarrow} = \Delta\epsilon + U - |\epsilon_{x,\downarrow\downarrow}|, \tag{3.25}$$

where $\Delta\epsilon = \epsilon_{n+2} - \epsilon_{n+1} \geq 0$ is the single-particle level spacing, and $\epsilon_{x,\uparrow\uparrow}$ and $\epsilon_{x,\downarrow\downarrow}$ are the exchange energies of the two spin-$\uparrow$ electrons and two spin-$\downarrow$ electrons, respectively. The constant charging energy U can be deduced to be 3.54 meV using Figure 3.9(a) and Equation 3.23. If the single-particle level spacing is known, Equations 3.24 and 3.25 can be used to determine the exchange energies $\epsilon_{x,\uparrow\uparrow}$ and $\epsilon_{x,\downarrow\downarrow}$. However, it was not possible to determine the single-particle level spacing from the excited state spectroscopy and it is only possible to determine the lower bound of the exchange energy: $|\epsilon_{x,\uparrow\uparrow}| = 210\ \mu\text{eV}+\Delta\epsilon$ and $|\epsilon_{x,\downarrow\downarrow}| = 430\ \mu\text{eV}+\Delta\epsilon$.

As was suggested in Section 3.4, the exchange energy may also be determined from excited state spectroscopy. From the schematic in Figure 3.8(c) it can be seen that the singlet-triplet splitting energy $\Delta\epsilon_{3,st}$ is given by the

single-particle spacing, $\Delta\epsilon_3$, and the exchange energy, ϵ_x, between the two electrons involved according to $\Delta\epsilon_{3,st} = \Delta\epsilon_3 - \epsilon_x$. Using the experimentally determined values of $\Delta\epsilon_3$ and $\Delta\epsilon_{3,st}$ gives the value $\epsilon_x = 0.9$ meV.

3.6 Spin-orbit interaction

An electron moving in an electric field will experience a magnetic field which will act on the spin of the electron, the so-called spin-orbit interaction. The spin-orbit interaction can be introduced into the Scrödinger equation in the form of a relativistic correction: $H_{so} = (\hbar/4m^2c^2)(\nabla V \times \overrightarrow{p}) \cdot \overrightarrow{\sigma}$, where m is the electron mass, c is the speed of light, V is the potential landscape, $\overrightarrow{p}$ is the electron momentum and $\overrightarrow{\sigma}$ is the Pauli operator. In III-V semiconductors two sources of spin-orbit interaction can be distinguish. The first contribution is from the asymmetric crystal potential in materials with zincblende crystal structures. This contribution is called the Dresselhaus term. The second contribution to spin-orbit interaction is the Rashba term, which arrises from asymmetry in the confining potential of the electrons. The consequences of the spin-orbit interaction in semiconductor quantum dots are the negative g-factors and the g-factor fluctuations [55, 56, 57, 58, 59] described in Section 3.4. Fluctuations in the g-factors are expected to occur when the non-vanishing spin-orbit interaction energy (Δ_{so}) is much smaller than the single-particle level separation $\Delta\epsilon$, i.e. $\Delta_{so} << \Delta\epsilon$.

The spin-orbit interaction tends to be stronger for heavy III-V compounds with a narrow band gap, making InSb nanowire quantum dots an excellent system in which to study these effects. The quantum dot device was fabricated by contacting an InSb nanowire segment with two Ti/Au electrodes with widths of 150 nm according to the procedure described in Section 2.2.2. The nanowire had a diameter of 70 nm and the contacts had a separation of 160 nm. The tunnel barriers to the quantum dot were formed at the metal-semiconductor interface. Measurements were performed in a ^{3}He cryostat at a temperature of 300 mK.

Orbital interactions were investigated in the excited state spectrum of the quantum dot in order to directly determine the spin-orbit interaction energy. Figure 3.11(a) shows the differential conductance (dI/dV_{sd}) as a function of source-drain voltage (V_{sd}) and back gate voltage (V_{bg}) for the device. From this charge stability diagram an average charging energy of $U = 5.7$ meV and an average level spacing of $\Delta\epsilon = 2.6$ meV were determined. The g-factors determined from magneto-transport measurements on this quantum dot are much larger than those found in InGaAs quantum dots; i.e. with values up to $|g^*| = 76$ which were strongly level dependent. Figure 3.11(b) shows the dif-

ferential conductance along cut A in Figure 3.11(a) as a function of magnetic field. The cut was made such that only transport through the N-electron ground state and spin-degenerate first excited state was possible. The N-electron singlet ground state formed by adding a spin$\downarrow$ electron to the dot is labeled $\downarrow$ and the first excited spin-up state is labeled $\Uparrow$. The first excited spin-down state is labeled $\Downarrow$. The spin-down states $\downarrow$ and $\Downarrow$ will move up in energy while the spin-up state $\Uparrow$ will move down in energy with increasing magnetic field. At $B = 2.6$ T the spin-up excited state and spin-down ground state will hybridize and form an avoided level crossing. This anti-crossing indicates a mixing of the two orbitals stemming from spin-orbit interaction in the dot [60, 61]. Figure 3.11(c) shows the ground state and excited state energy level positions near the anti-crossing in Figure 3.11(b). The spin-orbit energy $\Delta_{so} = 280$ μeV was extracted from the anti-crossing gap by fitting the experimental data to a two-level perturbation model. The small spin-orbit energy compared to the level separation supports our previous assumption that the spin-orbit interaction is responsible for the strong dependence of the g-factors on the single-particle levels.

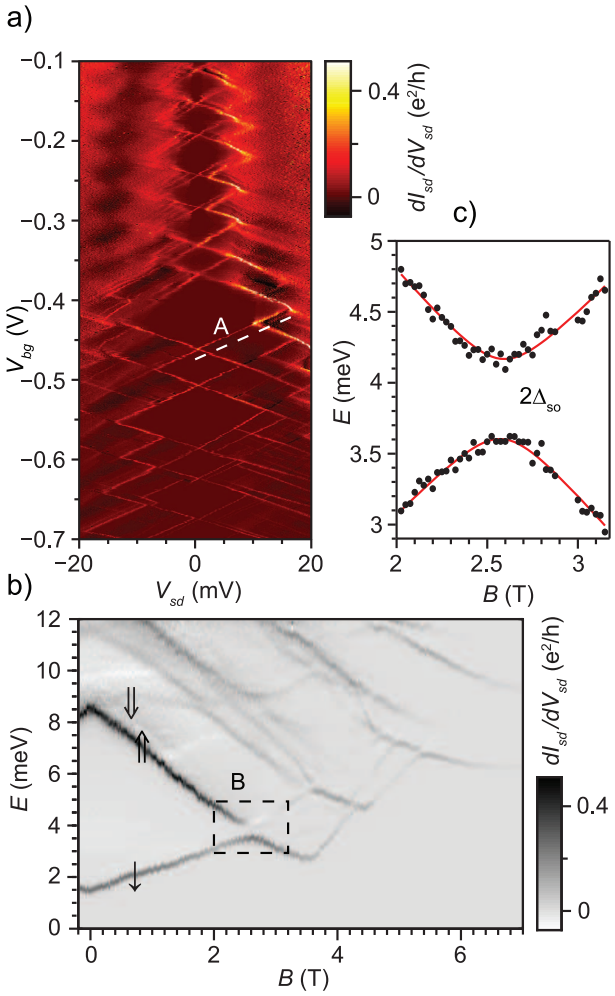

Figure 3.11: (a) Charge stability diagram showing transport through a few-electron quantum dot formed in an InSb nanowire segment. (b) Differential conductance along cut A in (a) as a function of magnetic field. The ground state is labeled $\downarrow$. The spin-up excited state is labeled $\Uparrow$ and the spin-down excited state is labeled $\Downarrow$. (c) Close-up of the area marked by the dashed black line in (b). The experimentally determined positions (dots) of the ground state and spin-up excited state are plotted as a function of magnetic field. The red curves show the result of theoretical calculations based on a two-level model including spin-orbit interaction.

Chapter 4

Correlation effects in single quantum dots

Correlation and spin correlation effects in single quantum dots are discussed in Papers V, VI and VII. This chapter introduces the concept of higher-order tunneling processes that can not be explained by the sequential transport picture discussed in Chapter 3. These higher-order tunneling effects are referred to as *co-tunneling* since the tunneling process involves simultaneous tunneling of two (or more) interacting electrons.

In Section 4.1 the lowest-order co-tunneling events are considered whereas Sections 4.2 and 4.3 deal with higher-order co-tunneling events where the spin of the electrons is taken into account. Section 4.4 deals with induced current suppression in the case of degeneracy of levels with equal spins.

4.1 Co-tunneling

The previous chapter described sequential transport processes through one or several levels in a quantum dot, where all intermediate states of the tunneling electrons were energetically allowed. Co-tunneling, on the other hand, involves tunneling through energetically forbidden states, so-called *virtual* states. Tunneling through virtual states is possible if the timescale of the process is short enough to be allowed by the uncertainty relation. To observe co-tunneling it is therefore essential to have strong source and drain tunnel coupling so that the tunneling times are of the same order as the timescale defined by the uncertainty relation.

We now consider the lowest-order co-tunneling process [62]. Figure 4.1(a) shows a schematic energy diagram of a quantum dot in a Coulomb blockaded configuration. In the picture of sequential transport no current will flow in

this configuration. However, if we consider two electrons tunneling in and out of the dot simultaneously via an intermediate, energetically forbidden, virtual state and the μ_N ground state a finite current may flow. Since the total energy of the initial and final states are equal this process is called *elastic* co-tunneling. Elastic co-tunneling causes a small current inside the Coulomb diamond, see the light gray and dark gray regions in the schematic stability diagram in Figure 4.1(c).

If the applied bias is equal to or larger than the lowest excited state for the N-electron dot it is possible to drive co-tunneling processes via the excited state μ_N^*. Figure 4.1(b) shows a schematic energy diagram for a Coulomb blockaded quantum dot with an applied bias equal to the excitation energy $\Delta\epsilon$. Here, an electron occupying the ground state can tunnel into the right lead and an electron on the left lead can tunnel into the quantum dot and populate the excited state μ_N^*. In this process energy is not conserved since the quantum dot is left in an excited state. This process is called *inelastic* co-tunneling and leads to an increase in current in the Coulomb diamond for biases greater than $\Delta\epsilon$, see the dark gray regions in figure 4.1(c). Since inelastic co-tunneling is dependent only on the bias voltage and not the gate voltage, the onset of inelastic co-tunneling will run parallel with the gate voltage axis at a constant bias voltage corresponding to $\Delta\epsilon$.

Figure 4.1(d) shows the charge stability diagram of a few-electron quantum dot on a logarithmic color scale where the source and drain coupling are relatively strong. The onset of inelastic co-tunneling via an excited state is indicated by dashed vertical lines.

4.2 Spin-1/2 Kondo effect

The Kondo effect was first discovered in the 1930s when researchers found that the resistance of metals containing a small amount of magnetic impurities increased below a critical temperature. The effect was not explained until 1964 when J. Kondo [63] found that it was caused by scattering of the spins of the conducting electrons via the magnetic impurities.

In quantum dots, the conventional Kondo effect, the so-called spin-1/2 Kondo effect, manifests itself as an increase in the conductance in the Coulomb blockade regime for odd charge states below a characteristic temperature, the so-called Kondo temperature, T_K [64, 65, 34]. Here, the single unpaired spin on the quantum dot acts as a magnetic impurity and introduces coherent spin-flip processes that drive current through the quantum dot. The increase in conductance seen in quantum dots, as opposed to the increase in resistance seen in dilute magnetic metals, can be interpreted as forward scattering of

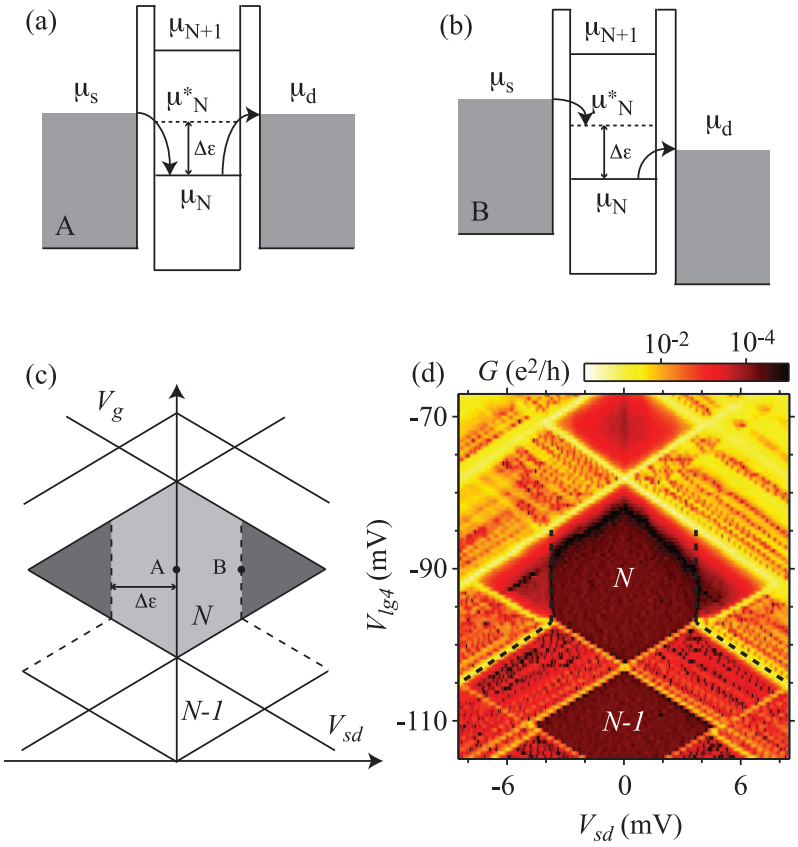

Figure 4.1: (a) Schematic energy diagram for a Coulomb blockaded quantum dot. Elastic co-tunneling via the ground state, μ_N, and a virtual state will result in a finite current through the device. (b) Schematic energy diagram for a Coulomb blockaded quantum dot with an applied bias corresponding to the level spacing of the first excited state. Inelastic co-tunneling via the first excited state, μ_N^*, will result in an increased current for $eV_{sd} \geq \Delta\epsilon$. (c) Schematic charge stability diagram showing regions where elastic co-tunneling (light gray) and inelastic co-tunneling (dark gray) are possible. The dashed lines inside the Coulomb diamond indicate the onset of inelastic co-tunneling. The dashed lines outside the Coulomb diamond indicate sequential transport through the lowest excited state of the N-electron quantum dot. (d) Charge stability diagram on a logarithmic color scale of a few-electron quantum dot with strong coupling to the source and drain leads. Inelastic co-tunneling in the Coulomb blockaded regime is seen for eV_{sd} greater than lowest excited state energy.

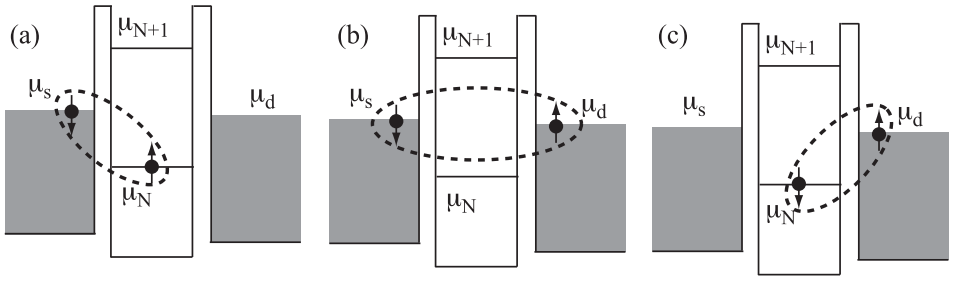

Figure 4.2: Schematic energy diagrams showing the mechanism behind the Kondo effect in a quantum dot. The three figures (a), (b) and (c) depict a tunneling event via a virtual state (b), whereby an unpaired spin-up electron occupying a spin-degenerate level tunnels to the drain contact and is replaced by a spin-down electron from the source contact.

electrons which reduces the resistance of the sample. The single localized unpaired spin on the quantum dot will form a singlet state with the delocalized spins in the leads. This macroscopic correlated singlet state will give rise to the Kondo effect. The Kondo effect is therefore observable only in the strong coupling regime where the interaction between the localized electron on the dot and the delocalized electrons on the leads is strong enough for the singlet state to form.

The mechanics behind the Kondo effect is schematically depicted in Figure 4.2. Figure 4.2(a) shows a single spin populating a spin-degenerate single-particle level on the quantum dot, thus blocking first-order tunneling. The unpaired spin will interact with the delocalized spins on the leads to form a singlet state. The localized electron may tunnel out of the dot into the right lead to form an energetically forbidden virtual state for a short time, see figure 4.2(b). A spin-down electron on the left lead may then tunnel into the dot, see figure 4.2(c). Note that the tunneling process of one electron from the left contact to the right contact will result in a spin flip of the localized electron and that the energy of the initial and final states are the same, i.e. the process is elastic. However, at finite bias the process is no longer elastic and the Kondo effect vanishes. In a quantum dot the Kondo effect can therefore be described as a narrow peak in the density of states at the electrochemical potential of the leads for $\mu_s = \mu_d$.

The manifestation of the Kondo effect in the transport through a quantum dot is a sharp differential conductance peak running through an odd Coulomb blockade diamond centered around zero bias. The characteristic temperature of the Kondo effect, T_K, can be determined from the full width at half maximum of the zero-bias differential conductance peak, $k_B T_K$. Fur-

thermore, the height of the Kondo peak has been shown to reach the unitary limit, $2e^2/h$ [66]. The Kondo temperature can also be estimated from the tunnel coupling according to:

$$T_K \sim \frac{\sqrt{h\Gamma U}}{2k_B} e^{-\pi U/4\Gamma h} \tag{4.1}$$

where $\Gamma = \Gamma_s + \Gamma_d$ is the total tunneling rate, and U is the on-site Coulomb repulsion energy or charging energy. Equation 4.1 is only valid in the middle of the Coulomb blockade diamond. Since the Kondo temperature depends exponentially on the tunnel coupling it is critical to operate in the strong coupling regime in order to observe the effect experimentally. However, the electron must be sufficiently localized to the dot for quantum dot to be formed.

The characteristic Kondo resonance at zero bias can be seen in Figure 4.3(a) which shows the $N = 9$ Coulomb diamond for the device shown in Figure 3.7(a) where the quantum dot is defined between lg3 and lg5 with $V_{lg3} = -250$ mV and $V_{lg5} = -415$ mV. Neighboring even diamonds do not show the Kondo resonance, which is in agreement with the theoretical prediction. Note that the coupling to source and drain are strong, which makes the diamond borders less pronounced. Figure 4.3(b) shows a trace along $V_{lg4} = -10$ mV, i.e. in the middle of the Coulomb blockade diamond of Figure 4.3(a). The Kondo peak in the differential conductance is clearly seen centered around zero bias. The maximum differential conductance here is roughly $0.4e^2/h$, which is far from the unitary limit. From the full width at half maximum of ~ 120 μV T_K can be determined to be 1.4 K. The tunneling rate, Γ, can be extracted from the Coulomb peaks in the linear response regime by fitting Equation 3.13 to the experimental data. The tunnel coupling $h\Gamma$ was estimated to be 1.0 meV. Using the tunnel coupling and the charging energy $U = 3.0$ meV determined from the $N = 9$ Coulomb diamond T_K was determined to be ~ 0.9 K using Equation 4.1. The discrepancy in the values of T_K determined with the two different methods probably arises from the estimation of the tunnel coupling, which has a considerable influence on the calculated Kondo temperature.

Figure 4.3(c) shows the current through the $N = 9$ charge state as a function of V_{lg4} for $V_{sd} = 25$ μV. The different curves correspond to different sample temperatures T. As the temperature increases the valley current decreases, a typical feature of the Kondo effect, which is contrary to the expected behavior of a Coulomb blockade valley, where broadening of the Coulomb blockade peaks leads to an increase in valley current. The Coulomb blockade peaks also shift apart from each other with increasing temperature, a feature that has been predicted theoretically [67]. Figure 4.3(d) shows

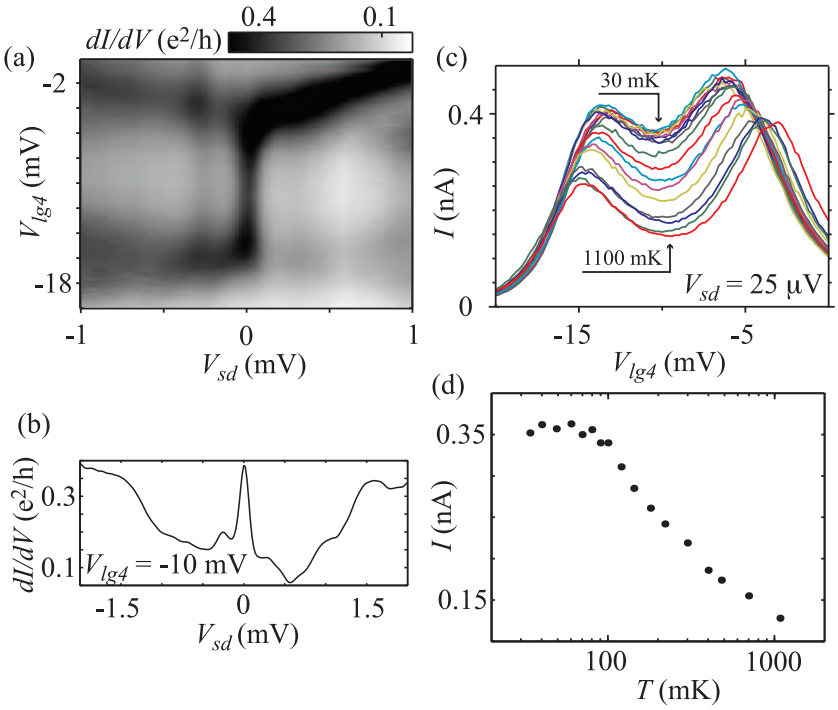

Figure 4.3: (a) Charge stability diagram showing a close-up of the $N = 9$ Coulomb diamond from Figure 3.7(b). The zero-bias Kondo resonance is clearly seen inside the Coulomb blockaded region. (b) Trace along $V_{lg4} = -10$ mV in (a) showing differential conductance versus V_{sd}. (c) Current as a function of V_{lg4} in the linear response regime for the $N = 9$ charge state. (d) Temperature dependence of the minimum valley current on a logarithmic temperature scale, measured in the linear response regime.

the minimum valley current as a function of temperature on a logarithmic temperature scale. The logarithmic temperature dependence seen here is also a typical feature of the Kondo effect [65]. The saturation of the valley conductance for $T < 100$ mK is probably caused by a saturation of the electron temperature in the sample studied in this work.

At finite magnetic fields the spin-degenerate level on the dot will split as a result of the Zeeman effect, as discussed in Section 3.4. The zero-bias Kondo resonance is then expected to vanish since the tunneling processes described in Figure 4.2 are no longer possible. However, the Kondo resonance may be restored by applying a source-drain voltage that matches the Zeeman splitting of the localized level, since the Kondo peak in the density of states at each chemical potential is expected to split by twice the Zeeman energy [68].

Experimentally, this means that the zero-bias Kondo resonance will split according to $eV_{sd} = \pm g_n^* \mu_B B$ for finite fields, where n is the single-particle level involved in the Kondo process. This can be seen in Figure 4.4(a) which shows the $N = 9$ diamond when an in-plane magnetic field of 2 T is applied. The Zeeman splitting of the Kondo peak is more clearly seen in Figure 4.4(b), which shows the trace at $V_{lg4} = -10$ mV from Figure 4.4(a). It is possible to determine the g-factor from the evolution of the Zeeman-split Kondo peaks with magnetic field. Figure 4.4(c) shows the Kondo peak position as a function of magnetic field. Linear fits to the peak positions give $|g_{5+}^*| = 2.4$ and $|g_{5-}^*| = 2.8$ for the peak at positive bias and negative bias Kondo peaks, respectively. These values compare well with the values determined from the ground state Zeeman splitting of a similar quantum dot described in Section 3.4.

4.3 Zero-field Kondo splitting

The large tunability of semiconductor quantum dots makes it possible to study variations of the Kondo effect that reveal new and interesting physics. These new Kondo variations include the two-stage Kondo effect [33], singlet-triplet Kondo-enhanced transitions for an even number of electrons on the dot [31, 32], the so-called orbital Kondo effect [69], and the two-channel Kondo effect [70]. The Kondo effect has been investigated in a quantum ring structure where it was found that the conductance resonance was modulated by the Aharonov-Bohm period [71]. The Kondo effect has also been studied in double quantum dot systems [72, 73], where bonding and anti-bonding states due to the superposition of the Kondo states on the two dots have been observed.

In this section, the way in which the $N = 9$ charge state Kondo resonance

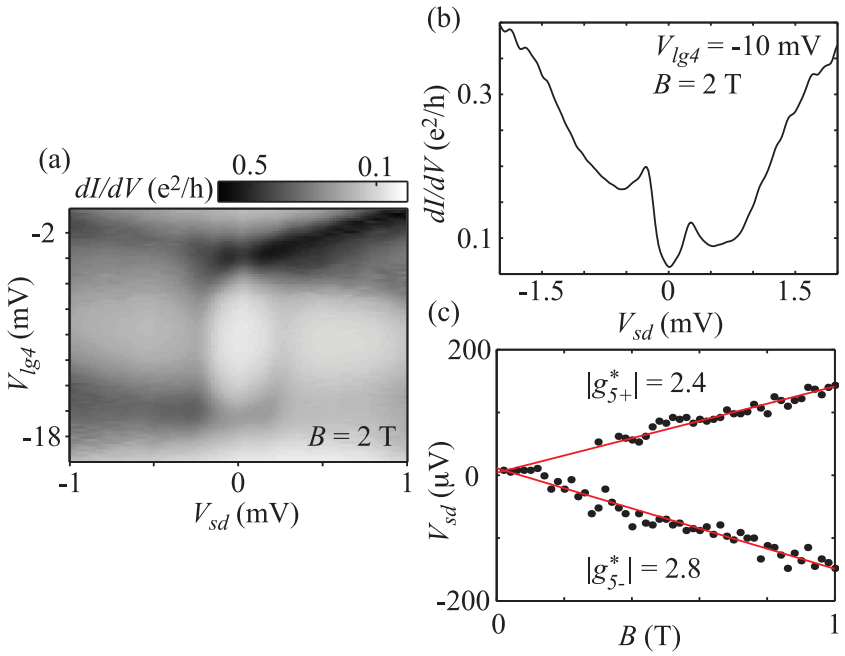

Figure 4.4: (a) Charge stability diagram for the $N = 9$ Coulomb diamond with an applied in-plane magnetic field of $B = 2$ T. (b) Trace along $V_{lg4} = -10$ mV from (a). (c) Position of the maximum Kondo peak for both positive and negative bias voltages as a function of applied magnetic field.

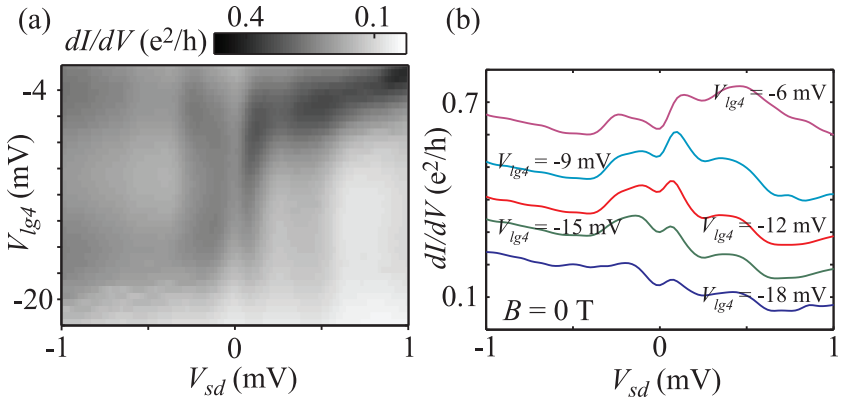

Figure 4.5: (a) Charge stability diagram for the $N = 9$ charge state with a lower tunnel barrier gate voltage asymmetry. A clear dip has developed in the broader Kondo resonance. (b) Traces for various gate voltages from (a).

discussed in the previous section changes with decreased asymmetry of the tunnel barrier gate voltages was investigated. The tunnel barrier gate voltage will not only effect the tunnel coupling but may also change the lateral shape of the quantum dot, which in turn gives rise to a different single-particle energy level spectrum. This change in the single-particle spectrum may in some cases lead to a singlet-to-triplet transition [74, 75, 54, 76, 77]. The reduced barrier gate voltage asymmetry may also effect the exchange coupling to nearby impurities [73, 78, 79, 80, 81].

Measurements will now be presented where the barrier gate voltage asymmetry was reduced. Voltages of $V_{lg3} = -260$ mV and $V_{lg5} = -405$ mV were used. Figure 4.5(a) shows the charge stability diagram for the $N = 9$ charge state Coulomb diamond without an applied magnetic field. A clear dip can be seen around zero bias inside the larger Kondo resonance. The splitting is more clearly seen in Figure 4.5(b), where traces are shown for various plunger gate voltages from (a). This system can be characterized by two low-energy scales, $k_B T_{K1}$ and $k_B T_{K2}$. Considering the middle of the Coulomb blockade region, $k_B T_{K1} = 400$ μeV is associated with the broader Kondo resonance while $k_B T_{K2} = 100$ μeV is associated with the dip around zero bias.

The magnetic field dependence of the split Kondo resonance at the middle of the Coulomb diamond, is shown in Figure 4.6(a). A clear increase in the splitting of the Kondo resonance can be seen at higher magnetic fields due to the Zeeman effect. For small fields the splitting shows more complex behavior. When plotting the zero-bias differential conductance as a function of magnetic field, as in Figure 4.6(b), a non-monotonic behavior with a maximum differential conductance at $B_{max} = \pm 225$ mT is observed (indicated

by the arrow in the figure). Using the average effective g-factor ($g_5^* = 2.6$) determined from the Zeeman splitting of the Kondo resonance in the previous section gives a corresponding Zeeman energy of $g_5^* \mu_B B_{max} \sim 30$ μeV. Plotting the differential conductance as a function of source-drain voltage V_{sd} for various magnetic fields [Figure 4.6(c)] shows that the single Kondo resonance is almost completely restored for $B = \pm 225$ mT. The small splitting observed at $B = \pm 225$ mT corresponds roughly to the expected Zeeman energy.

Temperature dependence of the differential conductance for different source-drain voltages at three different positions on the split Kondo peak was also investigated. Figure 4.6(d) shows the differential conductance for $V_{sd} = \pm 80$ μV and $V_{sd} = 0$ μV as a function of temperature on a logarithmic scale, measured at $V_{lg4} = -11$ mV. Here, $V_{sd} = \pm 80$ μV correspond to the two peaks in conductance of the split Kondo resonance. For the finite source-drain voltages $V_{sd} = \pm 80$ μV a logarithmic temperature dependence was observed, which is consistent with the Kondo effect. The temperature dependence for $V_{sd} = 0$ μV shows a vastly different behavior, where the observe dependence of the differential conductance with temperature is non-monotonic, with a maximum differential conductance at $T_{max} = 300$ mK (indicated by the arrow in the figure). This corresponds to a thermal energy of $k_B T_{max} \sim 30$ μeV. For $T > 300$ mK the data show a behavior similar to the conventional Kondo effect with a logarithmic temperature dependence. At high temperatures the peaks amplitudes approach each other, indicating that the two Kondo peaks merge due to thermal broadening.

The observed conductance dip inside the Kondo resonance and the non-monotonic dependence of the differential conductance as a function of magnetic field and temperature can be qualitatively explained by a two-step Kondo process. The first process produces an enhancement of the zero-bias conductance, which is then suppressed in a second step. If $k_B T_{K1} > k_B T_{K2}$, where $k_B T_{K1}$ and $k_B T_{K2}$ are energies associated with the first and second steps respectively, the resulting Kondo resonance will show a dip around zero bias. The underlying physical mechanism behind the two-step Kondo behavior in this odd-electron quantum dot is not yet fully understood. Two different physical mechanisms that could explain the observed behavior are proposed, namely the *two-stage* Kondo effect and the the *two-impurity* Kondo effect.

The two-stage Kondo effect is expected to occur in a quantum dot coupled to the source and drain leads through single channels with total spin $S \geq 1$ or for a singlet ground state with a nearby triplet excited state. It is therefore expected to be observed mainly in even-numbered Coulomb diamonds [82, 83, 84, 33, 76]. In quantum dots, spin configurations with $S = 1$

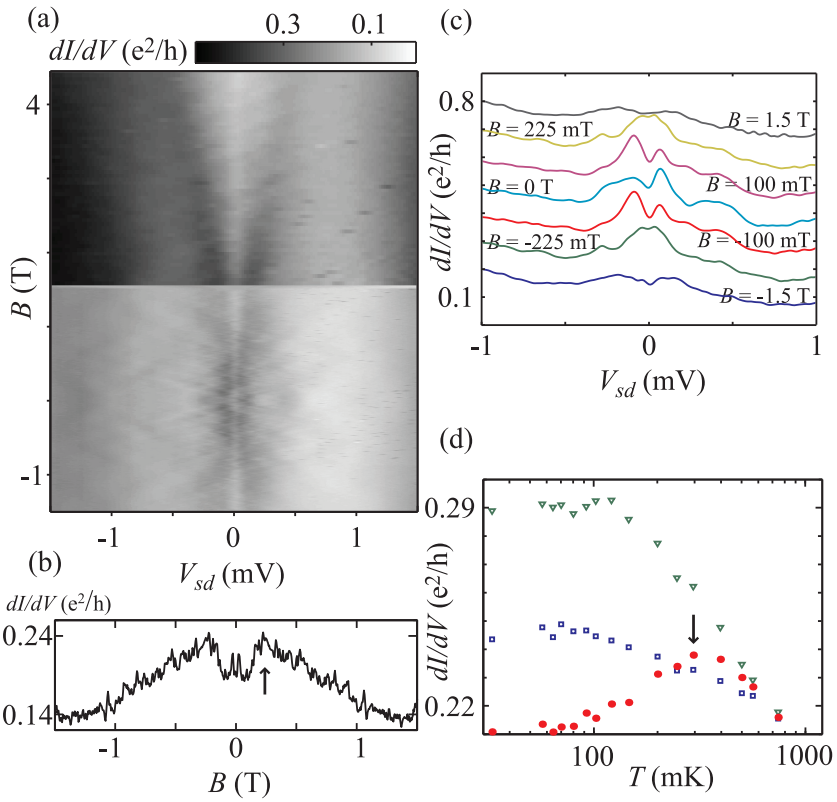

Figure 4.6: (a) Differential conductance as a function of magnetic field and source-drain voltage for $V_{g4} = -12$ mV for the split Kondo resonance. (For $B > 1.5$ T data from a different measurement were used.) (b) Zero-bias differential conductance as a function of magnetic field for $V_{g4} = -12$ mV. The arrow indicates B_{max}, which is the magnetic field at maximum differential conductance. (c) Traces for various magnetic fields from (a). Each trace has a 0.1 e^2/h offset for clarity. (d) Temperature dependence of the differential conductance of the split Kondo peak on a logarithmic temperature scale, measured at $V_{sd} = 80$ μV (green triangles), $V_{sd} = -80$ μV (blue squares) and $V_{sd} = 0$ μV (red circles) at $V_{lg4} = -11$ mV. The arrow indicates T_{max} for $V_{sd} = 0$ μV, which is the temperature at maximum differential conductance.

are possible if the exchange energy is greater then the orbital spacing, as discussed in Section 3.5. Transitions into higher order spin states, such as $S = 3/2$, are less likely but still possible [77]. Here, the transition into a higher order spin state would lead to splitting of the Kondo peak. One possible interpretation of the experimental observations is that the large exchange energy in this quantum dot, ~ 1 meV, together with the decreased barrier gate voltage asymmetry, drives the quantum dot into a $S = 3/2$ state. One major difference between the experimental work described in this thesis and previous theoretical work is that the dot in this work contains an odd number of electrons, whereas the system studied in references [82, 83, 84] contains an even number of electrons. However, the two-stage Kondo effect is predicted to exist for all $S > 1/2$ [82]. In addition to the split Kondo peak, the two-stage Kondo effect is predicted to manifest itself as a non-monotonic dependence of the differential conductance on temperature and magnetic field in the linear response regime. The findings of the present experimental studies are in qualitative agreement with these predictions.

Another possible mechanism that the two-step behavior is caused by is the two-impurity Kondo effect, in which two spins couple antiferromagnetically via the so-called Ruderman-Kittel-Kasuya-Yosida (RKKY) exchange interaction [73, 78, 79, 80, 81]. Here, one of the impurity spins is the unpaired spin on the quantum dot. The second impurity spin in the present single-dot system is probably an electron localized in a nearby trap state in the gate oxide. The exchange interaction between the two spins is tuned by the barrier gate voltages which leads to a gate-induced splitting of the Kondo resonance at certain voltages. This situation is similar to that presented in reference [81], where a gate-dependent exchange interaction with a trap state was used to tune the splitting of a spin-1/2 Kondo peak. The two spins, $\mathbf{S_1}$ and $\mathbf{S_2}$, will interact via an exchange interaction $\epsilon_x = J\mathbf{S_1} \cdot \mathbf{S_2}$. For antiferromagnetic coupling, the two spins will form a singlet state, locking the spin localized on the dot, thus suppressing the Kondo effect around zero bias. At higher biases, however, the system may change into a triplet state leading to reestablishment of the Kondo effect at the singlet-triplet degeneracy point. This will result in a peak in the differential conductance for biases $V_{sd} = \pm J/2$ [85]. Furthermore, the two-impurity Kondo effect is expected to show non-monotonic temperature and magnetic field dependence of the conductance in the linear response regime [78]. In this interpretation, the tunable Kondo splitting observed in the present work would correspond to a quantum phase transition between a spin-1/2 Kondo state and a two-spin singlet state as the RKKY interaction is tuned by the gate voltages.

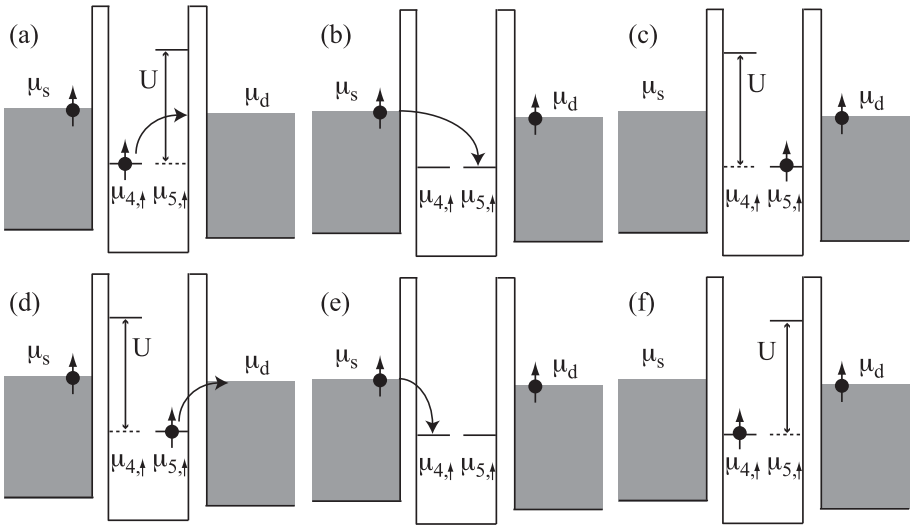

Figure 4.7: Schematic energy diagrams of a Coulomb blockaded quantum dot with orbital degeneracy of the $\mu_{4,\uparrow}$ and $\mu_{5,\uparrow}$ spin-↑ levels. (a)-(c) Co-tunneling process of transferring an electron occupying $\mu_{4,\uparrow}$ to the drain contact and an electron from the source contact to $\mu_{5,\uparrow}$. (d)-(f) Co-tunneling process of transferring an electron occupying $\mu_{5,\uparrow}$ to the drain contact and an electron from the source contact to $\mu_{4,\uparrow}$.

4.4 Correlation induced current suppression

The strongly level-dependent and giant g-factors in InSb nanowire quantum dots enable studies of orbital degeneracies with the same spin at finite magnetic fields. Coherence between levels and correlations with electrons in the leads can give rise to new physical phenomena. In this section, the co-tunneling and resonant current through a InSb nanowire quantum dot at the degeneracy point of the fourth and fifth orbitals with the *same* spin is investigated.

Figure 4.7 shows schematics of two competing co-tunneling transport paths for the degeneracy point of the $\mu_{4,\uparrow}$ and $\mu_{5,\uparrow}$ levels in the Coulomb blockade regime. In Figure 4.7(a) an electron occupies $\mu_{4,\uparrow}$. This electron may tunnel into the drain contact and form a virtual state, (b). An electron may then tunnel from the source contact to the $\mu_{5,\uparrow}$ level, (c). This leaves the quantum dot in a different orbital but with the same spin. Another possibility is that the $\mu_{5,\uparrow}$ level is initially occupied by an electron, (d). This electron may tunnel to the drain contact for a short amount of time, (e). An electron can then tunnel from the source contact into the $\mu_{4,\uparrow}$ level. This leaves the quantum dot in the $\mu_{4,\uparrow}$ orbital, with the same spin.

The InSb nanowire device was fabricated as described in Section 2.2.2 with a contact spacing of 160 nm, see Figure 4.8(a). Figure 4.8(b) shows the conductance through the quantum dot device as a function back-gate voltage, V_g, and applied magnetic field, B, for a source-drain voltage of $V_{sd} = 0.5$ mV. Spin states belonging to the same orbital will split due to the Zeeman effect as discussed in Section 3.4. There is also a slight shift of the peaks upwards in energy due to magnetic confinement (diamagnetic shift). N denotes the total number of electrons in the dot. The spins of the resonant levels are denoted $\uparrow$ for spin-up states and $\downarrow$ for spin-down states assuming negative g-factors with the total projected spin S_Z.

Three different types of degeneracies can be identified, labeled by A, B and C in Figure 4.8(b). The degeneracy points can also be seen in the schematic energy diagram in Figure 4.8(c). Label A indicates the spin degeneracy of the fourth spin-degenerate level, labeled ϵ_4 in Figure 4.8(c). This is the same type of degeneracy discussed in Section 4.2, which gives rise to the spin-1/2 Kondo effect. The associated Kondo resonance can be seen in Figure 4.8(d), which shows the linear conductance as a function of magnetic field along trace A in (b). Label B in Figures 4.8(b) and (c) indicates the region where the fourth and fifth orbitals with different spins become degenerate. The observed conductance peak is due to the Kondo effect for an integer spin [31]. The associated conductance peak can be seen in Figure 4.8(e), which shows the linear conductance as a function of magnetic field along trace B in Figure 4.8(b).

Label C in Figure 4.8(b) and (c) indicates the orbital degeneracy of the $\mu_{4,\uparrow}$ and $\mu_{5,\uparrow}$ states with the same spin. Here, a clear suppression of conductance is observed, as opposed to the conductance enhancement seen at the other degeneracy points. This suppression extends through the Coulomb blockaded region into the sequential tunneling peaks. This is more clearly seen in Figure 4.9(a), which shows a close-up of the area around the degeneracy point C. The traces labeled C1 to C5 in Figure 4.9(a) are shown in Figure 4.9(b) to (f) where the conductance as a function of magnetic field is plotted. Here, the conductance suppression can be clearly seen in both the Coulomb blockade regime and the sequential tunneling regime. The conductance suppression is attributed to destructive interference of the two tunneling paths illustrated in Figure 4.7 [86, 87].

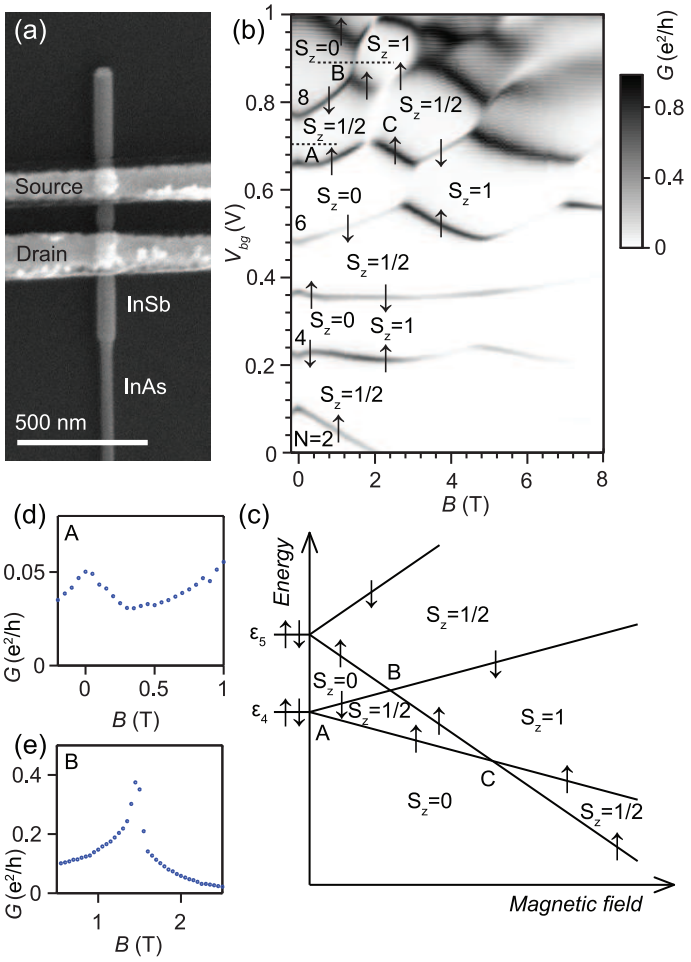

Figure 4.8: (a) Scanning electron microscopy image of a device similar to the device on which the measurements were made. (b) Conductance as a function of back-gate voltage V_{bg} and magnetic field B at $V_{sd} = 0.5$ mV. (c) Schematic energy diagram for the evolution of the fourth and fifth orbitals in a magnetic field, taking into account the Zeeman effect and neglecting Coulomb charging. (d) Trace along the dotted line labeled A in (b), showing conductance as a function of magnetic field. The conductance peak at zero field is associated with the spin-1/2 Kondo effect. (e) Trace along the dotted line labeled B in (b), showing conductance as a function of magnetic field. The conductance peak at finite field is associated with the integer Kondo effect.

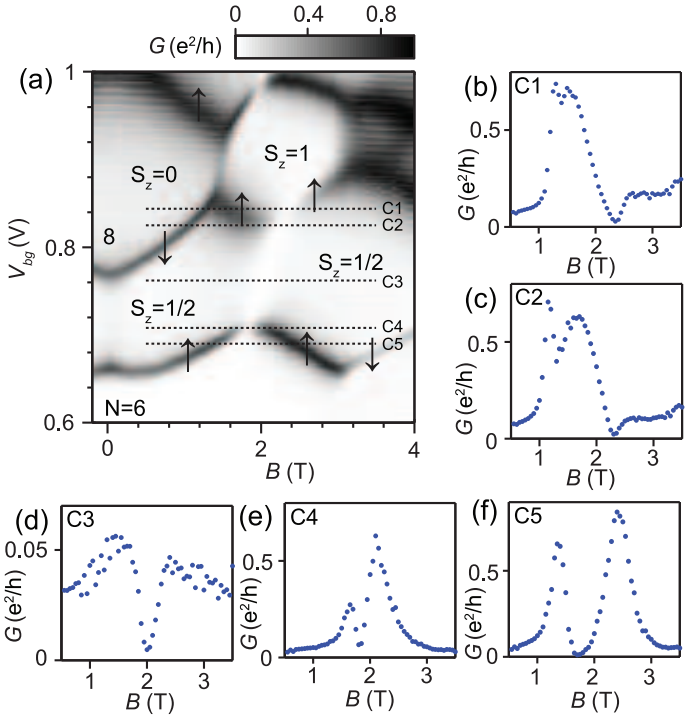

Figure 4.9: (a) Enlarged section of Figure 4.8(b) showing the conductance suppression in detail. (b)-(f) Conductance as a function of magnetic field along traces C1-C5 in (a).

Chapter 5

Double quantum dots

Double quantum dots are discussed in Papers VIII and IX. This chapter describes transport and magneto-transport in double quantum dots. Whereas single quantum dots can be regarded as artificial atoms, the interactions between the two quantum dots in the double quantum dot lead to these systems resembling *artificial molecules*. The large tunability of semiconductor quantum dots make it possible to study and tune interactions between electrons occupying various charge state and spin configurations in the two quantum dots.

Section 5.1 presents a theoretical model for transport through a double quantum dot system based on a classical capacitive model, the so-called constant interaction model. Measurements on double quantum dots fabricated in an InGaAs/InP heterostructure are presented in Section 5.2. Section 5.3 presents a charge state read-out scheme used to determine the exact charge state of the double quantum dot system. Spin-dependent transport in the so-called Pauli spin-blockade regime is discussed in Section 5.4 and singlet-tripet mixing in Section 5.5.

5.1 The constant interaction model

The model presented here is based on the physical concepts developed in reference [42]. Similar to the constant interaction model developed for the single quantum dot discussed in Section 3.1, the double quantum dot system is modeled by capacitors and resistors. The double quantum dot system considered in this model is illustrated in Figure 5.1(a), which shows a schematic equivalent electric circuit with two quantum dots coupled in series by a tunnel barrier with capacitance C_m. Quantum dot 1 is coupled to the source contact through a tunnel barrier with capacitance C_s, and quantum dot 2

is coupled to the drain contact through a tunnel barrier with capacitance C_d. Each dot is also capacitively coupled to a gate electrode with capacitances C_{g1} and C_{g2}. Source-drain and gate voltages are controlled by voltage sources V_{sd}, V_{g1} and V_{g2}, respectively. In the following discussion the linear response regime with negligible cross- and stray capacitances is considered, unless otherwise stated.

First, we will briefly consider the two most extreme cases of coupling between the dots, i.e. two fully coupled dots and two fully decoupled dots. When $C_m = 0$ the dots can be seen as two independent dots, where the electrostatic energy of the two dots reduces to the same form as for a single quantum dot. This regime is illustrated in Figure 5.1(b) which shows a schematic charge stability diagram of the equilibrium electron numbers (N_1, N_2) as a function of gate voltages V_{g1} and V_{g2}, where N_1 and N_2 refer to the number of electrons in dot 1 and dot 2, respectively. Here, the vertical and horizontal lines correspond to changes in the number of electrons in dot 1 and dot 2, respectively. In the case when C_m is the dominant capacitance, i.e. $C_m/C_{1(2)} \rightarrow 1$, the system resembles a single dot with a total charge $N_1 + N_2$. C_1 and C_2 are then the sums of capacitances: $C_1 = C_s + C_{g1} + C_m$ and $C_2 = C_d + C_{g2} + C_m$. This regime is illustrated in Figure 5.1(c) by a charge stability diagram in which both gates affect the single dot levels.

In the linear response regime with negligible cross- and stray capacitances it is possible to calculate the electrostatic energy $U(N_1, N_2)$ for N_1 electrons on dot 1 and N_2 electrons on dot 2, see reference [42] for a full derivation. Knowledge of the electrostatic energy $U(N_1, N_2)$ enables us to determine the electrochemical potentials of the two dots:

$$\begin{aligned}\mu_1(N_1, N_2) &= U(N_1, N_2) - U(N_1 - 1, N_2) \\ &= \left(N_1 - \frac{1}{2}\right) E_{C1} + N_2 E_{Cm} - \frac{1}{|e|}(C_{g1} V_{g1} E_{C1} + C_{g2} V_{g2} E_{Cm})\end{aligned} \tag{5.1}$$

$$\begin{aligned}\mu_2(N_1, N_2) &= U(N_1, N_2) - U(N_1, N_2 - 1) \\ &= \left(N_2 - \frac{1}{2}\right) E_{C2} + N_1 E_{Cm} - \frac{1}{|e|}(C_{g1} V_{g1} E_{Cm} + C_{g2} V_{g2} E_{C2})\end{aligned} \tag{5.2}$$

where E_{C1} and E_{C2} can be interpreted as the uncoupled charging energies of

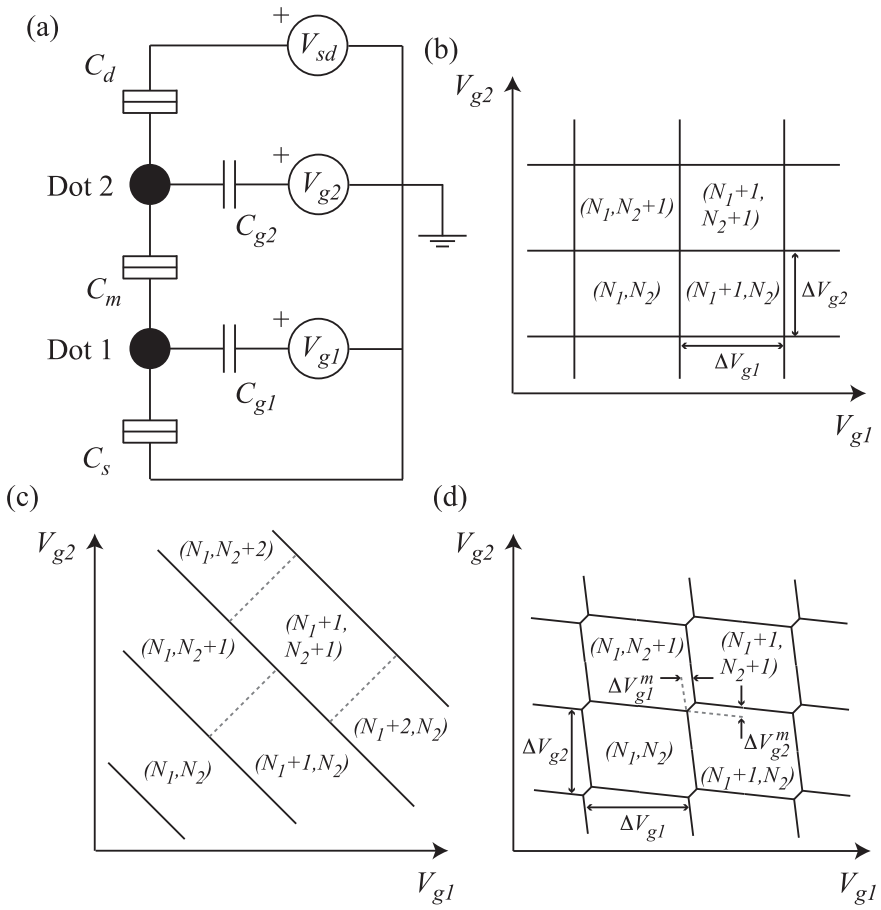

Figure 5.1: (a) Schematic equivalent electric circuit of a double quantum dot in the constant interaction model. Tunnel barriers connect the quantum dots in series to source and drain contacts. The two gates are capacitively coupled to the quantum dots. (b)-(d) Charge stability diagrams showing the charge transition borders for: (b) a decoupled double quantum dot, (c) a fully coupled double quantum dot (single quantum dot) and (d) a weakly coupled double quantum dot.

dots 1 and 2, respectively. E_{Cm} is the electrostatic coupling energy.

$$E_{C1} = \frac{e^2}{C_1}\left(\frac{1}{1 - C_m^2/C_1C_2}\right) \tag{5.3}$$

$$E_{C2} = \frac{e^2}{C_2}\left(\frac{1}{1 - C_m^2/C_1C_2}\right) \tag{5.4}$$

$$E_{Cm} = \frac{e^2}{C_m}\left(\frac{1}{C_1C_2/C_m^2 - 1}\right) \tag{5.5}$$

In the case of weak interdot coupling where quantum mechanical tunnel coupling can be neglected, the charge stability diagram will develop into a hexagon pattern, as seen in Figure 5.1(d). Here, small cross-capacitances between gates and dots have been included, which results in slanted charge transition borders. The size of each hexagon is determined by the gate capacitance according to:

$$\Delta V_{g1} = \frac{|e|}{C_{g1}} \tag{5.6}$$

$$\Delta V_{g2} = \frac{|e|}{C_{g2}} \tag{5.7}$$

The shift in energy at the crossing points of the charge transition borders arises from the capacitive coupling between the dots, and is equal to E_{Cm}. The shift in gate voltage is given by:

$$\Delta V_{g1}^m = \Delta V_{g1}\frac{C_m}{C_2} \tag{5.8}$$

$$\Delta V_{g2}^m = \Delta V_{g2}\frac{C_m}{C_1} \tag{5.9}$$

The corners of the hexagon are called triple points, and mark the points at which three different charge configurations of the double quantum dot are degenerate. In experimental measurements, these configurations would correspond to conductance resonances.

A more detailed schematic charge stability diagram, showing the ground state electrochemical potentials of the region around a pair of triple points is shown in Figure 5.2. Here, the triple point A is identified as the charge degeneracy point, which transfers an electron from the source contact to the drain contact through the cycle: $(N_1, N_2) \rightarrow (N_1 + 1, N_2) \rightarrow (N_1, N_2 + 1) \rightarrow (N_1, N_2)$. For degeneracy point B the cycle is $(N_1 + 1, N_2 + 1) \rightarrow (N_1 + 1, N_2) \rightarrow (N_1, N_2 + 1) \rightarrow (N_1 + 1, N_2 + 1)$. This charge transfer process can be interpreted as resonant tunneling of holes from the drain contact to

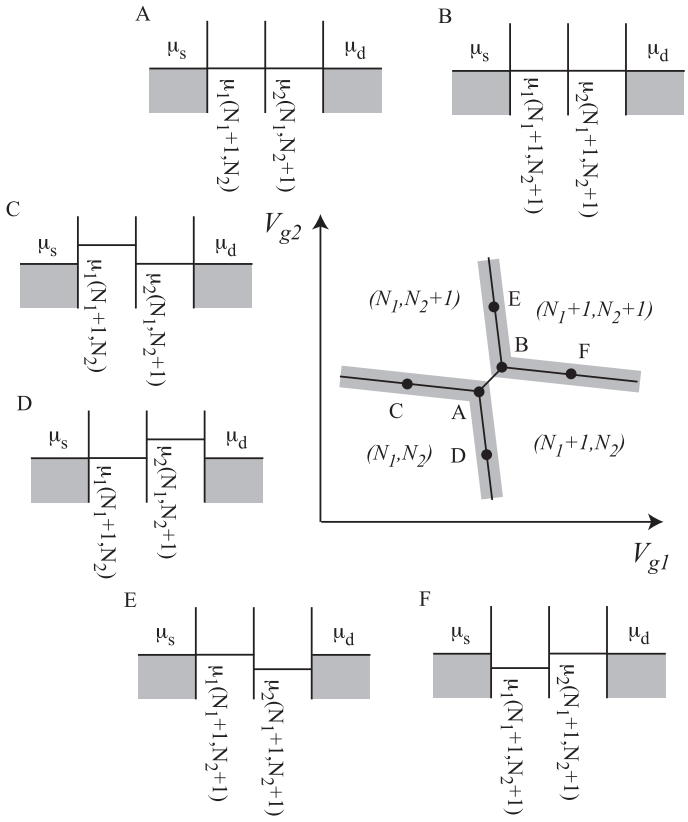

Figure 5.2: Schematic charge stability diagram showing the charge transition borders of a double quantum dot in the weak coupling regime. Four charge states are visible. Points A and B correspond to configurations where the electrochemical potentials of both dots are aligned electrochemical potentials of the source and drain. For points C-F the potential of one dot is aligned with the source or drain potential, whereas the other dot potential is detuned.

the source contact. Points C (F) correspond to configurations where the electrochemical potential of dot 1 is above (below) the aligned source, drain and dot 2 electrochemical potentials, respectively. Points D (E) correspond to configurations where the electrochemical potential of dot 2 is above (below) the aligned source, drain and dot 1 electrochemical potentials, respectively. These four configurations lead to a Coulomb blockaded double quantum dot system.

In order to fully characterize the capacitances of a double quantum dot system it is necessary to determine the gate lever arms $\alpha_{g1} = C_{g1}/C_1$ and $\alpha_{g2} = C_{g2}/C_2$. This is done by performing a charge stability measurement at finite bias. At finite bias the charge transition borders will change into stripes reflecting the larger transport window between the source and drain electrochemical potentials. The width of the stripes is determined by the bias voltage. Assuming a symmetrically applied bias and equal source and drain couplings, the stripes will be centered around the equilibrium charge transition borders as indicated by the gray areas in Figure 5.2.

The triple points will develop into triangular regions of allowed elastic or inelastic squential transport where the stripes overlap. This is illustrated in Figure 5.3, which shows a schematic charge stability diagram with a bias applied such that the electrochemical potential of the source is higher than the electrochemical potential of the drain. The size of the triangular regions in gate voltage δV_{g1} and δV_{g2} are given by the applied source-drain voltage, V_{sd}, and gate lever arms, α_{g1} and α_{g2}, according to:

$$V_{sd} = \alpha_{g1}\delta V_{g1} \tag{5.10}$$

$$V_{sd} = \alpha_{g2}\delta V_{g2} \tag{5.11}$$

Here, the dark gray regions correspond to configurations where transport through the double quantum dot is allowed, whereas the light gray regions correspond to Coulomb blockaded configurations. Point A in Figure 5.3 corresponds to resonant transport through the double quantum dot where both dot levels are in the middle of the source-drain window. Moving along the line with positive slope that intersects point A, will move both dot levels up or down in energy by the same amount relative to the electrochemical potentials of the source and drain. Point B (D) corresponds to a detuned configuration where the right (left) dot level is aligned to the drain (source) potential while the left (right) level is somewhere inside the bias window. At point C the dot levels are detuned such that $\mu_1 > \mu_2$ and are inside the bias window. Point E corresponds to the configuration where the left dot level is aligned with the source potential and the right dot level is aligned with the drain potential. Thus, points B-E correspond to regions of allowed

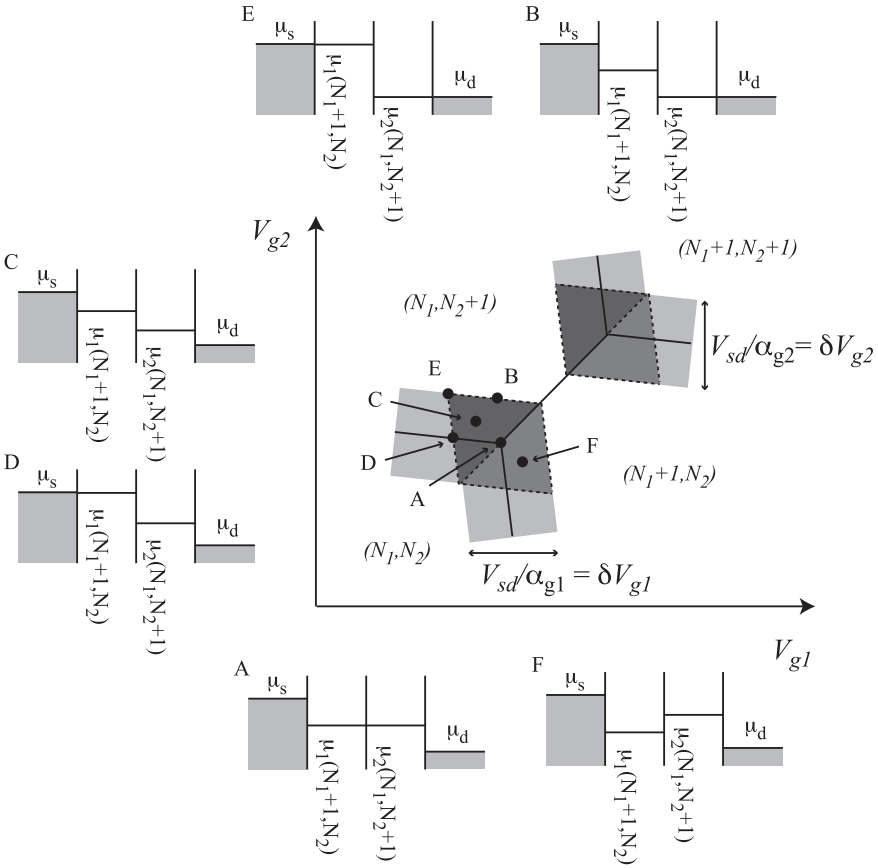

Figure 5.3: Schematic charge stability diagram showing a triple point pair at finite bias. Point A corresponds to alignment of the potential of the two dots centered between the source and drain electrochemical potentials. Points B-E correspond to configurations where both dot potentials are in between the source and drain levels and $\mu_1 > \mu_2$. Point F corresponds to a configuration where both dot levels are between the source and drain window and $\mu_1 < \mu_2$.

inelastic transport through the double quantum dot. The lower lighter gray triangular region outlined by dashed lines correspond to a Coulomb blockaded configuration where $\mu_1 < \mu_2$, see point F.

5.2 Transport in double quantum dots

In this section low-temperature transport measurements on a double quantum dot formed in the device shown in Figure 3.7(a) are presented. The double quantum dot is formed by inducing tunnel barriers in the quantum wire using gates lg1, lg3 and lg5 to form two quantum dots, one dot below lg2 and one dot below lg4. The individual voltages applied to lg1 and lg5 determine the couplings to the source and drain contacts, whereas the voltage applied to lg3 determines the interdot coupling. Double quantum dot measurements were carried out by first fine-tuning V_{lg1}, V_{lg3} and V_{lg5} to the coupling regime of interest. The double quantum dot stability diagram was then obtained by keeping V_{lg1}, V_{lg3} and V_{lg5} fixed and sweeping the plunger gates V_{lg2} and V_{lg4} to tune the number of electrons in the two dots.

Figure 5.4(a) shows the conductance through the double quantum dot as a function of V_{lg2} and V_{lg4} in the linear response regime on a logarithmic color scale with an intermediate to strong interdot coupling using the settings $V_{sd} = 25$ μV, $V_{lg1} = -380$ mV, $V_{lg3} = -180$ mV and $V_{lg5} = -420$ mV. The measurements were performed at a temperature of around 100 mK. The hexagonal patterns outlining the charge transition borders can be clearly seen. The finite conductance lines connecting the triple points are caused by co-tunneling through the detuned dot level. In this configuration the dots contain $\sim$10 electrons each.

Figure 5.4(b) shows the double dot stability diagram at the $(4,4) \rightarrow (3,5)$ charge transition measured at finite bias. Here, the charge states were determined using a charge sensor (see Section 5.3). The static voltages used in the measurement were $V_{sd} = 1$ mV, $V_{lg1} = -390$ mV, $V_{lg3} = -250$ mV and $V_{lg5} = -440$ mV. The increase in negative voltages on the barrier gates resulted in weaker tunnel coupling to the source and drain contacts and between the dots. As a consequence, the co-tunneling lines connecting the triple points are suppressed. The triple points have developed into triangles of finite current. Here, the bias is so large that the two triple points overlap. The dot levels are aligned at the base of the triangles, which results in a large current peak. Inside the triangle, transport occurs via inelastic events which reduces the current through the double dot compared to the resonant transport configuration. From the size of the triangles and Equations 5.10 and 5.11 the plunger gate lever arms were found to be $\alpha_{lg2} = 0.29$ and

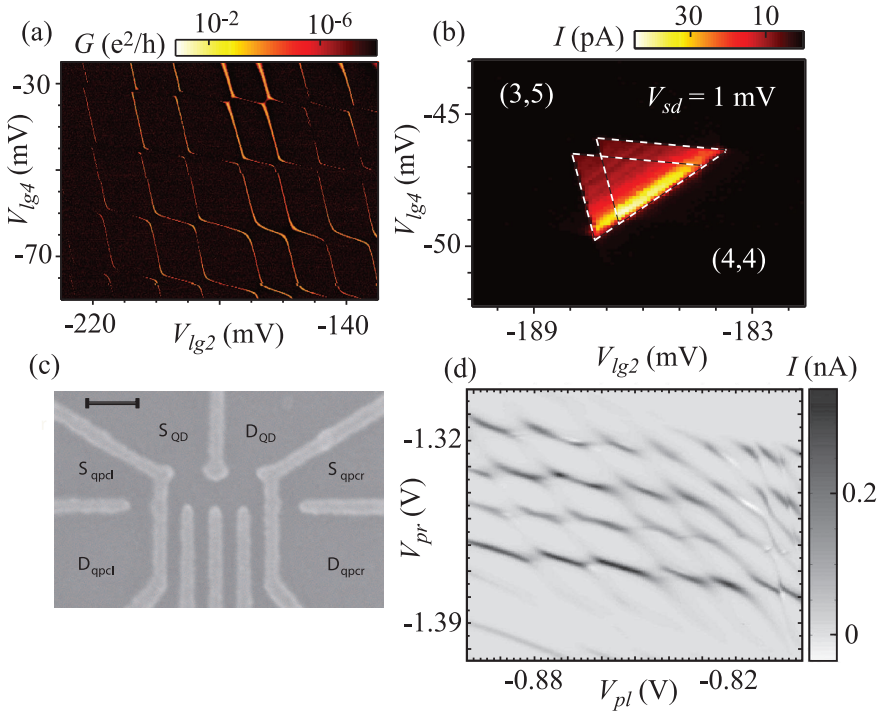

Figure 5.4: (a) Double quantum dot charge stability diagram showing linear conductance on a logarithmic color scale as a function of V_{lg2} and V_{lg4}. (b) Stability diagram showing the current through the double dot for a finite bias. The triple points have grown into triangles of finite current through inelastic sequential transport. Co-tunneling is suppressed outside the triple points due to weaker tunnel coupling. (c) Scanning electron microscope image of a double quantum dot defined in an InGaAs 2DEG by top gate electrodes. The scale bar is 200 nm. (d) Charge stability diagram showing current through the double quantum dot seen in (c) on a gray scale, as a function of the right and left plunger gate voltages V_{pr} and V_{pl}.

$\alpha_{lg4} = 0.32$.

Measurements were also perfomed on a top-gate-defined double quantum dot, see figure 5.4(c). This demonstrates the possibility of defining the double quantum dot using only top gate electrodes, thus eliminating the need for a fine etch process thereby simplifying the fabrication procedure. The double quantum dot was formed by applying negative voltages to six of the top gates. The lithographic diameters of the dots are approximately 150 nm. Two quantum point contacts were also defined in close proximity to the dots to act as charge sensors (see Section 5.3). Measurements were performed in a ^{3}He cryostat at a temperature of 300 mK, and showed hexagonal patterns of current through the double quantum dot, see Figure 5.4(d). However, thermal smearing of the Fermi level due to the relatively high cryostat temperature resulted in less pronounced hexagonal patterns. This device was not successfully tuned to the few-electron regime. However, charge sensing of the double quantum dot charge state was possible by monitoring the conductances of the two quantum point contacts.

5.3 Charge sensing

One of the challenges in transport measurements of the current through a single or double quantum dot is determining the exact charge state that is being measured. One way to identify the charge state is to try to completely deplete the dot or dots of electrons, while studying transport. This can be achieved by finding the region of conductance through the dot or dots where the diamond (single dot) or hexagon (double dot) structure ends, as this corresponds to a completely empty dot or dots. However, the structure could disappear due to pinched off tunnel coupling since the plunger gate used to deplete the dot also effects the coupling. This makes the method unreliable in some devices. A more reliable way of determining the charge state of a quantum dot is by using a quantum point contact (QPC) as a charge read-out sensor in close proximity to the dot such that the two systems are capacitively coupled [88]. QPC charge sensors have been widely used to characterize quantum dot systems and to study real-time tunneling of electrons through both single and double quantum dots [47, 89, 90, 91].

Figure 5.5(a) shows a schematic equivalent circuit of a double quantum dot capacitively coupled via $C_{1,s}$ and $C_{2,s}$ to a quantum point contact in a separate sensor circuit. In a quantum point contact the value of the conductance is quantized according to $G_{QPC} = 2Me^2/h$, where M is the number of modes available for transport [92]. This effect is called conductance quantization, and is caused by the lateral confinement of electrons. Spin degeneracy

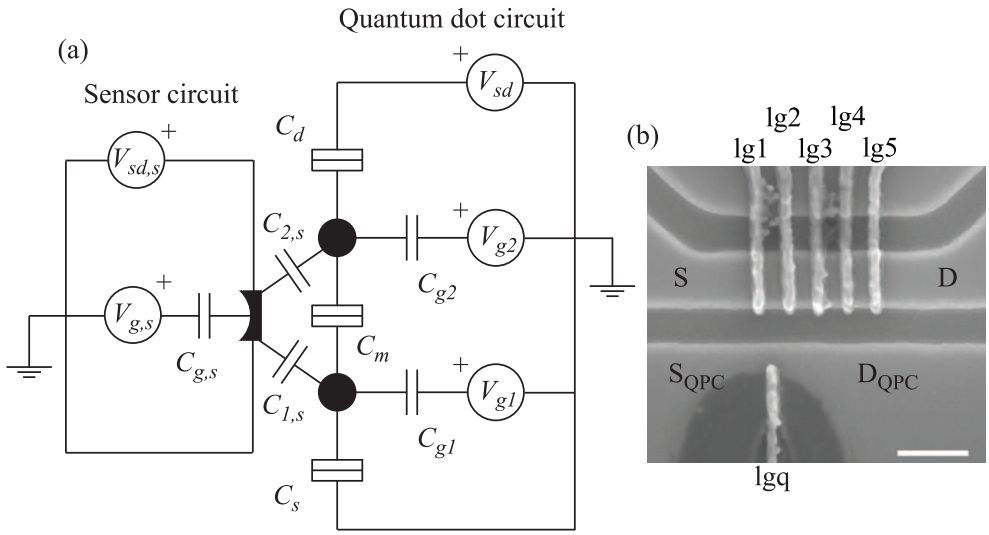

Figure 5.5: (a) Schematic equivalent circuit of a double quantum dot capacitively coupled to a quantum point contact charge sensor. (b) Scanning electron microscope image of a double quantum dot with an integrated quantum point contact charge sensor defined in an InGaAs/InP heterostructure. A local finger gate was used to tune the conductance through the quantum point contact. The scale bar is 200 nm.

is assumed in the equation. The number of open modes in a quantum point contact device is controlled by the lateral confinement, which is tuned by the quantum point contact gate voltage $V_{g,s}$. In the transition region between two conductance modes, or plateaus, the transconductance $dG_{QPC}/dV_{g,s}$ will be high, which will make the quantum point contact conductance very sensitive to its electrostatic environment. This makes it possible to detect changes in charge in the vicinity of the quantum point contact, such as changes in the charge state of a near by quantum dot, by looking for sudden jumps in the quantum point contact conductance, G_{QPC}. Since the quantum point contact only detects changes in the charge state of a nearby quantum dot, and not the transport through the dot, it is possible to detect changes in the charge state despite the fact that the current through the quantum dot might be too small to be measured due to weak tunnel coupling. This makes it possible to accurately determine the absolute charge state of a quantum dot or double quantum dot.

Figure 5.5(b) shows a scanning microscope image of an integrated device consisting of a double quantum dot and a quantum point contact. The quantum point contact connected to source and drain reservoirs and formed by an etched defined constriction with a width of 250 nm and a local finger gate lgq. The gate is used to tune the quantum point contact conductance to the regime where it is sensitive to changes in the charge state of the double quantum dot.

Figure 5.6(a) shows the quantum point contact linear conductance, G_{QPC}, as a function of V_{lgq} for a source-drain bias $V_{sd,QPC}$ of 1 mV. The quantum point contact conductance is close to the first plateau at $2e^2/h$, even without an applied voltage possibly due to surface depletion at the edges of the constriction. As V_{lgq} becomes more negative the conducting mode is pinched off. The optimal working point is the region on the curve where the slope is large, i.e. where the transconductance dI_{QPC}/dV_{lgq} is large, around $G_{QPC} = e^2/h$. However, this particular quantum point contact exhibited considerable instabilities in conductance, possibly due to charge traps in the HfO_2 dielectric, which made it necessary to operate it at conductances much smaller than e^2/h.

In Figure 5.6(b), the charge read-out sensor signal is plotted as the transconductance dI_{QPC}/dV_{lg2} as a function of V_{lg2} and V_{lg4} at $V_{sd,QPC} = 1$ mV, measured simultaneously with the data presented in Figure 5.4(a). Here, the hexagonal patterns in the sensor signal agree well with the hexagons in the double dot transport seen in Figure 5.4(a). The sensor signal can be interpreted as follows. As the plunger gate voltages of the double quantum dots are increased, electrons are added to the two quantum dots giving rise to co-tunneling and sequential tunneling peaks in the transport through the

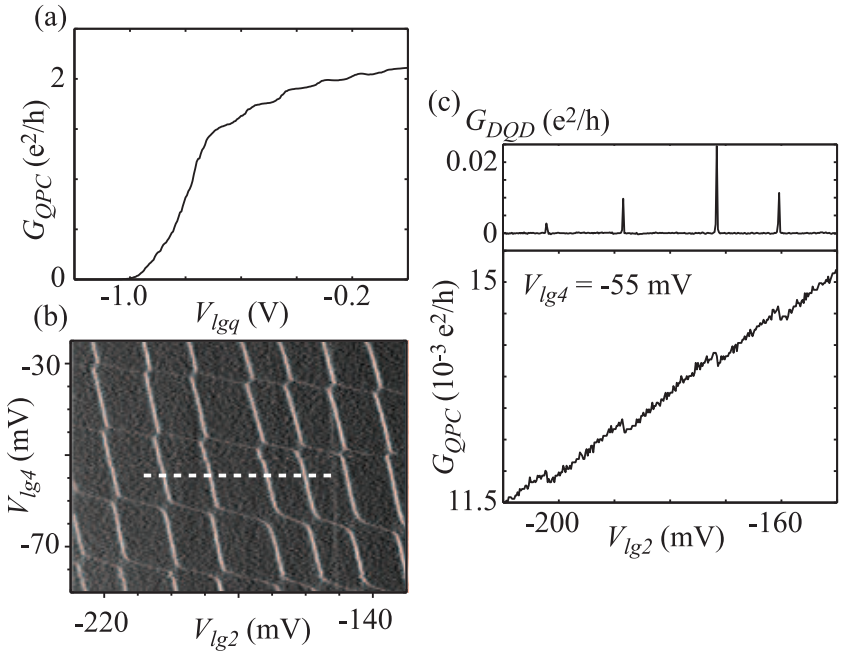

Figure 5.6: (a) Quantum point contact conductance G_{QPC} as a function of V_{lgq} at $V_{sd,QPC} = 1$ mV. The first quantized conductance step corresponding to $2e^2/h$ is seen. (b) Charge stability diagram showing the transconductance dI_{QPC}/dV_{lg2} of the charge read-out QPC as a function of V_{lg2} and V_{lg4} measured simultaneously with figure 5.4(a). (c) Linear conductance through the QPC (G_{QPC}) and double quantum dot G_{DQD} as a function of V_{lg2} at $V_{lg4} = -55$ mV [dashed line in (b)]. There are small kinks in the QPC conductance at the charge state transitions. Corresponding co-tunneling peaks can be seen in the double quantum dot conductance at the same voltages.

double quantum dot at the charge state transitions. At the same time, the charge transitions of the double quantum dot will cause jumps in the quantum point contact conductance due to the charges added to the dots. The added dot charges will effectively *gate* the quantum point contact thereby reducing the conductance. Thus, the steps in G_{QPC} at the charge state transitions will give rise to dips in the transconductance dI_{QPC}/dV_{lg2}, as seen in Figure 5.6(b).

The steps in G_{QPC} are clearly seen in Figure 5.6(c), which shows the conductance of the quantum point contact (G_{QPC}) and double quantum dot (G_{DQD}) as a function of V_{lg2} at $V_{lg4} = -55$ mV [dashed line in (b)]. The correlation between transport through the double quantum dot and steps in quantum point contact conductance at the charge state transitions is clearly visible.

It can be seen in Figure 5.6(b) that the signal from the left quantum dot (vertical dips in transconductance) is stronger than the right dot (horizontal dips in transconductance). This is because the capacitive coupling between the left dot and quantum point contact is greater than that between the right dot and quantum point contact. The difference in capacitive coupling arises from the fact that the left dot is closer to the quantum point contact than the right dot. The background slope of G_{QPC} seen in Figure 5.6(c) is the result of the cross-coupling of the quantum point contact with the plunger gates. In particular, it can also be seen in Figure 5.6(b) that the sensor signal is constant over the voltage ranges measured. Thus, the sensor signal does not depend on the actual tunnel coupling of the double quantum dot, which obviously changes over the voltage ranges measured, as can be seen in Figure 5.4(a).

The only requirement on the tunnel coupling of the quantum dots for charge sensing to work is that the measurement time of the quantum point contact current is longer than the tunneling time of electrons. If the tunneling time is longer than the measurement time the equilibrium charge transition might not be correctly determined in the measurement.

The double quantum dot was tuned to the final charge state, i.e. the (0,0) charge state and the information obtained was used in subsequent measurements to determine the absolute charge state. In the measurements described below, the static gate voltages were $V_{lg1} = -370$ mV, $V_{lg3} = -200$ mV, and $V_{lg5} = -420$ mV. Figure 5.7(a) shows the conductance through the quantum point contact as a function of V_{lg2} and V_{lg4} in the vicinity of the final charge state (0,0) of the double quantum dot. In order to more clearly show the conductance signal of the sensor the electrostatic dependence of V_{lg2} and V_{lg4} have been removed by subtracting linear functions of the gates. After the (0,0) state no further jumps are seen in the sensor signal when decreasing the

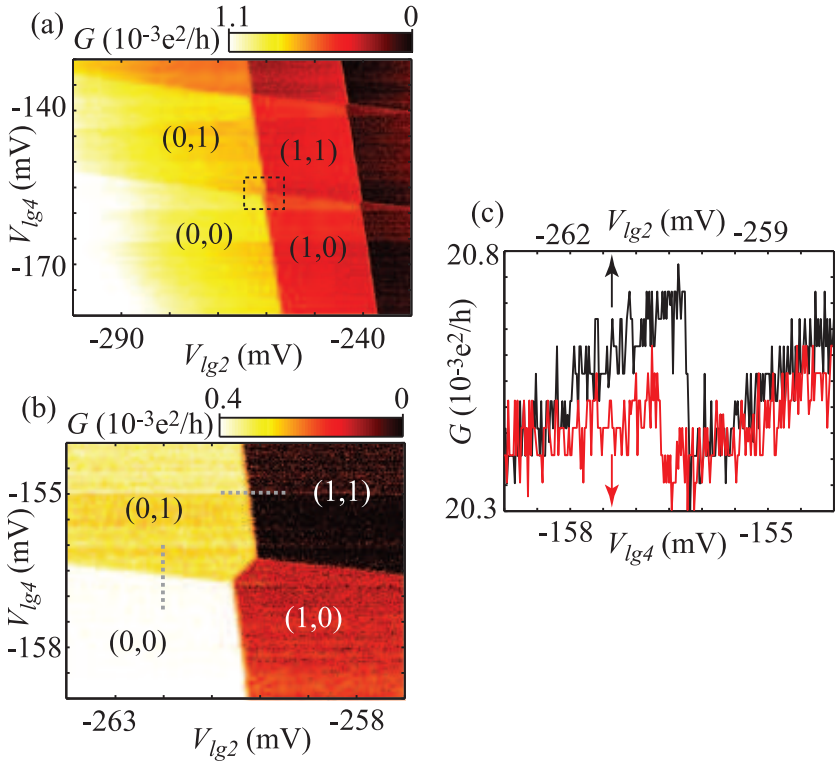

Figure 5.7: (a) Conductance of the charge read-out QPC as a function of V_{lg2} and V_{lg4} in the few-electron regime. A background conductance plane has been subtracted. The levels of the conductance seen in the figure correspond to different charge state configurations. Four charge states are indicated in this figure as (N_1, N_2), where N_1 and N_2 are the exact numbers of electrons in the left and right dots, respectively. (b) Close-up of the region enclosed by the dashed lines in (a). (c) Traces along the dotted lines in (b) showing the measured QPC conductance as a function of gate voltage.

voltages on the plunger gates. This suggests that the two dots are completely depleted of electrons and that the (0,0) charge state has been identified.

Figure 5.7(b) shows a close-up of the area indicated by the dashed lines in Figure 5.7(a). Four constant values of the conductance corresponding to the four different charge state configurations, i.e. $(0,0)$, $(0,1)$, $(1,0)$ and $(1,1)$ are visible. From the traces along the dotted lines in Figure 5.7(b) seen in Figure 5.7(c) the magnitude of the steps in quantum point contact conductance corresponding to a unit change in charge on the left quantum dot were estimated to be about $\Delta G_{left} = 0.3 \times 10^{-3}$ e^2/h and about $\Delta G_{right} = 0.1 \times 10^{-3}$ e^2/h for a unit change in the number of electrons on the right dot. The steps in conductance correspond to measured steps in current of around 5 to 10 pA for the applied source-drain bias $V_{sd,QPC} = 1$ mV. For the double quantum dot configuration shown in Figure 5.7(a) the current through the double quantum dot is below the limit of the experimental setup due to pinch-off of the tunnel couplings.

5.4 Pauli spin blockade

In certain configurations, the well defined spin states in few-electron double quantum dots will lead to a current rectification effect. This effect, called Pauli spin blockade, stems from the Pauli exclusion principle, which states that two electrons with the same spin cannot occupy the same orbital. Pauli spin blockade can be directly observed in the tunneling current of a two-electron diatomic molecule system formed in a weakly coupled double quantum dot [93].

The physical principle of the Pauli spin blockade is depicted schematically in Figure 5.8(a) and (b) which shows schematic energy diagrams of a double quantum dot system with one spin-↑ electron permanently occupying the right quantum dot. Here, the double dot states are labeled $[M_1, M_2]$ where M_1 and M_2 are the number of electrons on the left and right dot, respectively, not including paired electrons permanently occupying either dot. Initially, the double quantum dot system will occupy the $[0,1]$ state. An electron may tunnel from the source contact into the left dot to form the two-electron $[1,1]$ state. In the limit of weak interdot coupling the two dots can be considered almost independent and the $[1,1]s$ singlet state (anti-parallel spin) and the $[1,1]t$ triplet state (parallel spin) are practically degenerate. The electron entering from the source contact may therefore populate either the $[1,1]s$ state or the $[1,1]t$ state. If the $[1,1]s$ state is populated, as in Figure 5.8(a), the spin-↓ electron on the left dot may tunnel into the right dot to form a $[0,2]s$ state. The electron may then leave the double quantum dot through

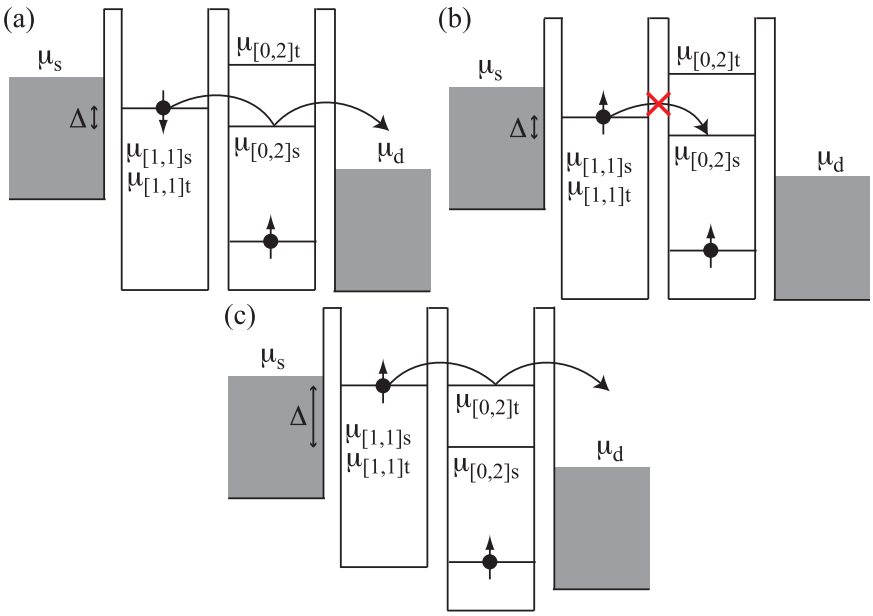

Figure 5.8: (a) and (b) Schematic energy diagrams showing the principle of Pauli spin blockade for a double quantum dot system with one permanent electron on the right dot and one electron entering from the source contact. The $[1,1]s \rightarrow [0,2]s$ transition is allowed (a), whereas the $[1,1]t \rightarrow [0,2]s$ transition is blocked (b) due to the Pauli exclusion principle. (c) Spin blockade may be lifted if the $[0,2]t$ state comes into resonance with the $[1,1]t$ and $[1,1]s$ states.

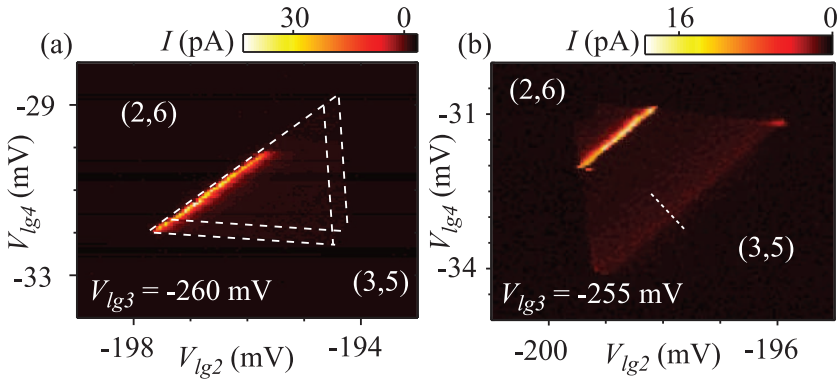

Figure 5.9: (a) Charge stability diagram showing current through a double quantum dot at the $(2,6) \rightarrow (3,5)$ charge transition with $V_{sd} = 1$ mV. The triple points are outlined for clarity. (b) Charge stability diagram showing current through the double quantum dot at the $(3,5) \rightarrow (2,6)$ charge transition with reversed bias $V_{sd} = -1$ mV. Current is suppressed along the baseline. The high-current line corresponds to the onset of transport through an excited triplet state of the right dot.

the drain contact. Current can therefore flow through the device. However, if the $[1,1]t$ state is populated, as in Figure 5.8(b), the spin-$\uparrow$ electron occupying the left dot can not tunnel into the right dot via the $[0,2]s$ state due to the Pauli exclusion principle nor can it tunnel into the $[0,2]t$ state as this state has higher energy. If the $[1,1]t$ state is below the electrochemical potential of the left lead the spin-$\uparrow$ electron will be trapped on the left dot due to relaxation of the hole left behind on the left lead. As a consequence, as soon as a spin-$\uparrow$ electron populates the left dot, current through the double quantum dot will be blocked. The only way for current to flow again in this configuration is by a spin-flip of the electron occupying the left dot. For the reverse bias configuration the transport cycle is $[0,1] \rightarrow [0,2]s \rightarrow [1,1]s \rightarrow [0,1]$, and there is no spin blockade. Thus, a double quantum dot in this configuration acts as a current rectifier.

One way to lift the spin blockade is to detune the energy levels of the two dots such that the $[0,2]t$ state comes into resonance with the $[1,1]s$ and $[1,1]t$ states, as in Figure 5.8(c). In this configuration, spin-$\uparrow$ electrons may tunnel from the source contact to the drain contact via $[1,1]t \rightarrow [0,2]t$, and spin-$\downarrow$ electrons may tunnel via $[1,1]s \rightarrow [0,2]s$. The onset of transport through the triplet state is typically expressed in terms of the detuning parameter Δ, defined as: $\Delta = \mu_{[1,1]t} - \mu_{[0,2]s}$, see figures 5.8(a)-(c).

Figure 5.9(a) shows a stability diagram at the $(2,6) \rightarrow (3,5)$ charge

transition for the double quantum dot system shown in Figure 5.5(b) measured with a finite source-drain bias $V_{sd} = 1$ mV. The static gate voltages used in this and the following measurements were $V_{lg1} = -390$ mV and $V_{lg5} = -440$ mV, with the voltage of V_{lg3} indicated in the figures. Again, the charge read-out sensor was used to determine the exact charge state transition. High current is visible along the baseline of the triple points, as expected. When the bias is reversed such that $V_{sd} = -1$ mV the triple point will be mirrored with respect to the baseline, as in Figure 5.9(b). Here, it can be seen that the current is strongly suppressed along the baseline. A new high-current line parallel to the baseline is seen at a constant detuning of the energy levels of the two dots.

The observed current rectification can be be explained by the Pauli spin blockade. Only unpaired spins on the two dots will be considered in the following discussion. The $(2, 5)$ charge state will be denoted the $[0, 1]$ state since the two electrons permanently occupying the left dot and the four electrons permanently occupying the right dot form pairs. Thus, the $(3, 5)$ charge state will be referred to as the $[1, 1]$ state and the $(2, 6)$ charge state as the $[0, 2]$ state. Inside the triangular region, from the baseline to the high-current line, the energy level configuration resembles those in Figures 5.8(a) and (b), where transport is only allowed for the $[1, 1]s \rightarrow [0, 2]s$ transition. Current is therefore suppressed due to spin blockade.

At the lower edge of the baseline the current through the double quantum dot increases slightly. Here the $[1, 1]s$ and $[1, 1]t$ states are aligned with the electrochemical potential of the source. A spin-$\uparrow$ electron populating the $[1, 1]t$ state may then tunnel out of the left dot into the source contact and can be replaced by a spin-$\downarrow$ electron, thus leading to an increase in the current through the system. The equivalent hole cycle takes place at the upper edge of the baseline, leading to an increase in current. The high current peak that runs parallel to the baseline indicates the onset of transport through the $[1, 1]t \rightarrow [0, 2]t$ transition allowing the transport of electrons with both spins, which leads to lifting of the spin blockade.

5.5 Singlet-triplet mixing

A leakage current through the Pauli spin blockade can be attributed to mixing of the singlet and triplet states. In double quantum dots the spin-orbit and hyperfine interactions are the two most important interactions between spins on the dots and the environment that contribute to mixing of the singlet and triplet states, and therefore leakage current, in the Pauli spin blockade regime [5].

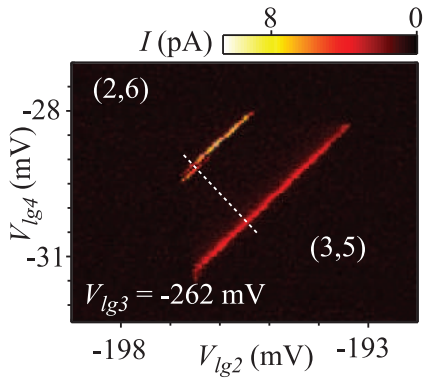

Figure 5.10: Charge stability diagrams showing current through the double quantum dot at the $(3,5) \rightarrow (2,6)$ charge transition with decreased interdot coupling compared to Figure 5.9(b). A leakage current through the Pauli spin blockade is visible along the baseline of the triangle.

Figure 5.10 shows a charge stability diagram of the same charge transition shown in Figure 5.9(b) but with $V_{lg3} = -262$ mV which leads to a decrease in interdot coupling. A pronounced peak in the current through the system now runs along the baseline in the Pauli spin blockade regime. The origin of this current peak is the mixing of the $[1,1]s$ and $[1,1]t$ states. The influence of the hyperfine interaction between the electron spin and the nuclear spins on the leakage current in the Pauli spin blockade regime will be discussed below. The influence of the spin-orbit interaction on the leakage current will also be discussed briefly.

In InGaAs quantum dots each electron spin is coupled to many surrounding non-zero nuclear spins via the hyperfine interaction. This is a consequence of the spacial extension of the electron wave function over the quantum dot. The random unpolarized and uncorrelated nuclear spins will give rise to an inhomogeneous effective nuclear magnetic field pointing in a random direction with a strength B_n, the so-called Overhauser field. The nuclear field will couple the singlet and triplet states in the double quantum dot structure when $E_n > \Delta E_{st}$, where $E_n = |g^*|\mu_B B_n$ is the Zeeman splitting energy caused by the nuclear magnetic field, and $\Delta E_{st} = |E_{[1,1]s} - E_{[1,1]t}|$ is the singlet-triplet splitting energy of the $[1,1]$ states. In a Pauli spin-blockaded double quantum dot the mixing of the singlet of triplet states due to hyperfine interaction will lead to triplet-to-singlet relaxation and thus induce a leakage current.

To qualitatively explain the leakage current through the spin blockade seen in the present measurements it is necessary to take into account the

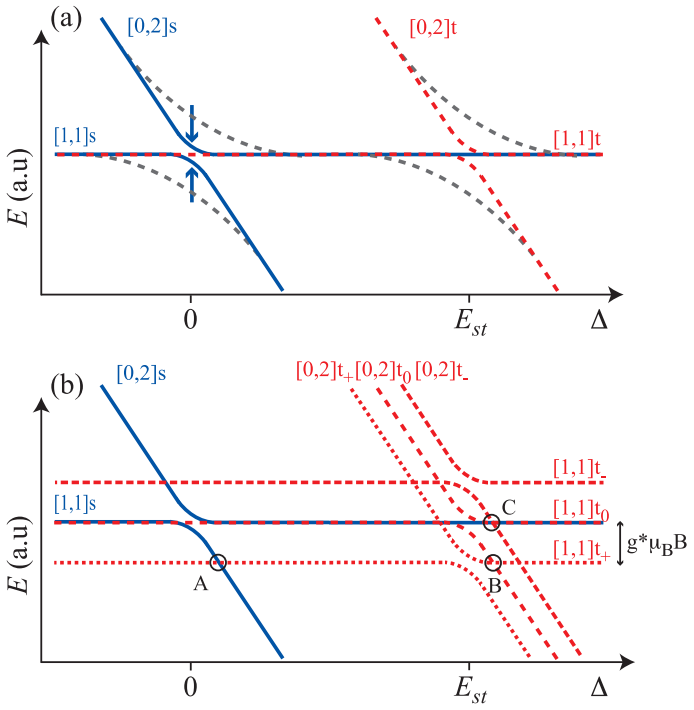

Figure 5.11: (a) Schematic of the energy evolution of the $[1,1]s$, $[1,1]t$, $[0,2]s$ and $[0,2]t$ states as a function of detuning, Δ. The hybridization of the $[1,1]s$ and $[0,2]s$ states and the $[1,1]t$ and $[0,2]t$ states due to the finite interdot coupling leads to avoided level crossings at $\Delta = 0$ and $\Delta = E_{st}$. (b) With a finite external magnetic field the $[1,1]t$ and $[0,2]t$ states split into three levels due to the Zeeman effect. Alternative transport paths at various degeneracy points are possible through spin-flip processes, for example, at points A, B and C.

competing energy scales of E_n, ΔE_{st} and $E_{ext} = |g^*|\mu_B B$, where B is the external magnetic field. First, consider the case in which the external magnetic field is zero. Figure 5.11(a) shows a schematic energy diagram of the evolution of the $[1,1]$ and $[0,2]$ singlet and triplet states as a function of the detuning parameter, Δ. The detuning is defined such that the $[1,1]s$ and $[1,1]t$ states have constant energy as a function of Δ. Near $\Delta = 0$ the $[1,1]s$ and $[0,2]s$ states will hybridize due to the finite interdot coupling and form an avoided level crossing. The anticrossing energy gap depends on the interdot coupling. A smaller interdot coupling will give rise to a smaller energy gap, as illustrated by the solid blue lines and arrows in Figure 5.11(a), whereas a larger interdot coupling will give rise to a larger energy gap, as shown by the dashed gray lines in Figure 5.11(a). The energy splitting, ΔE_{st}, between the $[1,1]t$ triplet state and the hybrid $[1,1]s$ and $[0,2]s$ singlet states will therefore depend on both the interdot coupling and the detuning. Efficient mixing of the $[1,1]s$ and $[1,1]t$ states is possible only when $E_n > \Delta E_{st}$. This means that for a smaller interdot coupling the hyperfine mixing in the spin blockade regime is efficient for small detuning as well as positive detuning, while for a larger interdot coupling mixing is suppressed around $\Delta = 0$, as is evident in Figure 5.11(a). Similar mixing also takes place for $\Delta = E_{st}$, where the triplet states will hybridize.

Figure 5.11(b) show the schematic energy diagram of the evolution of the $[1,1]$ and $[0,2]$ singlet and triplet states in the presence of an external magnetic field B. Here, the triplet states will split into three levels (t_0, t_+ and t_-), where the splitting is given by the Zeeman energy, $E_{ext} = |g^*|\mu_B B$. The split-off triplet states $t_\pm$ results in recovery of the spin blockade for these states in the weak interdot coupling case. This will result in a peak in leakage current around $B = 0$. In the strong interdot coupling case the split-off triplet states may move closer to the separated hybrid singlet states, and can therefore enhance the mixing via the nuclear field around $\Delta = 0$. Hyperfine-induced mixing may also lead to enhanced transport through the system at other degeneracy points such as A, B and C in Figure 5.11(b). At these degeneracy points higher order spin-flip processes are needed to allow electrons to travel through the double quantum dot.

To quantitatively investigate the hyperfine mixing in the few-electron InGaAs double quantum dot the current through the system was first studied as a function of detuning, Δ, and external field, B, in the weak coupling regime, see Figure 5.12(a). The gate voltages have been converted to detuning energy, Δ. Detuning is defined as zero along the baseline of the triple points and positive inside the triple points. The high-current peak around zero detuning and zero field was identified as the resonant leakage current through the $[1,1]s$ and $[0,2]t$ states. For larger external fields, mixing between the singlet

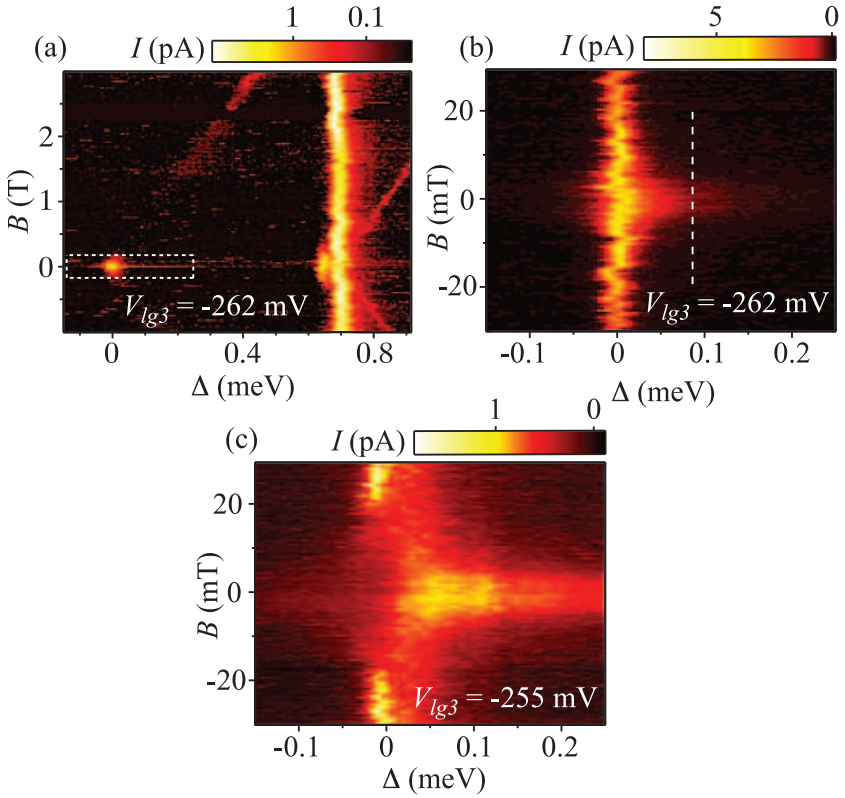

Figure 5.12: (a) Current through the double quantum dot as a function of external applied magnetic field and detuning cut along the dashed white line in Figure 5.10. (b) Close-up of the area within the white dashed line in (a). (c) The same as (b), but with greater interdot tunnel coupling.

state and the two split-off triplet states is suppressed. However, higher order hyperfine mediated spin-flip events at the degeneracy point of the $[1,1]t_+$ and $[0,2]s$ states will give rise to a finite but small leakage current through the spin blockade, moving towards more positive detuning with increasing magnetic field. This leakage current corresponds to the degeneracy point A in figure 5.11(b).

The strong current peak at $\Delta = 0.7$ meV correspond to resonant tunneling through the $[1,1]t$ and $[0,2]t$ states. The detuning of this strong peak is constant with applied magnetic field since the two triplet states Zeeman split by an equal amount. The two smaller peaks that split off from the strong $\Delta = 0.7$ meV peak correspond to resonant tunneling through the $[1,1]t_+ \rightarrow [0,2]t_0$ and $[1,1]t_0 \rightarrow [0,2]t_-$ transitions (positive slope) [see also points B and C in Figure 5.11(b)], and to the $[1,1]t_0 \rightarrow [0,2]t_+$ and $[1,1]t_- \rightarrow [0,2]t_0$ transitions (negative slope). These transitions also require higher order spin-flip processes leading to smaller current for these peaks than for the strong $\Delta = 0.7$ meV peak. The effective g-factor, g^*, can be determined by fitting the position of the split-off current peaks as a function of magnetic field. From such a fit a value of $|g^*| = 2.3$ was determined.

Figure 5.12(b) and (c) shows close-ups of the region outlined in Figure 5.12(a) for small and large interdot coupling respectively. In the case of weak interdot coupling, the leakage current at small external magnetic fields is present in both the zero and the positive finite detuning transport regions, whereas for strong interdot coupling the leakage current is suppressed in the region around $\Delta = 0$. This behavior is consistent with the schematic in Figure 5.11(a).

The Overhauser field can be extracted from the leakage current at finite detuning in the limit of weak interdot coupling. The experimental data were fitted using a relation from the quantitative description developed in reference [94]:

$$< I > /e = \Gamma_{in} S(\sqrt{3}B/B_n), \tag{5.12}$$

where Γ_{in} is the tunneling rate and

$$\begin{aligned} S(x) = {} & 4/x^2 - 6/x^4 + \sqrt{2\pi}\mathrm{erfi}(x/\sqrt{2})(6/x^5 - 2/x^3) \\ & \times \exp(-x^2/2) - 3\pi\mathrm{erfi}^2(x/\sqrt{2})\exp(-x^2)/x^6. \end{aligned} \tag{5.13}$$

$< I >$ is the average leakage current. Figure 5.13(a) shows the leakage current as a function of magnetic field for a constant detuning of $\Delta = 80$ μeV for three different interdot couplings. The solid lines represent the theoretical fits of the experimental data. From the fits a value of $B_n = 2.7$ mT was

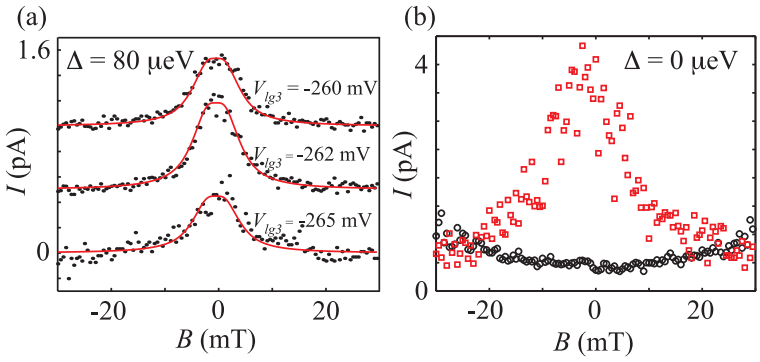

Figure 5.13: (a) Leakage current as a function of the applied external magnetic field at detuning $\Delta = 80$ μeV [i.e., along the white dashed line in Figure 5.12(b)] for three different weak interdot couplings. The solid lines are theoretical fits to the experimental data. Offsets have been added to the two upper plots for clarity. (b) Leakage current as a function of the applied external magnetic field at detuning $\Delta = 0$ μeV in a weak interdot coupling case using $V_{lg3} = -265$ mV (squares) and a stronger interdot coupling case using $V_{lg3} = -255$ mV (circles).

determined over the interdot coupling range studied here. This value is consistent with previous values reported for GaAs [95] and InAs [96] double quantum dot systems.

At finite magnetic field the triplet state may also decay to the singlet via spin-orbit interaction. Theoretical and experimental investigations have been made on the individual roles of the spin-orbit interaction and the hyperfine interaction in a Pauli spin blockaded double quantum dot, showing that the interdot coupling plays a critical role in determining the relaxation process. [97, 98, 99] The experimental data presented in Figure 5.12(b) correspond well with hyperfine-dominated mixing, where a zero-field peak is expected for $\Delta = 0$. In the strong interdot coupling and finite magnetic field regime, spin-orbit mixing is expected to dominate. Here, a dip in leakage current around zero magnetic field and zero detuning is expected. The weak dip in leakage current for $\Delta = 0$ for the stronger coupling case in Figure 5.12(c) could be an indication of a transition to a regime where the spin-orbit interaction is important. Thus, the transition from a leakage current peak into a dip, also seen in figure 5.13(b) which shows two traces for $V_{lg3} = -265$ mV and $V_{lg3} = -255$ mV for detuning $\Delta = 0$, was interpreted as the transition where mixing of the singlet and triplet states from hyperfine interaction and spin-orbit interaction become comparable in size. However, further measurements are needed to study the regime in which the spin-orbit interaction dominates the mixing.

Populärvetenskaplig sammanfattning

I denna avhandling studeras ledningsförmågan hos nanometer-stora kvantprickar tillverkade i halvledarmaterial. Halvledare är material vars ledningsförmåga ligger någonstans mellan ledare (metaller) och isolatorer. I halvledare kan ledningsförmågan ändras med elektriska fält, vilket har möjliggjort utvecklandet av halvledartransistorn. Utvecklandet av halvledartransistorn har revolutionerat våra vardagliga liv eftersom den utgör den grundläggande byggstenen i elektroniska apparater som datorer, mobiltelefoner och digitala kameror. Det som har bidragit till den snabba utvecklingen av elektroniska komponenter är en ständigt pågående miniatyrisering av transistorns storlek. Denna miniatyrisering kan dock inte fortsätta eftersom det finns en gräns för hur små transistorer kan vara och samtidigt fungera som de gör idag. Gränsen nås då storleken på transistorn närmar sig våglängden på elektronerna i materialet. Elektronerna uppvisar då icke-klassiska, så kallade kvantmekaniska egenskaper som försämrar transistorns prestanda. Forskare försöker nu tillverka elektroniska nano-komponenter baserade på nya fysikaliska principer som utnyttjar de kvantmekaniska egenskaperna istället för att begränsas av dem. Kvantprickar är möjliga kandidater bland dessa nya nano-komponenter eftersom de uppvisar tydliga kvantmekaniska egenskaper och tillåter kontrollerad och flexibel manipulation med elektriska och magnetiska fält.

Flexibiliteten hos kvantprickar har lett till förslag att använda kvantprickar som komponenter i så kallade kvantdatorer. Tanken är att använda en elektrons spinn i en kvantprick som en grundläggande enhet, en *kvant-bit*, för att lagra information. Spinn är en kvantmekanisk egenskap som alla elementarpartikar besitter och kan sägas beskriva en partikels rörelsemängdsmoment. Kvantdatorer kan i teorin användas för att lösa vissa typer av problem väldigt mycket snabbare än dagens datorer.

Kvantprickarna som har studerats i denna avhandling har en storlek i nanometerskalan. En nanometer är en miljarddels meter, det vill säga $1/10^9$ meter. Kvantprickar kan liknas vid nanometerstora öar som elektroner är be-

gränsade att röra sig inom. På denna skala är de kvantmekaniska effekterna synliga och elektroner uppvisar både partikel- och vågegenskaper. Kvantprickar kan tillverkas på många olika sätt. I denna avhandling studeras kvantprickar som tillverkats i så kallade heterostrukturer eller nanotrådar bestående av halvledarmaterial. I dessa strukturer begränsas elektronernas rörelse i en respektive två riktningar. Med hjälp av elektriska fält kan de begränsas i alla riktningar. I våra mätningar har vi visat att vi kan skapa både enskilda kvantprickar samt två kvantprickar i följd. Storleken på de kvantprickar vi har skapat är cirka 100 nanometer i diameter.

Kvantprickar uppvisar många fysikaliska egenskaper som liknar egenskaperna hos atomer och brukar därför kallas *artificiella atomer*. Bland annat uppvisar kvantprickar ett diskret energispektrum där elektronerna som ockuperar kvantpricken bara kan anta vissa specifika energivärden. Dessa energivärden kan bestämmas genom att mäta ledningsförmågan genom kvantpricken. Strömmen genom kvantpricken är hög för de tillåtna energierna och låg för de förbjudna energierna. Genom att manipulera energinivåerna utifrån med elektriska och magnetiska fält kan diverse fysikaliska egenskaper, samt växelverkan mellan de elektroner som ockuperar kvantpricken, bestämmas genom att mäta ledningsförmågan på kvantpricken. Vi har lyckats bestämma dessa tillåtna energivärden i våra kvantprickar samt flera karakteristiska energier associerade med diverse fysikaliska egenskaper.

Även växelverkan mellan elektronerna på kvantpricken och omgivningen kan mätas. Vi har undersökt den elektrostatiska växelverkan mellan elektronerna på kvantpricken och en intilliggande ledare. På detta sätt har vi bestämt det exakta antalet elektroner som ockuperar kvantpricken. Vi har även lyckats mäta växelverkan mellan elektronerna på kvantpricken och de atomkärnor som utgör och omger kvantpricken, den så kallade *hyperfinväxelverkan*. Växelverkan med omgivningen har stor betydelse för kvantdatorn eftersom denna växelverkan frivilligt eller ofrivilligt kan påverka de tillstånd som kvantprickarna befinner sig i.

Bibliography

[1] John Bardeen, Walter Brattain and William Shockley received the 1956 Nobel Prize in Physics, www.nobel.se/physics/laureates/1956/

[2] Intel Corporation, *The evolution of a revolution*, http://download.intel.com/pressroom/kits/IntelProcessorHistory.pdf

[3] Intel Corporation, *Intel Core i7 Processor Extreme Edition Technical Documents*, http://download.intel.com/design/processor/datashts/323252.pdf

[4] I. Zutic, J. Fabian, and S. Das Sarma, *Spintronics: Fundamentals and applications*, Rev. Mod. Phys. **76**, 323 (2004).

[5] R. Hanson, L. P. Kouwenhoven, J. R. Petta, J. R. Tarucha, and L. M. K. Vandersypen, *Spins in few-electron quantum dots*, Rev. Mod. Phys. **79**, 1217 (2007).

[6] D. Loss, and D. P. DiVincenzo, *Quantum computation with quantum dots*, Phys. Rev. A **57**, 120 (1998).

[7] Y. Nakamura , Y. A. Pashkin, and J. S. Tsai, *Coherent control of macroscopic quantum states in a single-Cooper-pair box*, Nature **398**, 786 (1999).

[8] Y. Makhlin, G. Schön, and A. Shnirman, *Quantum-state engineering with Josephson-junction devices*, Rev. Mod. Phys. **73**, 357 (2001).

[9] R. F. Service, *Search for Majorana Fermions Nearing Success at Last?*, Science **332** 193 (2011).

[10] I. Vurgaftman, J. R. Meyer, L. R. Ram-Mohan, *Band parameters for III-V compound semiconductors and their alloys*, J. Appl. Phys. **89**, 5815 (2001).

[11] C. Weisbuch, and B. Vinter, 1991, *Quantum Semiconductor structures* (Academic press inc., San Diego).

[12] T. Ando, A. B. Fowler, and F. Stern, *Electronic properties of two-dimensional systems*, Rev. Mod. Phys. **54**, 437 (1982).

[13] M. Yazawa, M. Koguchi, and K. Hiruma, *Heteroepitaxial ultrafine wire-like growth of InAs on GaAs substrates*, Appl. Phys. Lett. **58**, 1080 (1991).

[14] K. Haraguchi, T. Katsuyama, K. Hiruma, and K. Ogawa, *GaAs p-n junction formed in quantum wire crystals*, Appl. Phys. Lett. **60**, 745 (1992).

[15] L. Samuelson, *Self-forming nanoscale devices*, Materials Today **6**, 22 (2003).

[16] K. v. Klitzing, G. Dorda, and M. Pepper, *New Method for High-Accuracy Determination of the Fine-Structure Constant Based on Quantized Hall Resistance*, Phys. Rev. Lett. **45**, 494 (1980).

[17] http://nobelprize.org/physics/laureates/1985/

[18] J. Feng, G. Thareja, M. Kobayashi, S. Chen, A. Poon, Y. Bai, P.B. Griffin, S. S. Wong, Y. Nishi, and J. D. Plummer, *High-Performance Gate-All-Around GeOI p-MOSFETs Fabricated by Rapid Melt Growth Using Plasma Nitridation and ALD Al_2O_3 Gate Dielectric and Self-Aligned NiGe Contacts*, IEEE Electron Device Letters **29**, 805 (2008).

[19] T. Bryllert, L. -E. Wernersson, T. Löwgren, and L. Samuelson, *Vertical wrap-gated nanowire transistors*, Nanotechnology **17**, S227 (2006).

[20] K.K. Likharev, *Single-electron devices and their applications*, Proceedings of the IEEE, **87** (1999) 606.

[21] P. Shor, *Algorithms for quantum computation: Discrete logarithms and factoring*, IEEE Symposium on Foundations of Computer Science, 124 (1994).

[22] J. R. Petta, A. C. Johnson, J. M. Taylor, E. A. Laird, A. Yacoby, M. D. Lukin, C. M. Marcus, M. P. Hanson, and A. C. Gossard, *Coherent Manipulation of Coupled Electron Spins in Semiconductor Quantum Dots*, Science **309**, 2180 (2005).

[23] F. H. L. Koppens, C. Buizert, K. J. Tielrooij, I. T. Vink, K. C. Nowack, T. Meunier, L. P. Kouwenhoven, and L. M. K. Vandersypen, *Driven coherent oscillations of a single electron spin in a quantum dot*, Nature **442**, 766 (2006).

[24] S. Nadj-Perge, S. M. Frolov, E. P. A. M. Bakkers, and L. P. Kouwenhven, *Spin-orbit qubit in a semicondutor nanowire*, Nature **468**, 1084 (2010).

[25] C. Flindt, A. S. Sørensen, and K. Fensberg, *Spin-Orbit Mediated Control of Spin Qubits*, Phys Rev. Lett. **97**, 240501 (2006).

[26] V. N. Golovach, M. Borhani, and D. Loss, *Electric-dipole-induced spin resonance in quantum dots*, Phys. Rev. B **74**, 165319 (2006).

[27] S. Debald, and C. Emary, *Spin-Orbit-Driven Coherent Oscillations in a few-Electron Quantum dot*, Phys. Rev. Lett. **94**, 226803 (2005).

[28] B. E. Kane, *A silicon-based nuclear spin quantum computer*, Nature **393**, 133 (1998).

[29] J. M. Taylor, C. M. Marcus, and M. D. Lukin, *Long-Lived Memory for Mesoscopic Quantum Bits*, Phys. Rev. Lett. **90**, 206803 (2003).

[30] L. Kouwenhoven, L. I. Glazman, *Revival of the Kondo effect*, Physics Worlds, January, 33 (2001).

[31] S. Sasaki, S. De Franceschi, J. M. Elzerman, W. G. van der Wiel, M. Eto, S. Tarucha, and L. P. Kouwenhoven, *Kondo effect in an integer-spin quantum dot*, Nature **405**, 764 (2000).

[32] J. Nygård, D. H. Cobden, and P. E. Lindelof, *Kondo physics in carbon nanotubes*, Nature **408**, 342 (2000).

[33] W. G. van der Wiel, S. De Franceschi, J. M. Elzerman, S. Tarucha, and L. P. Kouwenhoven, *Two-Stage Kondo Effect in a Quantum Dot at a High Magnetic Field*, Phys. Rev. Lett. **88**, 126803 (2002).

[34] Y. Igarashi, M. Jung, M. Yamamoto, A. Oiwa, T. Machida, K. Hirakawa, and S. Tarucha, *Spin-half Kondo effect in a single self-assembled InAs quantum dot with and without an applied magnetic field*, Phys. Rev. B **76**, 081303(R) (2007).

[35] P. Ramvall, N. Carlsson, P. Omling, L. Samuelson, W. Seifert, M. Stolze, and Q. Wang, *$Ga_{0.25}In_{0.75}As/InP$ quantum wells with extremely high and anisotropic two-dimensional electron gas mobilities*, Appl. Phys. Lett. **68**, 1111 (1996).

[36] T. Koga, J. Nitta, T. Akazaki, and H. Takayanagi, *Rashba Spin-Orbit Coupling Probed by the Weak Antilocalization Analysis in InAlAs/InGaAs/InAlAs Quantum Wells as a Function of Quantum Well Asymmetry*, Phys. Rev. Lett. **89**, 046801 (2002).

[37] R. S. Wagner and W. C. Ellis, *Vapor-liquid-solid mechanism of single crystal growth*, Appl. Phys. Lett. **4**, 89 (1964).

[38] W.H. Teh, C.-T. Liang, M. Graham and C.G. Smith, J. Microelectromech. Syst. **12**, 641 (2003).

[39] D. B. Suyatin, C. Thelander, M. T. Björk, I. Maximov, and L. Samuelson, *Sulfur passivation for ohmic contact formation to InAs nanowires*, Nanotechnology **18**, 105307 (2007).

[40] L. P. Kouwenhoven, D. G. Austing, and S. Tarucha, *Few-electron quantum dots*, Rep. Prog. Phys. **64**, 701 (2001).

[41] T. Ihn, *Electronic Quantum Transport in Mesoscopic Semiconductor Structures* (Springer-Verlag) (2004).

[42] W. G. van der Wiel, S. De Franceschi, J. M. Elzerman, T. Fujisawa, S. Tarucha, and L. P. Kouwenhoven, *Electron transport through double quantum dots*, Reviews of Modern Physics **75**, 1 (2003).

[43] C. W. J. Beenakker, *Theory of Coulomb-blockade oscillations in the conductance of a quantum dot*, Phys. Rev. B **44**, 1646 (1991).

[44] G. Breit, and E. Wigner, *Capture of Slow Neutrons* Phys. Rev. **49**, 519 (1936).

[45] U. Meirav, M. A. Kastner, S. J. Wind, *Single-Electron Charging and Periodic Conductance Resonances in GaAs Nanostructures*, Phys. Rev. Lett. **65**, 771 (1990).

[46] C. Fasth, A. Fuhrer, M. T. Björk, and L. Samuelson, *Tunable Double Qauntum Dots in InAs Nanowires Defined by Local Gate Electrodes*, Nano. Lett. **5**, 1487 (2005).

[47] T. Fujisawa, T. Hayashi, Y. Hirayama, H. D. Cheong, Y. H. Jeong, *Electron counting of single-electron tunneling current*, Appl. Phys. Lett. **84**, 2343 (2004).

[48] S. Roddaro, A. Fuhrer, P. Brusheim, C. Fasth, H. Q. Xu, L. Samuelson, J. Xiang, and C. M. Lieber, *Spin States of Holes in Ge/Si Nanowire Quantum Dots*, Phys. Rev. Lett. **101**, 186802 (2008).

[49] T. Fujisawa, G. Shinkai, and T. Hayashi, *Zeeman splitting in single-electron transport through a few-electron quantum dot*, Phys. Rev. B **76**, 041202 (2007).

[50] H. Kosaka, A. A. Kiselev, F. A. Baron, Ki Wook Kim, and E. Yablonovitch, *Electron g factor engineering in III-V semiconductors for quantum communications*, Electron. Lett. **37**, 464 (2001).

[51] B. Kowalski, P. Omling, B. K. Meyer, D. M. Hofmann, C. Wetzel, V. Härle, F. Scholz, and P. Sobkowicz, *Conduction-band spin splitting of type-I $Ga_xIn_{1-x}As/InP$ quantum wells*, Phys. Rev. B. **49**, 14786 (1994).

[52] S. Tarucha, D. G. Austing, T. Honda, R. J. van der Hage, and L. P. Kouwenhoven, *Shell filling and spin effects in a few electron quantum dot*, Phys. Rev. Lett. **77**, 3613 (1996).

[53] S. Tarucha, D. G. Austing, Y. Tokura, W. G. van der Wiel, and L. P. Kouwenhoven, *Direct Coulomb and Exchange Interaction in Artificial Atoms*, Phys. Rev. Lett. **84**, 2485 (2000).

[54] A. Fuhrer, T. Ihn, K. Ensslin, W. Wegscheider, and M. Bichler, *Singlet-Triplet Transition Tuned by Asymmetric GateVoltages in a Quantum Ring*, Phys. Rev. Lett. **93**, 176803 (2004).

[55] K. A. Matveev, L. I. Glazman, and A. I. Larkin, *g-Factors of Discrete Levels in Nanoparticles*, Phys. Rev. Lett. **85**, 2789 (2000).

[56] P. W. Brouwer, X. Waintal, and B. I. Halperin, *Fluctuating spin g-tensor in small metal grains*, Phys. Rev. Lett. **85**, 369 (2000).

[57] D. Csontos, and U. Zulicke, *Large variations in the hole spin splitting of quantum-wire subband edges*, Phys. Rev. B **76**, 073313 (2007).

[58] D. Csontos, and U. Zulicke, *Tailoring hole spin splitting and polarization in nanowires*, Appl. Phys. Lett. **92**, 023108 (2008).

[59] D. Csontos, U. Zulicke, P. Brusheim, and H. Q. Xu, *Lande-like formula for the g factors of hole-nanowire subband edges*, Phys. Rev. B **78**, 033307 (2008).

[60] C. Fasth, A. Fuhrer, L. Samuelson, V. N. Golovach, and D. Loss, *Direct measurement of the spin-orbit interaction in a two-electron InAs nanowire quantum dot*, Phys. Rev. Lett. **98**, 266801 (2007).

[61] V. N. Golovach, A. Khaetskii, and D. Loss, *Spin relaxation at the singlet-triplet crossing in a quantum dot*, Phys. Rev. B **77**, 045328 (2008).

[62] S. De Franceschi, S. Sasaki, J. M. Elzerman, W. G. Van Der Wiel, S. Tarucha, and L. P. Kouwenhoven, *Electron cotunneling in a semiconductor quantum dot*, Phys. Rev. Lett. **86**, 878 (2001).

[63] J. Kondo, *Resistance Minimum in Dilute Magnetic Alloys*, Progr. Theor. Phys. **32**, 37 (1964).

[64] D. Goldhaber-Gordon, H. Shtrikman, D. Mahalu, D. Abusch-Magder, U. Meirav, and M. A. Kastner, *Kondo effect in a single-electron transistor*, Nature **391**, 156 (1998).

[65] S. M. Cronenwett, T. H. Oosterkamp, and L. P. Kouwenhoven, *A tunable Kondo effect in quantum dots*, Science **281**, 540 (1998).

[66] W. G. van der Wiel, S. De Franceschi, T. Fujisawa, J. M. Elzerman, S. Tarucha, and L. P. Kouwenhoven, *The Kondo Effect in the Unitary Limit*, Science **289**, 2105 (2000).

[67] N. S. Wingreen and Y. Meir, *Anderson mode out of equilibrium: Noncrossing-approximation approach to transport through a quantum dot*, Phys. Rev. B **49**, 11040 (1994).

[68] Y. Meir, N. S. Wingreen, P. A. Lee, *Low-temperature Transport Through a Quantum Dot: The Anderson Model Out of Equilibrium*, Phys. Rev. Lett. **70**, 2601 (1993).

[69] P. Jarillo-Herrero, J. Kong, H. S. J. van der Zant, C. Dekker, L. P. Kouwenhoven, and S. De Francenschi, *Orbital Kondo effect in carbon nanotubes*, Nature **434**, 484 (2005).

[70] R. M. Potok, I. G. Rau, H. Shtrikman, Y. Oreg, and D. Goldhaber-Gordon, *Observation of the two-channel Kondo effect*, Nature **446**, 167 (2007).

[71] A. Fuhrer, T. Ihn, K. Ensslin, W. Wegscheider, and M. Bichler, *Kondo Effect in a Many-Electron Quantum Ring*, Phys. Rev. Lett. **93**, 176803 (2004).

[72] H. Jeong, A. M. Chang, and M. R. Melloch, *The Kondo Effect in an Artificial Quantum Dot Molecule*, Science **293**, 2221 (2001).

[73] N. J. Craig, J. M. Taylor, E. A. Lester, C. M. Marcus, M. P. Hanson, and A. C. Gossard, *Tunable Nonlocal Spin Control in a Coupled-Quantum Dot System*, Science **304**, 565 (2004).

[74] J. Kyriakidis, M. Pioro-Ladriere, M. Ciorga, A. S. Sachrajda, and P. Hawrylak, *Voltage-tunable singlet-triplet transition in lateral quantum dots*, Phys. Rev. B **66**, 035320 (2002).

[75] A. Kogan, G. Granger, M. A. Kastner, D. Goldhaber-Gordon, and Hadas Shtrikman, *Singlet-triplet transition in a single-electron transistor at zero magnetic field*, Phys. Rev. B **67**, 113309 (2003).

[76] G. Granger, M. A. Kastner, I. Radu, M. P. Hanson, and A. C. Gossard, *Two-stage Kondo effect in a four-electron artificial atom*, Phys. Rev. B **72**, 165309 (2005).

[77] T. Ihn, A. Fuhrer, K. Ensslin, W. Wegscheider, and M. Bichler, *Spin effects in a quantum ring* Physica E **26**, 225 (2005).

[78] C. Chung, and W. Hofstetter, *Kondo effect in coupled quantum dots with RKKY interaction: Effects of finite temperature and magnetic field*, Phys. Rev. B **76**, 045329 (2007).

[79] H. B. Heersche, Z. de Groot, J. A. Folk, L. P. Kouwenhoven, H. S. J. van der Zant, A. A. Houck, J. Labaziewicz, and I. L. Chuang, *Kondo Effect in the Presence of Magnetic Impurities*, Phys. Rev. Lett. **96**, 017205 (2006).

[80] Y. Bomze, I. Borzenets, H. Mebrahtu, A. Makarovski, H. U. Baranger, and G. Finkelstein, *Two-stage Kondo effect and Kondo-box level spectroscopy in a carbon nanotube*, Phys. Rev. B **82**, 161411 (2010).

[81] A. Eichler, M. Weiss, and C. Schönenberger, *Gate-tunable split Kondo effect in a carbon nanotube quantum dot*, Nanotechnology **22**, 265204 (2011).

[82] M. Pustilnik, and L. I. Glazman, *Kondo Effect in Real Quantum Dots*, Phys. Rev. Lett. **87**, 216601 (2001).

[83] W. Hofstetter, and H. Schoeller, *Quantum Phase Transition in a Multilevel Dot*, Phys. Rev. Lett. **88**, 016803 (2002).

[84] W. Hofstetter, and G. Zarand, *Singlet-triplet transition in lateral quantum dots: A numerical renormalization group study*, Phys. Rev. B **69**, 235301 (2004).

[85] P. Simon, R. Lopez, and Yuval Oreg, *Ruderman-Kittel-Kasuya-Yosida and Magnetic-Field Interactions in Coupled Kondo Quantum Dots*, Phys. Rev. Lett. **94**, 086602 (2005).

[86] V. Meden, and F. Marquardt, *Correlation-Induced Resonances in Transport through Coupled Quantum Dots*, Phys. Rev. Lett. **96**, 146801 (2006).

[87] V. Kashcheyevs, A. Schiller, A. Aharony, and O. Entin- Wohlman, *Unified description of phase lapses, population inversion, and correlation-induced resonances in double quantum dots*, Phys. Rev. B **75**, 115313 (2007).

[88] M. Field, C. G. Smith, M. Pepper, D. A. Ritchie, J. E. F. Frost, G. A. C. Jones, and D. G. Hasko, *Measurements of Coulomb blockade with a noninvasive voltage probe*, Phys. Rev. Lett. **70**, 1311 (1993).

[89] L. M. K. Vandersypen, J. M. Elzerman, R. N. Schouten, L. H. Willems van Beveren, R. Hanson, and L. P. Kouwenhoven, *Real-time detection of single-electron tunneling using a quantum point contact*, Appl. Phys. Lett. **85**, 4394 (2004).

[90] T. Fujisawa, T. Hayashi, R. Tomita, and Y. Hirayama, *Bidirectional Counting of Single Electrons*, Science **312**, 1634 (2006).

[91] S. Gustavsson, R. Leturcq, B. Simovic, R. Schleser, T. Ihn, P. Studerus, K. Ensslin, D. C. Driscoll, and A. C. Gossard, *Counting Statistics of Single Electron Transport in a Quantum Dot*, Phys. Rev. Lett. **96**, 076605 (2006).

[92] B. J. van Wees, H. van Houten, C. W. J. Beenakker, J. G. Williamson, L. P. Kouwenhoven, D. van der Marel, and C. T. Foxon, *Quantized conductance of point contacts in a two-dimensional electron gas*, Phys. Rev. Lett. **60**, 848 (1988).

[93] K. Ono, D. G. Austing, Y. Tokura, and S. Tarucha, *Current Rectification by Pauli Exclusion in a Weakly Coupled Double Quantum Dot System*, Science **297**, 1313 (2002).

[94] O. N. Jouravlev, and Y. V. Nazarov, *Electron Transport in a Double Quantum Dot Governed by a Nuclear Magnetic Field*, Phys. Rev. Lett. **96**, 176804 (2006).

[95] F. H. L. Koppens, J. A. Folk, J. M. Elzerman, R. Hanson, L. H. Willems van Beveren, I. T. Vink, H. P. Tranitz, W. Wegscheider, L. P. Kouwenhoven, and L. M. K. Vandersypen, *Control and Detection of Singlet-Triplet Mixing in a Random Nuclear Field*, Science **309**, 1346 (2005).

[96] A. Pfund, I. Shorubalko, K. Ensslin, and R. Leturcq, *Spin-state mixing in InAs double quantum dots*, Phys. Rev. B **76**, 161308(R) (2007).

[97] A. Pfund, I. Shorubalko, K. Ensslin, and R. Leturcq, *Suppression of Spin Relaxation in an InAs Nanowire Double Quantum Dot*, Phys. Rev. Lett. **99**, 036801 (2007).

[98] J. Danon and Yu. V. Nazarov, *Pauli spin blockade in the presence of strong spin-orbit coupling*, Phys. Rev. B **80**, 041301(R) (2009).

[99] S. Nadj-Perge, S. M. Frolov, J. W. W. van Tilburg, J. Danon, Yu. V. Nazarov, R. Algra, E. P. A. M. Bakkers, and L. P. Kouwenhoven, *Disentangling the effects of spin-orbit and hyperfine interactions on spin blockade*, Phys. Rev. B **81**, 201305(R) (2010).